UNIVERSITY OF TRIESTE

XXXI CYCLE OF THE PhD COURSE IN NANOTECHNOLOGY

COMPUTATIONAL INVESTIGATION OF NANOPARTICLES AT THE BIOINTERFACE

ING-IND/24

Coordinator

Lucia Pasquato

PhD Student

Silvia Boccardo

Supervisor

Paola Posocco

Co-supervisor

Loredana Casalis

"Ogni cosa che puoi immaginare,

la natura l'ha già creata"

ABSTRACT

Molecular self-assembly is a topic attracting intense scientific interest. Various strategies have been developed for construction of molecular aggregates with rationally designed properties, geometries, and dimensions which are able to provide solutions to both theoretical and practical problems in areas such as drug delivery, medical diagnostics, and biosensors, to name but a few. In this respect, gold nanoparticles (AuNPs) with core diameters in the rage 1−10 nm have emerged as a powerful class of materials for a variety of biomedical applications. The utility of AuNPs is enhanced by our ability in tuning their surface properties by grafting multiple ligand species able to self-assemble in mixed-monolayers. Thus, identification of molecular designing rules is essential to achieve a precise control of specifically patterned monolayer protected nanoparticles for an intended biological outcome. In this thesis are described the evidences of our investigation of the self-organization of different mixtures of immiscible ligands on a spherical gold surface. The evaluation of the role of some critical parameter such as core dimension, different chemistry and relative ligand length and ratio as well as solvent was the starting point to develop a standard procedure to tune the self-assembled monolayer (SAM) morphology. Studies of the morphology of these mixed monolayers were carried out using an *in-silico* approach based on multiscale molecular simulations. Then, combining theory and experiments, we investigated the role of ligand arrangement and composition on the interaction with model lipid bilayer (either simple and complex) and with cells of these monolayer protected NPs. *In-silico* models were then employed to study the binding of patterned AuNps with human serum albumin (HSA), uncovering the impact of the monolayer morphologies on protein-NP interfaces. Laslty, a third kind of biointerface was taken into account and the supramolecular binding of small molecules, toward mixed/homoligand shells was disclosed.

SOMMARIO

L'autoassemblaggio a livello molecolare è un argomento che negli ultimi anni sta attraendo un alto interesse scientifico. Sono state sviluppate diverse strategie per costruire aggregati molecolari con proprietà, geometrie e dimensioni predefinite, che sono in grado di fornire soluzioni sia a problemi teorici che pratici in aree quali il trasporto di farmaci, diagnostica medica e biosensori, solo per citarne alcuni. In questo panorama le nanoparticelle d'oro (AuNPs), con diametro compreso tra 1 e 10 nm, sono emerse come un potente strumento per varie applicazioni biomediche. L'utilità di queste AuNPs è ulteriormente potenziata dalla nostra capacità di metterne a punto le proprietà superficiali utilizzando diversi tipi ligandi che sono in grado di auto assemblarsi in monostrati misti. Per questo motivo identificare regole di design molecolare è essenziale per ottenere un preciso controllo della morfologia del monostrato che ricopre il nocciolo d'oro, nell'ottica di uno specifico interesse biologico. In questa tesi sono descritti i risultati dello studio sull'autoassemblaggio di ligandi immiscibili su una superfice d'oro sferica. Valutando il ruolo di alcuni parametri critici (es: dimensione del nocciolo, lunghezza dei ligandi, diversa chimica e solvente) è stato possibile sviluppare una procedura standard per regolare la morfologia del monostrato auto assemblante (SAM). Studi sulla morfologia di strati auto assemblanti sono stati eseguiti per mezzo di un approccio *in-silico* basato su simulazioni multi scala. Combinando teoria con esperimenti, è stato possibile investigare che ruolo gioca l'arrangiamento e la composizione dei ligandi sull'interazione con membrane lipidiche (mono e multi componente) e con cellule di queste nanoparticelle. Modelli *in-silico* sono stati utilizzati per valutare l'interazione di AuNPs protette da SAM con l'albumina, proteina del siero umano, per comprendere come la presenza di diverse morfologie possa influire sull'interazioni di queste nanoparticelle all'interfaccia con le proteine. Infine, è stata analizzata la capacità di AuNPs protette da strati auto assemblanti di interagire con piccole molecole e come diverse morfologie possano influire sulla capacità di carico e di interazione di queste nanoparticelle.

Summary

List of figures

List of tables

List of acronyms

ESR: Electro Spin Resonance

SPR: Surface Plasmon Resonance

NPs: Nanoparticles

SAM: Self-Assembled Monolayer

AFM: Atomic Force Microscopy

AuNPs: Gold Nanoparticles

HSA: Human Serum Albumin

UV-VIS: Ultraviolet Visible

TEM: Transmission electron microscope

TGA: Thermogravimetric analysis

NMR: Nuclear magnetic resonance

DPD: Dissipative Particle Dynamics

MD: Molecular Dynamics

TFP: Triphenylphosphine

PEG: PolyEtylene Glycol

MUS: Mercaptoundecanesulphonate

MDDS: Mercaptododecanesulphonate

MHDS: Mercaptohesadecanesulphonate

CG: Coarse Grain

AA: All-atom

NBI: Nano-bio interface

MPNPs: Monolayer Protected Nanoparticles

DOPC: dioleoyl-sn-glycero-3-phosphocholine

Chol: Cholesterol

SM: sphingomyelin

ZW: zwitterionic

EPy: 4-EthylPyridine

Py: Pyridine

BSA: Bovine Serum Albumin

HSA: Human Serum Albumin

CV: Crystal Violet

DOXO: Doxorubicine

DOXI: Dunorubicinone

Chapter 1. *Nano-bio interface*

The promise of nano-biomaterials for diagnostic and therapeutic biomedical applications has been widely reported throughout the recent years. (1-6) And yet, the translation of nanomaterial-based therapeutics to clinical applications remains an elusive target. Toxicity, immunogenicity, and decreased efficacy have been some of the main challenges in using nanomaterials in biomedicine. To overcome some of these problems, many studies have been undertaken to understand the interactions between nanomaterials and the biological environment. Identifying ways in which the nanomaterial interface can be controlled enhancing the possibility to tune the interactions with biomolecules for beneficial biomedical applications.

Under the correct lens, almost anything may be considered a material. Biological molecules add an extra level of complexity due to their unique structure e.g. proteins, enzymes, DNA, and lipids. Currently, many biomedical applications of nanomaterials rely on the functionality of attached biomolecules to target, deliver, image or mediate interactions with the biological environment. (7-19)

The attachment of a biomolecule on the nanomaterial surface resulted in changing the structure of the biological molecule itself. This could lead to an alteration of the biological function giving birth to a completely new nanomaterial that could interact with the biological environment in an unpredictable way. (20-24)

At the same time, engineered nanoparticles are the most promising platform for nanoscale diagnostic/therapeutic strategies. (25-27)

The nano-bio interface comprised physicochemical interactions, kinetics and thermodynamic exchanges at the interfaces between NP and biological surfaces. (28)

The surfaces of nanoparticles will progressively and selectively adsorb biomolecules, unless they have been designed to do otherwise. This ‘corona’ of biomolecules lowers the surface energy of the nanoparticle and promotes its dispersion. (29-35)

There is no way to fully describe all the bio-physicochemical interactions that occurred at the NBI; yet, there is the necessity to develop a rational approach for understanding how the properties of engineered NPs relate to biological behavior and how the design of those

properties could be exploited in optimizing the efficacy of NPs for safe diagnostic/therapeutic use. The current methodology is mainly based on in vitro and in vivo studies. However, experiments are demanding in terms of time, costs, and resources. In this context, computational models are a powerful tool for analyzing biological information that are not accessible to other modeling and experimental techniques. (36)

1.1 Gold nanoparticles protected with self-assembled monolayers

Gold NPs (AuNPs) are one of the most promising engineered nanoparticle types, having high potential for biomedical applications. (37, 38) Bulk gold is chemically inert and it is possible to easily synthesize gold nanoparticles with controlled size, shape, and surface chemistry. Moreover, AuNPs possess excellent optical properties at the nanoscale, enabling a wide variety of analytical techniques for tracking and imaging gold in biological samples, including cells and tissues (39).

In the recent years a lot of different functionalized AuNPs where used in bio-nanotechnology applications (sensing, targeting, imaging). We report here only few examples to give an overall idea on how broad could be the field of applications of these nanomaterials. AuNPs could be conjugated with antibodies or oligonucleotides for the detection of target biomolecules,43 to be used for *in vitro* detection and diagnosis of cancer. (40) In another interesting study, they were used in the "bio-barcode assay" (41). AuNPs were conjugated with both barcode oligonucleotides and target-specific antibodies, and magnetic microparticles functionalized with monoclonal antibodies for the target moiety. These complexes produced a sandwich that released a large amount of barcode oligonucleotides, providing both identification and quantification of the target. (42) Mirkin *et al*. demonstrated the detection of prostate specific antigen (PSA) using Au-NP PSA probe design, PSA-specific antibodies covalently attached to the gold surface, applying the bio-barcode methodology with a limit of detection of 330 fg/mL. (43), while Zeng *et al*. reported an aptamer-nanoparticle strip biosensor (ANSB) system for the detection of Ramos (lymphoma) cells (44). Using non-covalent conjugates of AuNPs and fluorophore molecules Rotello and co-workers obtained high sensitivity sensing of biomolecular targets (45). This method was able to differentiate 12 different species/strains of bacteria with 95% accuracy. Moreover, this strategy was used to differentiate normal, cancerous and metastatic cells in a rapid and accurate assay.

AuNPs could also be used also to transport therapeutic agents into cells and several research groups have investigated how functionalized AuNPs interact with cell membranes to improve the efficiency of the delivery process (46). Mirkin *et al*. used RNA-AuNP conjugates to knockdown luciferase expression showing the conjugates have a half-life six times longer than that of free dsRNA and demonstrating a high gene knockdown capability (47). Rotello *et al*. also demonstrated that cationic AuNPs, featuring cationic amino acid-based side chains, can be used for DNA transfection. (48)

The optical and electronical properties of gold nanoparticles allowed to use them for cell imaging exploiting a variety of techniques. AuNPs could be used as a contrast agent for CT imaging based on the higher atomic number and electron density of gold as compared to the currently used iodine. Hainfeld *et al*. showed that AuNPs enhance the *in vivo* vascular contrast in CT imaging, (49), and Kopelman *et al*. further designed immuno-targeted AuNPs to selectively target tumor specific antigens. (50) Jon *et al*. used a prostate specific membrane antigen (PSMA) aptamer-conjugated AuNPs (PSMA-AuNPs) to establish a molecular CT image for the specific imaging of prostate cancer cells. (51)

1.1.1 Homoligand self-assembled monolayer-protected gold nanoparticles

Surface modification with tailored chemistry is a commonly used route to control AuNPs physicochemical and surface-related properties. The most widely used approach, both in experimental and theoretical studies, consist of a gold core protected with a self-assembled monolayer (SAM) of thiolate ligands. Generally speaking, SAMs of organic molecules are molecular assemblies formed spontaneously on a substrate (either flat or curved) by adsorption and organized into large ordered domains. (52)

The available library of thiolate ligands for NP functionalization is extensive and includes functional moieties such as alcohols, alkyl halides, amines, amino acids, amphiphilic polymers, azides, carbohydrates, carboxyl acids, nucleic acids, peptides, phenols and proteins. Other electroactive ligands such as sulfonates and nitriles offer alternative routes to enhance the activity of SAM-protected AuNPs in biological environments. Apart from being complex, self-organized, multivalent systems, SAM-protected AuNPs also exhibit structural features comparable to many biological systems including proteins, nucleic acids and many cellular substructures. The success in synthesizing sub-10 nm SAM-protected

AuNPs has provided a unique opportunity to model interfacial phenomena at natural surfaces, which are dominant in biological activities.

A number of experimental and theoretical studies have been carried out to elucidate the molecular features and organization of SAMs on flat and curved gold surfaces. (53, 54) An established property of SAMs constituted by *alkyl* thiolates on flat substrates is that the adsorbed molecules arrange themselves with a tilt angle relative to the surface normal to maximize packing (i.e., van der Waals interactions between chains). Assuming that the ligand packing on flat surfaces and on nanoparticle is the same that would mean that molecules would generate a large number of defects at the facet edges. (55)

In their work, Glotzer and coworkers revealed how stripe-like domains, present on the curved surface of AuNPs, formed by atomistic and mesoscale simulations. (56-59) The formation of striped domains may derive from the ligands length mismatch, or from their different bulkiness. Another crucial parameter that determined the formation of ordered domains in a SAM is the NP core size. On small NPs, a binary mixture tended to separate into two distinct phases (i.e., Janus arrangement), as all chains gained free volume due to the high surface curvature and there was no entropic gain on formation of new interfaces. Decreasing the surface curvature, the available free volume decreased and the entropic gain associated with the formation of new interfaces increased. When the NP radius is further increased, disordered stripes and patchy domains are expected to dominate. (60)

Due to the curvature of the gold core the SAM used to coat it presented enough space between different ligand chains to trap small molecules through host-guest interactions which facilitate selective binding events between ligands and target analytes based on molecular recognition, as shown in *Figure 1*.

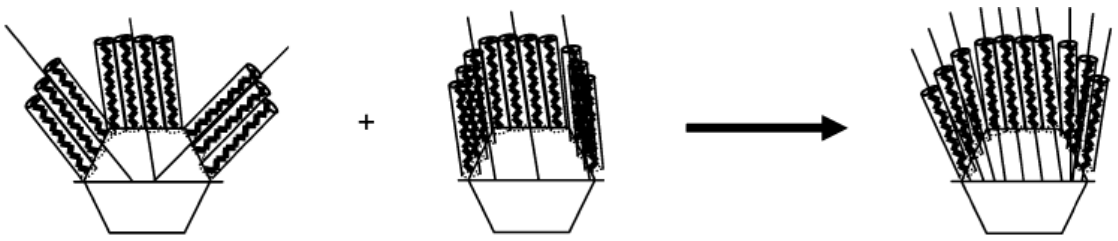

Figure 1: Simplified representation of ligand packing for homoligand nanoparticles. Ligands may be organized on a faceted core essentially in two configurations: they can assume their optimal tilt angle with regard to each facet (left), or they can assume a global tilt angle (middle). The first configuration leads to high-energy defects at the crystal edges, while the second does not take advantage of the particle curvature. The real *configuration*

is likely a compromise between the two, with the ligands roughly conforming to a global tilt angle, but relaxing, and splaying outward (right). (61)

The monolayers are so expected to exhibit a selective host-guest chemistry taking advantage of specific design of the monolayer itself. Increasing the complexity of the system using a mixture of incompatible ligands to form the monolayer offers a further degree of freedom.

1.1.2 Mixed SAM protected nanoparticles

When mixed SAMs of dislike molecules are employed to coat AuNPs, nanoscale domains may spontaneously form in the particle shell, thus leading to the generation of anisotropy with regards to surface functionalization via ligand arrangement. The spontaneous formation of 3D patterns (e.g. patched, striped or Janus domains see Figure 2), within the surface shell of immiscible ligands employed to coat gold nanoparticles, depended on the sum of two different effects: (56)

- Minimization of enthalpy
- Maximization of conformational entropy.

The first one reduces the contact between immiscible ligands, while the gain of the second depended on the formation of interfaces between immiscible thiolates with different properties in terms of length and steric hindrance. Glotzer and coworkers demonstrated that the formation of stripes, made of two immiscible ligands of enough difference in length was universal and did not depend on the chemistry of the surfactants. Stripes form only when sufficient conformational entropy is gained during their formation. For surfactants with two different lengths, the gain of entropy for the longer surfactant is larger due to the availability of free volume around the surfactant tail group overcoming the loss of entropy due to stripe formation. Moreover, stripe thickness depended on various factors, such as the solvent, the length of the alkanethiol tail, charge on the headgroup. (60)

While few different morphologies are admissible dealing with a binary mixture of ligands, if we consider combinations of a higher number of thiols the number of possible morphologies increases. (61). Starting from these theoretical evidences it seemed possible to tune the morphological characteristics of the mixture of immiscible ligands, used to coat the NP surface, based on easy-to-control parameters (e.g. ligand length, NP gold core

dimensions) as well as on some less controllable parameters (e.g. ligand degree of immiscibility and stoichiometry). (62; 63; 56), (64-73). Presence of discrete domains at the nanometer level provide surface properties (such as interfacial energy, solubility, or wettability) to engineered AuNPs that cannot be explained simply based on the bulk composition alone and allows tailoring of nanosurfaces with a wide variety of specific features.

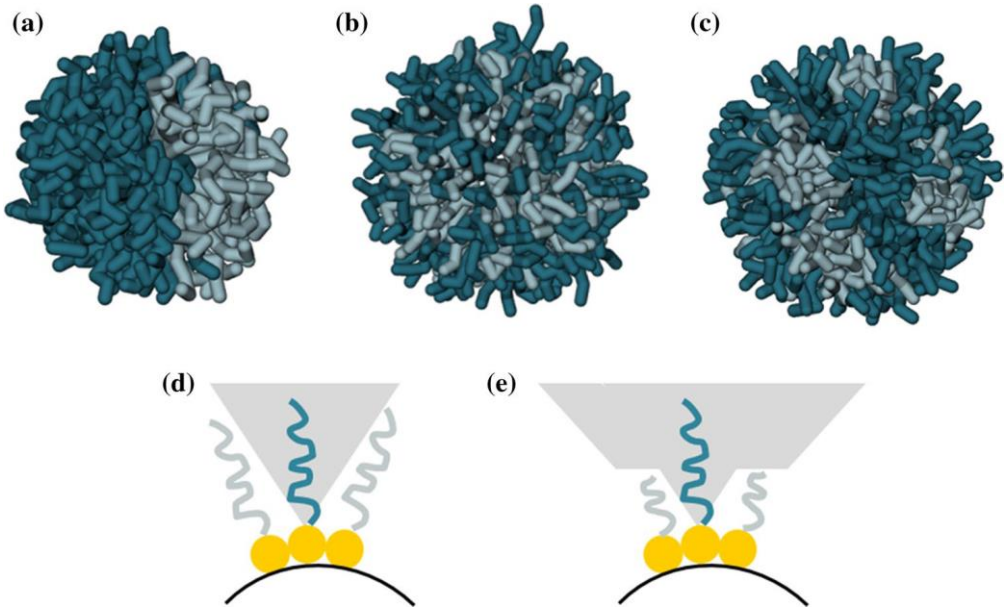

*Figure 2: Typical 3D organization of two immiscible ligands (dark- and light-blue sticks) on a curved surface: Janus (**a**), mixed random (**b**), and regularly striped (**c**). Schematic representation of the free volume (grey area) that the ligand tails are allowed to sample on an NP surface, when surrounded by other types of surfactant chains of the same (**d**) or different length (**e**) on curved surfaces. Ligand length mismatch endows longer tails with more available free volume, which results in an interface entropy gain and favors striped pattern formation over complete phase segregation.*

The preparation of patterned NPs may follow two general process: spontaneous self-assembly of subunits or step-by-step synthesis using an external template (71; 75-78). Regarding gold NPs, subunits used are typically thiols, given the strength of the gold–sulfur bond (~40 kcal/mol) (79). Spontaneous self-assembling is driven by the fact that mixtures of immiscible ligands can spontaneously form a patterned monolayer due to structural mismatches, ligand immiscibility and the resulting morphologies represents thermodynamic minima for each system. The step-by-step synthesis technique represent the traditional approach, in which monolayer patches were obtained directly on the NPs with external tools or by ad hoc synthetic procedures. For example, NPs were deposited onto solid supports and then, generating air–liquid or liquid–liquid interfaces two large portions of the NP surface

can be selectively functionalized. This procedure was particularly useful for preparation of Janus nanoparticles so the alternative, self-assembly approach is more suitable for obtaining other morphologies. (60)

Moreover, as in the biological environment other biological structures (e.g. proteins, cell membranes) presented patterns of hydrophilic/hydrophobic areas, these morphological characteristics of the SAM were expected to influence the interaction of SAM-protected NPs with proteins and membranes or other surface-related biological processes. (80-86).

1.2 Mixed SAM protected nanoparticles at the bio-interface

To determine the capacity of MPNPs to be internalized into cells and which kind of biological response they promote, it is necessary to understand their behavior once in contact with the biological environment. Two are the main nano-bio interfaces SAM protected nanoparticles came in contact with:

- Membranes
- Proteins
- Cells

1.2.1 Nanoparticle interactions with membranes

Membrane models (MMs) are currently used to study the influence of the chemical properties of SAM protected NPs on their interactions with lipid bilayers. Membrane attachment is mainly characterized by the use of supported lipid bilayers (SLBs), associated with methods such as surface plasmon resonance (SPR) (87; 88), quartz crystal microbalance measurements with dissipation monitoring (QCM-D), and atomic force microscopy (AFM). Several theoretical studies have recently been performed to evaluate the molecular aspects of NP–membrane interactions. Classical methods such as molecular dynamic (MD) were the most used. However, most biological phenomena occur on time and length scales which were not accessible to MD calculations, and less-detailed techniques, such as Coarse Grain (CG) (89-91) become necessary. Moreover, membrane composition varies with respect of different cell types and influencing the global properties of the membrane (92-94), determining different type of interactions with NPs.

Some computational studies investigate how different surface patterns can affect membrane interactions often correlated to experimental studies while others consider only Janus-type systems. (95-98)

Stellacci's group first showed that striped NPs entered cells via spontaneous diffusion, while NPs with the same ligand composition but random morphology were internalized through the endocytic pathway (99-101). Li et al. (102) tried to give an explanation to these different behaviors. They compared the free energy change associated to translocation through a lipid bilayer for four different types of hydrophilic/hydrophobic patterned NPs. They found that striped NPs lowered the energy barrier to cross the membrane, justifying the diffusion of these systems through lipid bilayers.

Thanks to Van Lehn and Alexander-Katz that provided an accurate description of the interaction mechanism for anionic MUS/OT patterned NPs and a model 1,2-dioleolyl-*sn*glycero-3-phosphocholine (DOPC)-composed membrane, the first critical step is the contact between a hydrophobic patch on the NP and a membrane lipid tail bending up and protruding into the aqueous medium. (103; 104) Once this initial contact has been established, the SAM deform to maximize the contact chances (Figure 3).

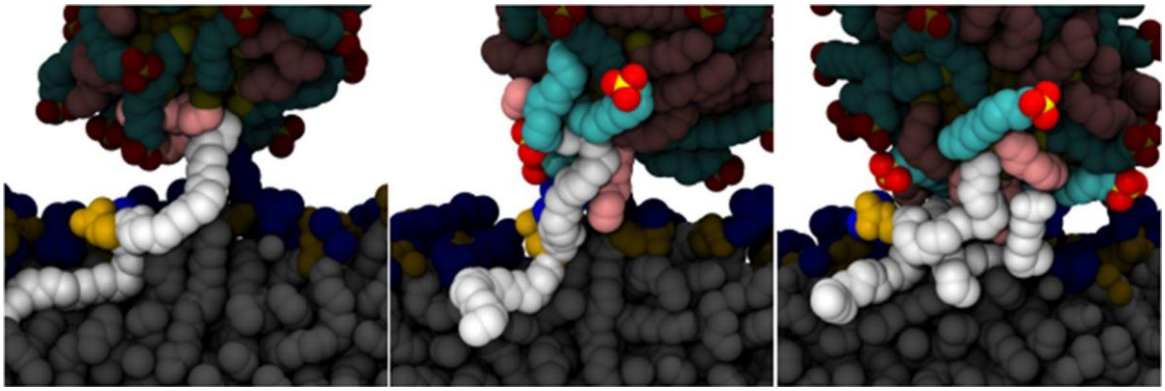

Figure 3: Stages of NP insertion into a membrane following protrusion contact. The first protruding membrane lipid (left panel), the NP ligands [MUS:OT (1:1) on a 2-nm NP] and other membrane lipids successively (center and right panels) recruited are highlighted in each image. Lipid tails are represented as white spheres, phosphate groups are in yellow, and choline groups in blue. MUS molecules contacting the bilayer in green (corresponding to CH2 groups), yellow (sulfur atoms), and red (oxygen atoms) spheres, while OT molecules are presented as pink chains. Lipids and ligands not presently involved in the insertion process appear dark. [Adapted with permission from (Van Lehn and Alexander-Katz 2015). Copyright (2015) Royal Society of Chemistry]

The membrane progressively increased its curvature relieved only when the NP core is deeply inserted into the bilayer (103). An important consideration emerged from these studies, that there is a little influence of the nanopatterned SAM morphology due to the fact that striped, mixed, random or patchy morphologies are virtually indistinguishable from each other for 1:1 and 2:1 MUS/OT compositions, the only exception being the Janus morphology. (197; 105) The monolayer composition seems to play the dominant role in determining the likelihood of insertion.

From these evidences, it is not surprising that most of the computational investigations used a simplified membrane representation with the bilayer composed of one or a few different lipid molecules (106, 107).

1.2.2 Nanoparticle interactions with proteins

Nowadays, nanoparticles had been widely applied for numerous biomedical applications, such as bioimaging, biosensing, drug delivery, diagnostics, and therapy. When NPs came in contact with biofluids such as blood, plasma and serum, the adsorption of proteins was just around the corner forming the so-called protein corona (108, 109). The protein corona could dramatically alter the interfacial properties of nanomaterials, giving them a new biological identity that is for sure different from the native synthetic one (110). Moreover, this biological identity was able to elicit some physiological responses (e.g. agglomeration, cellular uptake, circulation lifetime, signaling, kinetics, accumulation, and toxicity) mediating the interaction of the nanomaterial with the biological environment (111). The precise mechanism(s) of formation of the protein corona is still far from being understood, since it depended on numerous factors as well as on the nanomaterial (size, shape, charge, hydrophobicity, composition, surface functionalization), the proteins (size, shape, charge, isoelectric point, and conformational flexibility), and the physiological environment (polarity, ionic strength, pH, and temperature), side (112, 113).

Furthermore, the formation of a protein layer around NPs hampered their specific delivery and targeting capabilities. The use of targeted NPs in bio-nanotechnology could be improved by tuning their surface making them able to bind proteins selectively, modulating their capabilities of signaling, uptake, transport. Conversely, NP could alter the structure of the adsorbed proteins becoming potentially a hazard. (112-118)

Several number of studies were carried out to uncover the physiological responses to nanomaterial–protein complexes (119-122) but, due to the complexity of physiological systems (123) and the experimental difficulty of evaluating the characteristics of the corona a comprehensive description of these phenomena is missing. Moreover, most of the present studies involved homoligand coated NPs while only a few have evaluated the influence of a nanostructured surface (size range comparable to proteins). Studies on patterned NPs have shown that composition and morphology of the SAM affect the binding of proteins, such as bovine serum albumin (BSA) bind. Fluorescence quenching, dynamic light scattering (DLS), circular dichroism (CD), and isothermal titration calorimetry (ITC) performed on NPs with either striped or randomly morphology suggested different "side-on" or "end-on" bovin serum albumin conformations on the NP, depending on its shell organization. (124) In another combined experimental/computational study, interactions of cytochrome *c* (cyt *c*) with nanopatterned surfaces (mixtures of 6-mercapto- 1-hexanol (MH) and OT ligands) were evaluated using protein assays and computational MD simulations. The combined approach highlighted that the cyt *c* exhibited increased its adsorption increasing the MH proportion, suggesting that the interactions were largely hydrophilic. (125) The same key role of the surface structural and chemical heterogeneity of nanoscale patterned NPs was also confirmed by a further computational study involving lysozyme and specifically patterned planar surfaces of self-organized 6-mercapto-1-hexanol (MH) and octanethiol (OT) thiols (126). These evaluations suggested that nanoparticle surfaces needed to be tuned to combine with different/specific proteins, and proteins needed to be engineered to specifically interact with nanomaterials. (60)

1.2.3 Nanopatterned nanoparticles interaction with cells

The retention of NPs in human body can lead to toxic effects, even though NPs are often described as "safe". These toxic effects are particularly relevant if the retention persist for long periods at high concentrations. (127; 128) Fratoddi et al. (129) reviewed and summarized the commonly used assays to determine the effects of NP exposure on cell viability (membrane damage assays, viability tests). Unfortunately, results measured by these assays were not straightforward (130), and a standardization of the procedure/methodology is required to assess the overall toxicity of NPs. Experiments with a wide range of cells have been performed to test the toxicity of NPs. Cells should be in the logarithmic growth phase rather than in the stationary phase to be more sensitive to toxic

effects. (131) This being said, tuning the coating of NPs can affect both internalization (132-135; 105; 101) and decrease the toxicity. (136; 137)

Interestingly, NPs that present similar surface chemistry but different surface morphologies (e.g., striped versus random ligand arrangements) can have similar internalization ability, different internalization pathways, and correspondingly different cell toxicities. It has been reported that NPs with random morphologies are more toxic than striped ones. (128). Drug delivery is one of the main fields of bioapplication for patterned NPs (138). Striped MUS/OT NPs were able to transport single- and double-strand DNA into B16-F0 melanoma cells. Amphiphilic ligand-coated AuNPs exhibited remarkable lymph node tissue accumulation. When tested for vaccine delivery after conjugation with a peptide antigen (SIINFEKL), they drastically improved the peptide vaccine response compared with free antigen or linker-antigen administration. (139)

Amphiphilic stripe-like MUS/OT AuNPs were loaded into multilamellar lipid vesicles and delivered to tumor cells, where they increased the cell killing ability. (140).

Chapter 2. *Computational techniques*

This chapter describes the main computational techniques applied in the thesis to model homo/hetero self-assembled monolayer protected gold nanoparticles, to evaluate the molecular features and structural properties of the different monolayers that coat the gold surface and their interaction with the biological environment (membranes and proteins).

2.1 Molecular dynamics

Molecular dynamics is a computational technique that allow one to predict the time evolution of a system of interacting particles (atoms, molecules) and estimate relevant physical properties. It generates information as atomic positions, velocities, and forces from which the macroscopic properties (e.g., energy, pressure, …) can be derived by means of statistical mechanics. MD simulation usually consists of three main constituents: (i) a set of initial conditions (initial positions and velocities of all particles in the systems); (ii) the interaction potentials to represent the forces among all particles; (iii) the evolution of the system in time by solving a set of classical Newtonian equations of motion for all particles in the system:

$$-\frac{dE(R)}{dR} = m\frac{d^2R}{dt^2}$$

where *E(R)* described the potential energy of the system which depended from the initial conditions employed, *R* represented the coordinates and *m* the molecular mass of the atoms.

A force field (FF) represented the analytic expression that described the potential energy E(R) of the considered molecular model. It generally sums up singles energetic contributions such as:

- **Bonded energies**: due to interactions between connected atoms, depending on angles and bond types
- **Non-bonded energies**: due to not-bonded atoms, depending on Van der Waals and electrostatic interactions and hydrogen bonds

Different types of FF existed and were dedicated to different aspects of molecular simulations; sometimes happened that some parameters were not present in the selected FF, but they might be really necessary for the parametrization of a molecule that holds specific atoms. These missing parameters could also be calculated with *ab initio* methodologies or substitutes with experimental values, if available. (137)

Contributions of the bonded and non-bonded energies can be summed up as:

$$E(R) = E_{valenza} + E_{no-bond} + E_{cross}$$

in which $E_{valenza}$ represented chemical bonds, $E_{no-bond}$ the electrostatic interactions and E_{cross} bonds and angles distortions.

Going deeper in detail:

$$E_{valenza} = E_{bond} + E_{angle} + E_{tosion}$$

- $\boldsymbol{E_{bond}}$: energy term proportional to the distance between two atoms chemically bonded
- $\boldsymbol{E_{angle}}$: energy term related to the bending of angles formed by to bonds
- $\boldsymbol{E_{torsion}}$: energy term related to the torsional motion of dihedral angles formed by 3 consecutive bonds

$$E_{no-bond} = E_{Van\ de\ Waarls} + E_{Coulomb} + E_{hydrogen\ bonds}$$

- $\boldsymbol{E_{Van\ de\ Waarls}}$: energy term related to the Van Der Waals interactions between atoms
- $\boldsymbol{E_{Coulomb}}$: energy term arising from the Coulombic interactions between charged moieties
- $\boldsymbol{E_{hydrogen\ bonds}}$: energy term referred to the presence or formation of hydrogen bonds

Usually, equations of motions are integrated applying one of the many algorithms using difference methods. MD simulation can be performed in many different statistical ensembles, such as grand canonical (μVT), microcanonical (NVE), canonical (NVT) and isothermal-isobaric (NPT). The constant pressure and temperature can be controlled by adding an appropriate barostat and thermostat. (141)

2.2 Coarse graining techniques

Molecular dynamics simulations on very large systems may require such large computer resources that they cannot easily be studied by traditional all-atom methods. Simulations of processes on timescales longer than 1 microsecond are prohibitively expensive, because they require so many time steps. In these cases, the problem could be avoided by using reduced representations, which are also called coarse-grained models (CG).

Martini force field is a coarse-grained force field suited for molecular dynamics simulations of biomolecular systems. (143) The force field has been parameterized in a systematic way, based on the reproduction of partitioning free energies between polar and apolar phases of a large number of chemical compounds. (143) The Martini model is based on a four-to-one mapping, i.e., on average four heavy atoms plus associated hydrogens are represented by a single interaction center. The four-to-one mapping was chosen as an optimum between computational efficiency on the one hand and chemical representability on the other hand. Mapping of water is consistent with this choice, as four real water molecules are mapped to a CG water bead. Ions are represented by a single CG bead, which represents both the ion and its first hydration shell. To represent the geometry of small ring-like fragments or molecules (e.g., benzene, cholesterol, and several of the amino acids), the general four-to-one mapping approach is too coarse. Ring-like molecules are therefore mapped with a higher resolution of up to two non-hydrogen atoms to one Martini particle.

Based on the chemical nature of the underlying structure, the CG beads are assigned a specific particle type with more or less polar character. The Martini model has four main types of particles: polar (P), non-polar (N), apolar (C), and charged (Q). Within each type, subtypes are distinguished either by a letter denoting the hydrogen-bonding capabilities (d = donor, a = acceptor, da = both, 0 = none) or by a number indicating the degree of polarity

(from 1 = low polarity to 5 = high polarity), giving a total of 18 particle types or 'building blocks'.

Martini, as any other model, has a number of limitations. It is obviously important to know these limitations, both to make sure the model is used appropriately and to further improve the model. With its 4-1 mapping and its particular range of interactions, Martini can reproduce the thermodynamics of a large number of different organic compounds. In many cases it is comparable in accuracy to atomistic models, particularly in thermodynamics, but it also amplifies a number of limitations in atomistic models, where lack of electronic polarizability in the standard force field is one of the main limitations.

However, the wide use of Martini and extensive testing in the original papers and subsequent studies clearly shows the degree of agreement with experiments and atomistic simulations and allows an assessment of whether Martini is accurate enough for a particular application. Recent progress in linking Martini more closely to atomistic simulations through back mapping and through hybrid simulations appears promising in terms of extending the use of Martini simulations to problems that may be outside the current resolution.

2.3 Umbrella sampling

Umbrella sampling is a computational technique used to improve sampling of a system (or different systems) where ergodicity is hindered by the form of the system's energy landscape. Systems in which an energy barrier separates two regions of configuration space may suffer from poor sampling. In Metropolis Monte Carlo runs, the low probability of overcoming the potential barrier can leave inaccessible configurations poorly sampled – or even entirely unsampled – by the simulation. Molecular dynamics simulations are useful to perform dynamic and equilibrium processes of large molecules with atomic detail, but processes which involve large free energy barriers or timescales longer than a microsecond are not feasible to be simulated directly. The potential of mean force (PMF) can be used to represent the equilibrium distribution of one or few relevant conformational variables, angles, distances, etc. with an increased accuracy thanks to a longer sampling and improved force fields. Therefore, if the chosen coordinate is a good reaction coordinate a dynamical propagation on the PMF can simulate the kinetics of the reaction of interest. The most used method for generating a PMF efficiently from molecular dynamics simulations is the umbrella sampling technique. In this method, a reaction coordinate is chosen and by applying

restraining potentials, the system is encouraged to sample regions of conformational space (windows) that would not otherwise be accessible during the direct sampling. The result is a series of histograms which contain the biased distribution of the reaction coordinate from each window. These histograms are then unbiased and combined usually with the aid of the weighted histogram analysis method (WHAM). Remarkably, using a known experimental PMF allowed to choose the optimal restraining potentials eliminating an eventually trial-and-error process. (143)

2.4 Dissipative particles dynamics

Dissipative particle dynamics (DPD) is such a coarse-grained molecular dynamics model, in which the particles represent clusters of molecules that interact via conservative, dissipative and fluctuating forces. (144)

DPD as a particle-based mesoscopic simulation technique, was successfully used to model block copolymers, (145) mesophases, (146) surfactants (147) and polymer phase separations, (148) as well as the assembly of patchy and striped patterns on monolayer protected nanoparticles (149).

The DPD particles (or beads), each representing a group of small molecules or extensive molecular fragments, interact by conservative, dissipative, and random forces, which are pairwise additive. The net force acting on a bead *i* can be expressed as

$$\boldsymbol{F}_{\mathrm{i}} = \sum_{\mathrm{j}\neq\mathrm{i}} (\boldsymbol{F}_{\mathrm{ij}}^{\mathrm{C}}+\boldsymbol{F}_{\mathrm{ij}}^{\mathrm{D}}+\boldsymbol{F}_{\mathrm{ij}}^{\mathrm{R}})$$

and is calculated by summation over all other particles within a certain cutoff radius, r_c, which gives the extent of the interaction range. Let r_c, m, and $k_{\mathrm{B}}T$ be the unit distance, the particle mass, and the thermal energy, respectively.

The conservative force represents the excluded volume interactions between particles *i* and *j* in the dimensionless form

$$\boldsymbol{F}_{\mathrm{ij}}^{\mathrm{C}} = a_{\mathrm{ij}} (1 - r_{\mathrm{ij}}) \hat{\boldsymbol{r}}_{ij},$$

where $\boldsymbol{r}_{ij} = \boldsymbol{r}_i - \boldsymbol{r}_j$, $r_{ij} = |\boldsymbol{r}_{ij}|$, $\hat{\boldsymbol{r}}_{ij} = \boldsymbol{r}_{ij}/r_{ij}$ and a_{ij} is the maximum chemical repulsion between particles *i* and *j*. The intermolecular interaction parameter aij is related to the more common Flory-Huggins interaction parameter through the expression (144)

$$aij = aii + 3.27Xij$$

The dissipative,

$$\boldsymbol{F}_{ij}^{D} = -\gamma\, \omega(r_{ij})^2\, (\hat{\boldsymbol{r}}_{ij} \cdot \boldsymbol{v}_{ij})\, \hat{\boldsymbol{r}}_{ij},$$

and random forces,

$$\boldsymbol{F}_{ij}^{R} = \sigma\, \omega(r_{ij})\, \hat{\boldsymbol{r}}_{ij}\, \zeta/(\delta t)^{-1/2},$$

act as heat sink and source, respectively, and the combined effect of the two forces performs as a thermostat (150), where γ is a friction coefficient related to the thermal noise amplitude σ via the fluctuation−dissipation theorem,

$$\sigma^2 = 2\gamma k_B T,\ \omega(r)$$

ω is a weight function, ζ is a normally distributed random variable with zero mean and unit variance that is uncorrelated for different particle pairs, δt is the time step of an integration scheme, and $\boldsymbol{v}_{ij} = \boldsymbol{v}_i - \boldsymbol{v}_j$ is the relative velocity of the i^{th} and the j^{th} particles. The equations of particle motion, $d\boldsymbol{r}_i/dt = \boldsymbol{v}_i$ and $d\boldsymbol{v}_i/dt = \boldsymbol{F}_i$, are typically solved using as integration scheme the velocity-Verlet algorithm. (151)

Finally, when modelling chains two additional forces are acting between bonded beads: a harmonic spring connecting two adjacent particles *i* and *j*

$$\boldsymbol{F}_{ij}^{B} = k_b(r_{ij} - r_0)\, \hat{\boldsymbol{r}}_{ij},$$

where k_b is a spring constant and r_0 the equilibrium distance between the particles, and

$$\boldsymbol{F}_{ijz}^{A} = 1/2\ k_\theta \sin(\theta_0\text{-}\theta_0),$$

where k_θ is a spring constant and θ_0 the equilibrium angle between adjacent beads triples *ijz* in a row.

Chapter 3. *Understanding the organization of mixed self-assembled monolayer-protected nanoparticles*

As explained in Chapter 1, when mixed self-assembled monolayers (SAMs) of immiscible ligands are employed to coat gold nanoparticles (AuNPs), nanoscale domains tend to form spontaneously within the surface ligand shell. This peculiarity provided access to a variety of possible patterns and allowed to tune their morphological characteristics varying a series of easy-to-control parameters such as surfactant length, NP radius, as well as less governable parameters such as the degree of immiscibility and stoichiometry of the SAM components (152). For these reasons, being able to understand the properties responsible for this auto-organization is essential for designing new systems with controlled morphologies and properties.

In this thesis, we focused our attention on investigating the phase segregation in SAM-AuNPs covered by different mixtures of fluorinated (*F*-) and hydrogenated (*H*-) thiolates, exploiting the well-known immiscibility of hydrocarbons and fluorocarbons. In fact, the spontaneous phase separation in supramolecular aggregates of hydrogenated/fluorinated amphiphiles is well documented for several of such systems (e.g. micelles, Langmuir and Langmuir Blodgett films) including two-dimensional self-assembled monolayers on gold surfaces (2D SAMs). (153) Furthermore, fluorinated amphiphiles are receiving increasing interest for biological/biomedical applications as they confer useful properties to the materials they are linked to, such as inertness, facilitated cellular uptake, avoidance of protein denaturation and reduced toxicity. (154-156) Additionally, being NMR active, fluorine nuclei assist in probing biological interactions and may lead to novel supramolecular contrast agents for bioimaging (157). 19F held great promise as alternative nuclide for in vivo and ex vivo MRI for its high sensitivity (83% relative to 1H) and 100% natural abundance. Importantly, in animal bodies essentially no endogenous 19F is detectable by MRI, thus eliminating interference from background signals. NP-based 19F MRI will also enable image quantification, a feature not available in any current routine diagnostic imaging. (60)

This calls for a more in-depth investigation on the role of fluorinated ligands in monolayer-protected-nanoparticles especially when dealing with biological applications. Having this in mind, we developed computational procedures, both at atomistic and coarse-grained level, to study the structure of SAM-protected AuNPs. Concomitantly, using these results we offered the basis to develop our understanding of the design rules required to control the formation of specifically patterned monolayer-protected NPs.

3.1 Fluorinated and hydrogenated alkanethiolates coated gold nanoparticles

A large set (see Appendix A) of gold NPs with an average diameter of 2-4 nm were prepared and functionalized with *F*- and *H*-thiolate ligands of (Figure 4):

- *different length*: **NP-C16/F6**, protected by hexadecanethiol (**HC16**) and 1*H*,1*H*,2*H*,2*H*-perfluorooctanethiol (**HF6**), and **NP-C12/F6**, coated by mixtures of dodecanethiol (**HC12**) and **HF6**;
- *equal length*: **NP-C12/F10**, coated by **HC12** and 1*H*,1*H*,2*H*,2*H*-perfluorododecanethiol (**HF10**), and **NP-C8/F6**, protected by mixtures of octanethiol (**HC8**) and **HF6**;
- *increased steric hindrance* **NP-brC12/F6**, featuring mixtures of 3-methyldodecane-1-thiol (**HbrC12**) and **HF6**.

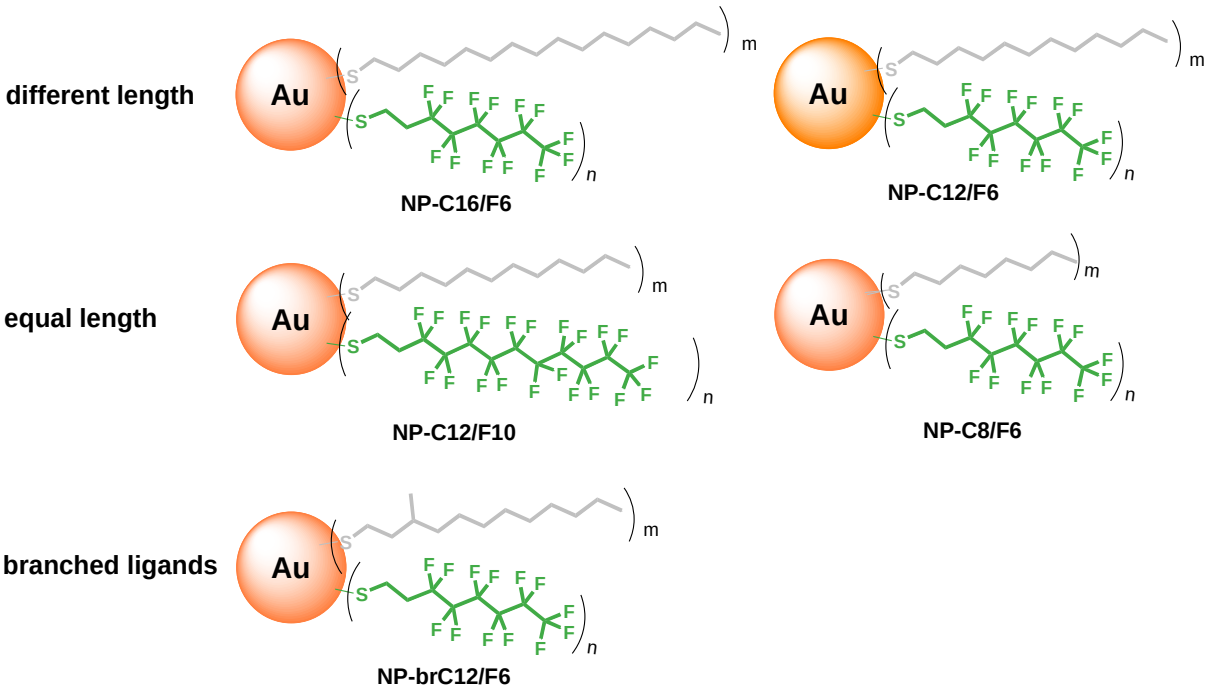

Figure 4: 2-4 nm core diameter AuNPs decorated by F- and H-thiols.

Gold nanoparticles **NP-C16/F6**, **NP-C8/F6**, and **NP-brC12/F6** were prepared by direct synthesis, whereas **NP-C12/F6** and **NP-C12/F10** were obtained by place exchange reaction from narrowly dispersed **NP-C12**, in turn prepared following the method of Miyake. (158) All samples were fully characterized using UV-VIS, TEM, TGA, and standard NMR experiments. Preparation and characterization of all systems was carried out by the group of Prof. Lucia Pasquato (Department of Chemical and Pharmaceutical Sciences, University of Trieste).

The evaluation of the morphology of these mixed monolayer-protected gold NPs may be difficult because of a large number of limitations such as their low solubility in common organic solvents, presence of impurities, or the slippery nature of the NP surface, limits the number of experimental techniques suitable to study their morphology. To overcome these issues, in this work, we adopted an integrated and complementary experimental/computational approach for the characterization of these systems. Specifically, our experiments relied on 1D and 2D ^{19}F NMR (159). The theoretical investigation was based on a predictive multiscale molecular simulation protocol that combines atomistic and coarse-grained calculations.

Overall, this study clarified how the variation of some specific parameters (as the type and ligand ratio) might influence the morphology of a SAM and the results obtained permit to design some rules to achieve a precise control of inorganic nanoparticles protected by specifically patterned monolayers.

Full details of the experimental work can be found in *M. Sologan, D. Marson, S. Polizzi, P. Pengo, S. Boccardo, S. Pricl, P. Posocco, L. Pasquato, "Patchy and Janus nanoparticles by self-organization of binary mixtures of fluorinated and hydrogenated alkanethiolates on the surface of a gold core". ACS Nano,* 2016, 10 (10), pp 9316–9325.

3.1.1 Computational details

The initial structure of the nanoparticle core was constructed by arranging DPD beads (Au) on a *fcc* lattice into the desired geometry shape and diameter using OPENMD software (v. 2.3) (160). The icosahedral shape was adopted as one of the most thermodynamically stable crystalline form for gold below 10 nm. (161)

Solvents (*i.e.*, chloroform (CHL) and hexafluorobenzene (HFB)) were modelled as a single bead. Each ligand was represented by a flexible chain model of beads connected by harmonic springs. The coarse-grained scheme for the ligands (Figure 5: An example of the coarse-grained scheme showing the DPD mapping employed.) is based on four different types of beads: bead *S*, representing the sulfur head group, beads *C* and *M* denoting the linear and branched parts of hydrocarbon ligands, respectively, bead *F* mimicking the perfluorocarbon component of the chain.

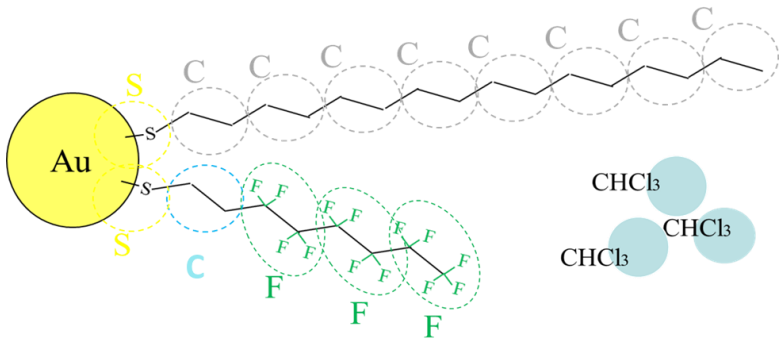

Figure 5: An example of the coarse-grained scheme showing the DPD mapping employed. Solvents were modelled as a single bead.

Accordingly, the structure pertaining to each ligand is reported in Table 1.

Ligand type	*Model*
F6	$SC(F)_3$
F10	$SC(F)_5$
C8	$S(C)_4$
brC12	$SCM(C)_4$
C12	$S(C)_6$
C16	$S(C)_8$

Table 1: Coarse-grained model of each H-chain and F-chain

The mesoscale topology was assessed by matching the atomistic (calculated by molecular dynamics (MD) simulations) and mesoscale pair-correlation functions for each ligand chain. MD and DPD pair correlation functions were computed from equilibrated MD/DPD models obtained applying the same procedure proposed by our group (162) for hydrocarbon or perfluorocarbon ligands terminating with a short poly(oxoethylene) moiety (as well as mercaptoundecanesulfonate/octanethiol ligands) and reported briefly below. First, a 1 μs MD simulation at 300 K was performed on each ligand molecule in vacuum starting from the optimized molecular model. Nose-Hoover (Q = 1) was used to thermostat the temperature and the velocity Verlet algorithm to integrate the equations of motion with a time step of 0.5 fs. Atomic interactions were described by PCFF force field (FF). (163) Then, DPD simulations were performed on single molecules in vacuum having set equal all the bead-bead interactions. A time step of 0.04 was adopted in each DPD run. This also led to obtain chain beads with volumes reasonably close to each other (~ 55 $Å^3$).

Once the topology, i.e. number, type and connectivity of beads, has been retrieved, mesoscale pair-pair interaction parameters a_{ij} were derived employing the same recipe reported in our previous works (164) for modified gold NPs, starting from the relative atomistic energies, as summarized in the next paragraph.

According to this approach, a suitable atomistic model of gold/ligands/solvent interface was built, optimized, and subject to 10 ns of NVT simulation at 300 K. In order to obtain a reasonable sampling of the *H*- and *F* chain conformational space, five different configurations of the *H*- and *F* chains were constructed, using the *Amorphous Builder* module of *Materials Studio*, which employs a version of the *Rotational Isomeric State* (*RIS*) method (165) for generating chain configurations. Each structure was then relaxed and subjected to a combined molecular mechanics/molecular dynamic simulated annealing

protocol (166) and then employed to build the interface in a pseudo-2D periodic system. The ligand chains were initially placed perpendicular to the gold surface plane with their sulfur head group randomly distributed on the surface. The distance between the gold surface and the sulfur atom was fixed at an average value of 2.38 Å (167), and the velocity of each sulfur atom was set to zero along the direction perpendicular to the surface plane.

The modified PCFF FF, optimized by Heinz and co-workers (168) for hybrid organic and metal interfaces, including gold (INTERFACE FF), was adopted in the atomistic calculations. NVT MD simulations of the ligand/gold/solvent interfaces were run at 300 K for 10 ns, applying the Ewald summation method (169) for treating Coulomb interactions and a cut-off of 7Å for van der Waals forces; an integration step of 2 fs, and a Nose-Hoover thermostat (Q ratio = 1) were also adopted. All MD simulations were carried out using *Materials Studio* (v. 5.0, Accelrys, San Diego, CA) molecular simulation package. The energetic analysis was conducted on the equilibrated portion of the MD trajectory, and all energy values were averaged over 100 configurations.

According to the theory (see Chapter 2), the intra- and intermolecular interactions between DPD particles are expressed by the conservative parameter a_{ij}, which inherits the chemical information of the system. Here, we employed a consolidated procedure that correlated the interaction energies estimated from atomistic MD simulations to the mesoscale a_{ij} parameter values, rescaled onto the corresponding mesoscale segments. (170)

Thus, we set the adimensional bead-bead interaction parameter for chloroform-chloroform interaction equal to $a_{CHL-CHL} = 30.1$, based on the direct relationship with their isothermal compressibility at room temperature. (171) The gold-gold interaction parameter was set to a lower value (i.e. $a_{Au-Au} = 49.6$), based on our previous calculations. (170) Once these two parameters were set, and their values associate with the corresponding values of the rescaled DPD energies, all the remaining bead-bead interaction parameter for the DPD simulation could be easily obtained, starting from the atomistic binding energies following the same procedure described in detail in previous papers of our group. (170) Therefore, we employed the following values for a_{ij}: $a_{S-S} = 48.3$, $a_{C-C} = 50.1$, $a_{M-M} = 53.2$, $a_{F-F} = 56.8$, $a_{HFB-HFB} = 46.9$, $a_{S-C} = 69.5$, $a_{S-M} = 70.3$, $a_{M-C} = 65.7$, $a_{F-S} = 73.8$, $a_{F-C} = 66.0$, $a_{F-M} = 76.2$, $a_{Au-S} = 1.90$, $a_{Au-C} = 55.4$, $a_{Au-M} = 56.4$, $a_{CHL-C} = 51.2$, $a_{CHL-M} = 48.7$, $a_{CHL-F} = 57.3$, $a_{HFB-C} = 61.3$, $a_{HFB-M} = 49.1$, $a_{HFB-F} = 50.2$, $a_{HFB-CHCL} = 54.2$ r_C/k_bT.

Each ligand was placed close to the NP surface and oriented outward with the head-tail vector along the radial direction, ensuring that the corresponding position on the surface did

not have clash with any previously positioned ligand using Packmol package. (172) The appropriate number of *H*- and *F*- chains was inserted in order to reproduce the experimental grafting density (*i.e.*, the number of ligands for nm^2 of surface). A random configuration was imposed to arrange the chains on the gold surface. Then, the modified NP was solvated again by Packmol. Each system was tested on three independently generated starting configurations.

A $25r_c$ x $25r_c$ x $25r_c$ simulation box was adopted, placing the monolayer protected NP in the middle of the periodic cell. To avoid finite size effect, the distribution of the solvent from the centre of mass of the NP was checked in preliminary simulation runs. All Au beads were forced to move as a rigid body during the calculation. At the same time, the sulfur heads can diffuse laterally on the NP surface during the entire simulation time. Optimized adimensional values for bond and angle parameters, obtained from the matching of the pari-pair correlation functions described above, , were employed for both alkane and perfluorocarbon thiols: k_b(C-C) = 10, r_0(C-C) = 0.60, k_θ(C-C-C) = 10, θ_0 (C-C-C) = 110, k_b(C-F) = 10, r_0 (C-F) = 0.65, k_b(F-F) = 20, r_0 (F-F) = 0.69, k_θ(C-F-F) = 0, θ_0 (C-F-F) = 180, k_θ(F-F-F) = 10, θ_0 (F-F-F) = 110.

Each initial configuration was first relaxed for $1x10^4$ steps and a time step of Δt = 0.01. Then, at least additional $6x10^6$ time steps (Δt = 0.02) were performed increasing the interaction parameters till their actual value. System equilibration was assessed monitoring temperature, pressure, density, and potential energy behaviour. We did not observed chain penetration into the gold core during the simulation time.

In systems dissolved in hexafluorobenzene, NPs were first equilibrated in chloroform and then a proper amount of CHL beads was replaced by HFB beads, and the resulting systems were then equilibrated.

The cut-off radius r_c, the particle mass m_i, and k_BT are taken as units of length, mass and energy. Preliminary run tests were performed by means of Culgi (v.9.0, Culgi B.V., Leiden, The Netherlands). All mesoscale production runs and analysis were performed using LAMMPS (173) running on GPUs and VMD. (174)

3.1.2 Nanoparticles coated by branched ligands

The initial hypothesis that a branched structure of the hydrogenated ligand reduced the formation of phase-segregated domains was confirmed by the equilibrium morphologies collected from the corresponding DPD calculations (Figure 6). These simulation structures clearly prove that the two ligands do not tend to form compact domains and they prefer to remain isolated, resulting in a random organization of the monolayer regardless of the monolayer composition and dimension of the gold core. These evidences agree well with previous literature data on the organization of monolayers comprising branched thiolates. (101) The chemical shift of the CF_3 groups of ligand F6 as a function of the percentage of the fluorinated ligand into the monolayer for the NP-brC12/F6 system is shown in Figure 6. The linear decay suggested that the average composition of the first nearest neighbor shell for one ligand coincided with the overall composition of the monolayer in agreement with the 3D organization predicted by the theoretical calculations.

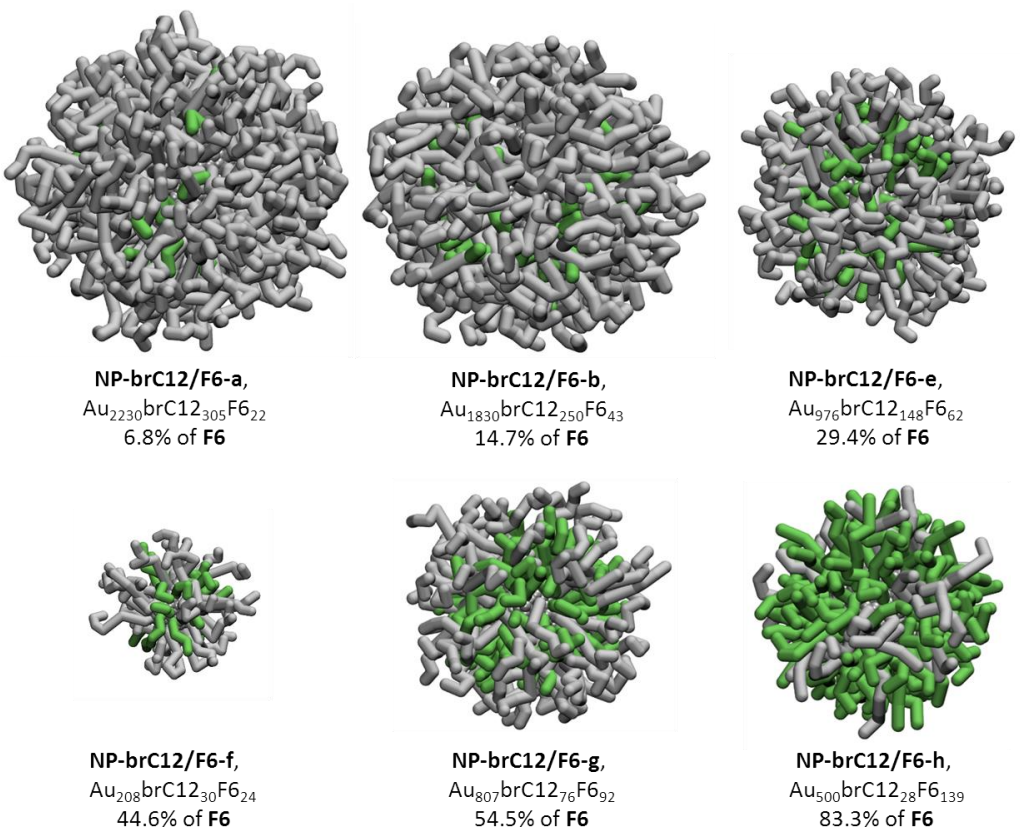

*Figure 6: Equilibrium morphologies of **NP-brC12/F6** (color code: grey, **brC12**; green, **F6**) NPs as obtained by the mesoscale simulations. Solvent is omitted for clarity.*

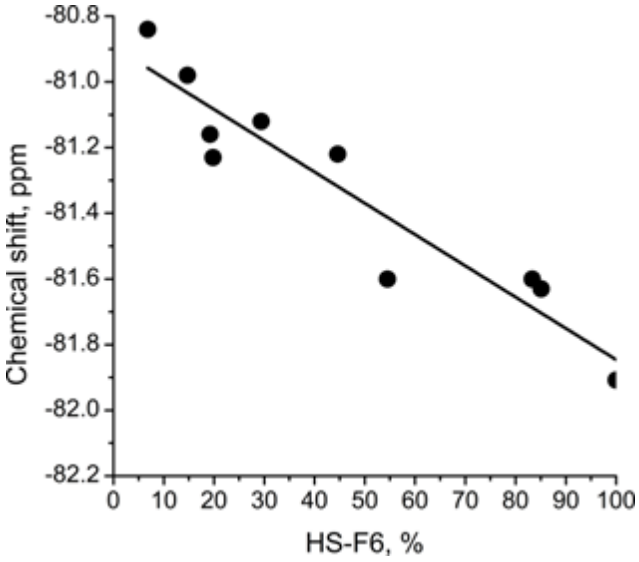

Figure 7: Chemical shift (δ) variation of CF3 groups increasing the percentage of the F-ligand in the monolayer of NP-brC12/F6. Solid line serves as eye guide only.

3.1.3 Nanoparticles coated by ligands of equal length

The equilibrium morphologies obtained from the mesoscale simulation of the **NP-C12/F10** systems (Figure 8) revealed that the ligands are phase-separated (Janus morphology) in line with a previously reported theoretical prediction on nanoparticles protected by ligands of equal length. (65) To our knowledge, this is also the first example of a 3D monolayer with Janus morphology obtained by place-exchange in the absence of external forces.

Moreover, a steep decay in the chemical shift was observed when F10 was less than 40%, followed by a smooth decrease of the chemical shift up to the 100% of F10. This indicated a strong evolution of the surface area at the H-/F interface in the first region of the curve, which determined a significant upfield shift of the signals of the fluorinated ligands. When the loading increases over 60%, no significant changes at the interface were observed; accordingly, the chemical shift remains nearly constant (Figure 9). This behavior is well supported by the structures obtained by simulation.

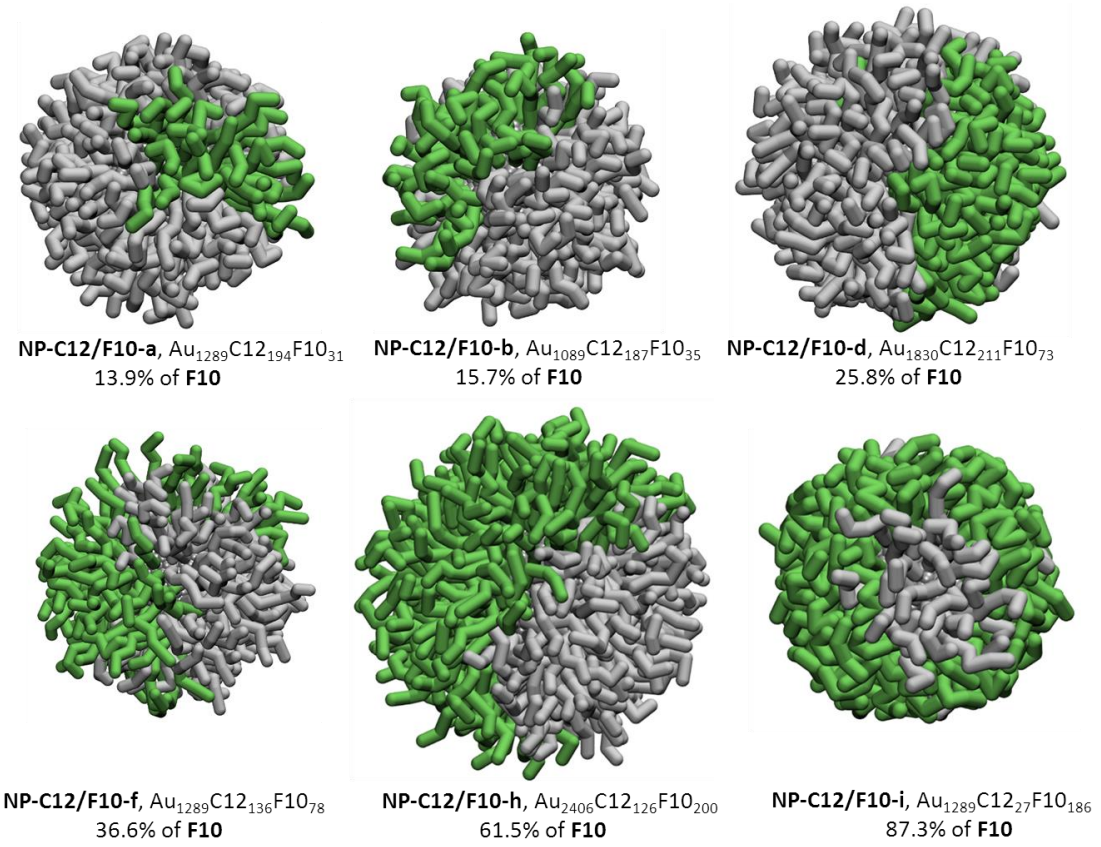

*Figure 8: Equilibrium morphologies of **NP-C12/F10** (color code: grey, **C12**; green, **F10**) obtained by the mesoscale simulations. Solvent is omitted for clarity.*

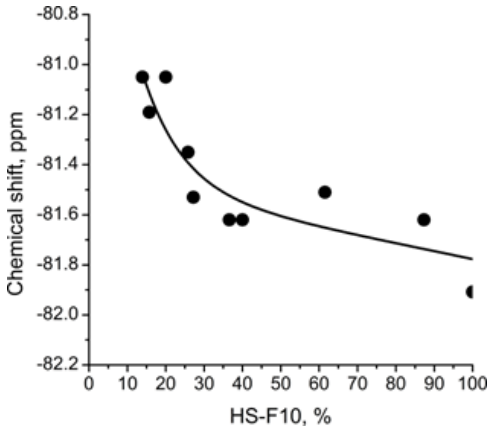

Figure 9: Chemical shift (δ) variation of CF_3 groups increasing the percentage of the F-ligand in the monolayer of NP-C12/F10. Solid line serves as eye guide only

NP-C8/F6, an alternative system featuring ligands of comparable lengths (Figure 10), was found to be characterized by a different SAM morphology and chemical shift behavior (Figure 11). This was somewhat unexpected since, intuitively, the monolayers of **NP-C8/F6**

and the previously discussed **NP-C12/F10** should both presented a similar Janus-like organization.

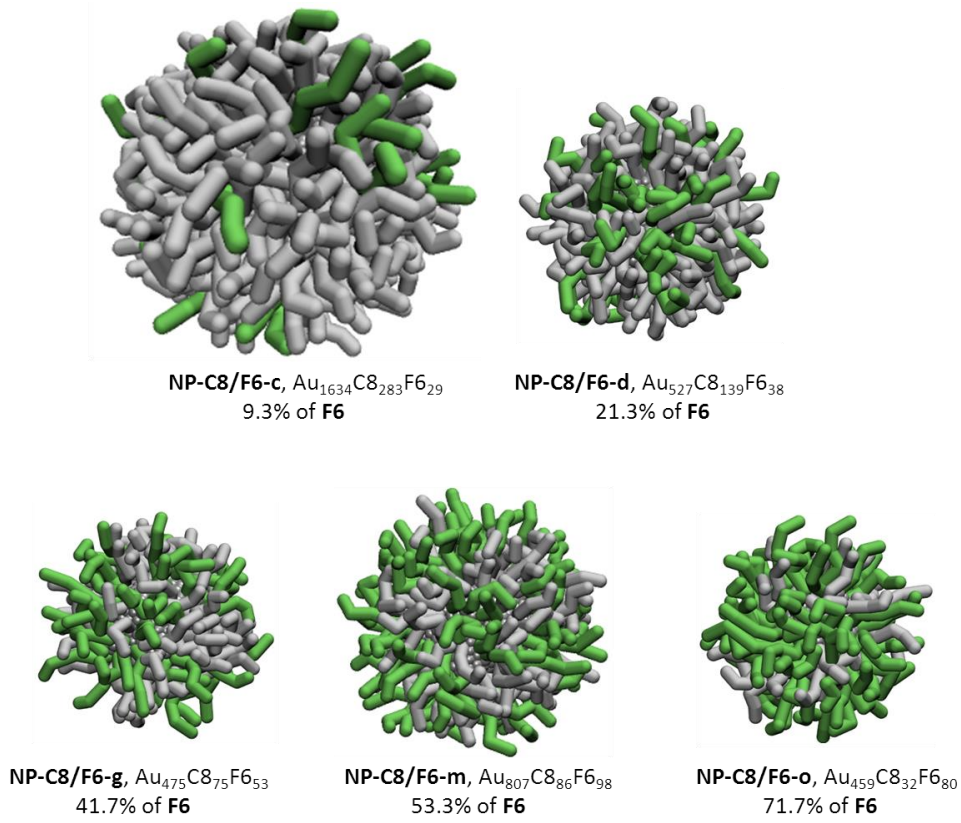

*Figure 10: Equilibrium morphologies of **NP-C8/F6** (color code: grey, **C8**; green, **F6**) NPS as obtained by the mesoscale simulations. Solvent is omitted for clarity.*

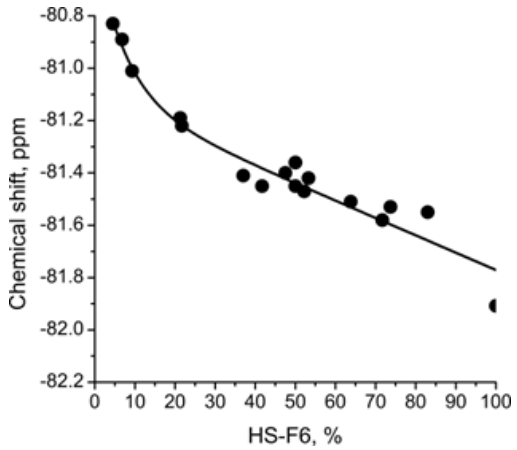

Figure 11: Chemical shift (δ) variation of left) CF3 groups and right) 7-CF2 nuclei increasing the percentage of the F-ligand in the monolayer of NP-C8/F6. Solid line serves as eye guide only.

The corresponding mesoscopic simulations, predicted that the **C8** and **F6** thiolates do not phase-separate in two distinct domains. On the contrary, below 20%, DPD showed that the

F- thiolates preferred to remain isolated, and an essentially random organization was observed. By increasing the loading, the fluorinated ligands did not form extended domains; rather, they tended to remain confined in small patches or formed irregular clusters when the stoichiometric ratio was further increased. Overall, the morphology of **NP-C8/F6** nanoparticles remained ill defined. We hypothesize that the shorter chain length of F6 with respect to F10 reduces the overall strength of the fluorophilic interactions, making the formation of fluorinated domains less favourable. In addition, the difference in steric hindrance between H- and F- thiolates may represent a bias in the organization of the thiolates when this geometrical mismatch is not counterbalanced by the occurrence of strong fluorophilic interactions.

3.1.4 Nanoparticles coated by ligands of different length

Mesoscale simulations on selected samples of **NP-C16/F6** (Figure 12) revealed that the SAM morphology organized in striped domains, even when 20% of the **F6** thiolate is present. For these NPs, the gain in entropy due to the difference in length and the immiscibility of *H*- and *F*-ligands is sufficient to overcome the loss of enthalpy, in line with previously reported data about the organization of mixed monolayers composed of thiols having different length. Furthermore, the striped organization can explain why some samples of **NP-C16/F6** are soluble in chloroform even at percentages of the fluorinated ligands into the monolayer up to 73%. We thought that the sufficiently long hydrogenated chain might mask the short-fluorinated ones, screening out the inter-nanoparticles interactions between fluorinated domains if the width of the stripes is small enough, 0.75 nm on average. At values of **F6** lower than 40%, increasing the number of fluorinated ligands resulted in striped-domains of *F*-chains different in size. Once the stripes are completely formed (approximately at **F6** > 40%), the further addition of fluorinated ligands did not influence the morphology, as the incoming thiols located inside a previously formed stripe. At percentages of the fluorinated thiolate higher than 80%, **F6** chains prevail, reducing the size of the *H*-domains. The chemical shift (Figure 13) versus composition curve is composed of three regions: an initial, almost linear decay is obtained in the composition range of 0−40%, suggesting that by increasing the percentage of **F6**, even over 80%, the presence of fluorinated thiolates did not influence the previously formed F-/H- stripe due to their favorable location inside the preexisted domains. These results were in great agreement with the computational founding.

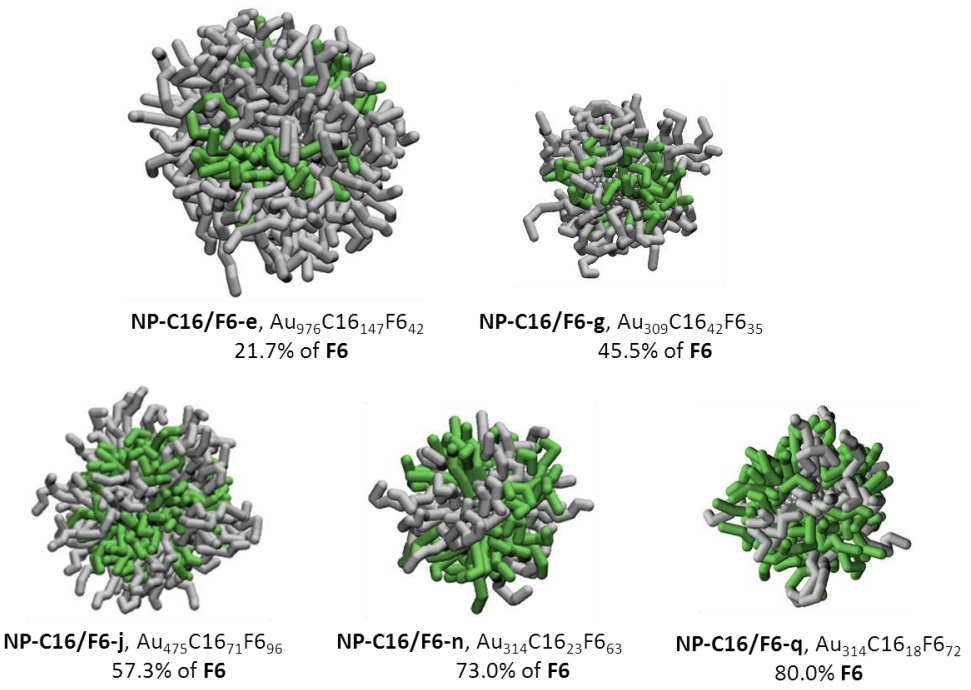

*Figure 12: Equilibrium morphologies of selected of **NP-C16/F6** (color code: grey, **C16**; green, **F6**) NPs as obtained by mesoscale simulations. Solvent is omitted for clarity.*

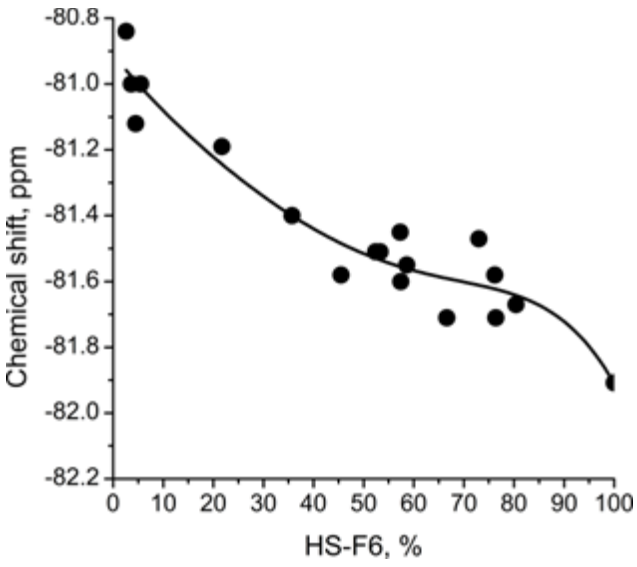

Figure 13: Chemical shift (δ) variation of CF3 groups increasing the percentage of the F-ligand in the monolayer of NP-C16/F6. Solid line serves as eye guide only.

Mesoscale simulations of **NP-C12/F6** systems did not show a well-defined, ordered organization as a function of the **F6** content. As clearly shown in Figure 14, sometimes stripe-like domains are formed, while, at the same time, irregular patches could be also

observed. Specifically, when 10-15% of the fluorinated ligands were introduced into the monolayer, they form small patches of a few fluorinated chains. When the loading of **F6** exceeds 30%, elongated patches or stripe-like domains appear, and the dimensions of the relevant domains increase to 0.75-0.80 nm, on average.

At percentages higher than 60% of *F*- thiolates, the shape of the domains is again predominantly patchy. The predicted morphologies are also consistent with the solubility properties of **NP-C12/F6**. Up to 40% of **F6** in the monolayer, these systems are soluble in chloroform–indicating that the surfaces of the fluorinated domains are small enough to be efficiently shielded by the hydrogenated chains. Increasing the **F6** content leads to an enlargement of the fluorinated domains, and the *H*- ligands do not reduce inter-particles interactions leading to a change of the solubility properties.

Looking at the chemical shift of CF_3 groups (Figure 15), a plateau region was found until the 25% of F6s were introduced in the monolayer; this trend was followed by a decrease of the chemical shift for small additions of F6 into the monolayer. A plateau region was observed up to the 100% F6, indicating that at lower and higher loadings of F6 there is no marked difference in the surroundings of the fluorinated ligands at the interface.

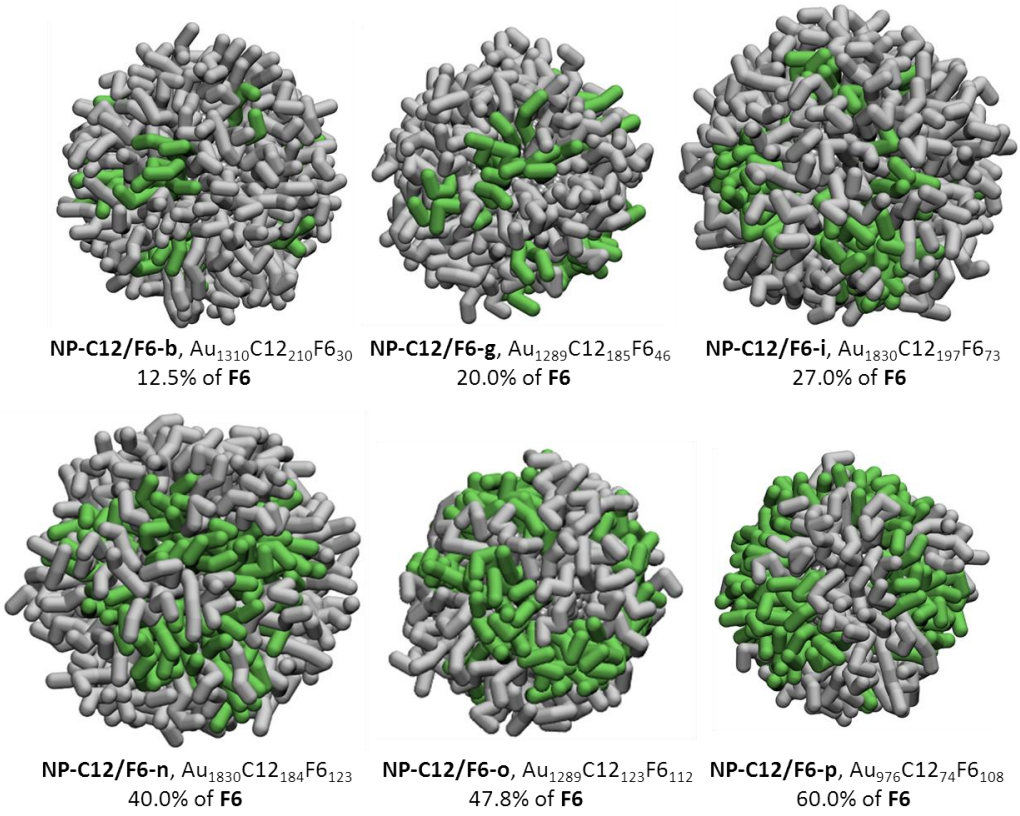

*Figure 14: Equilibrium morphologies of selected **NP-C12/F6** (color code: grey, **C12**; green, **F6**) NPs as obtained by mesoscale simulations. Solvent is omitted for clarity.*

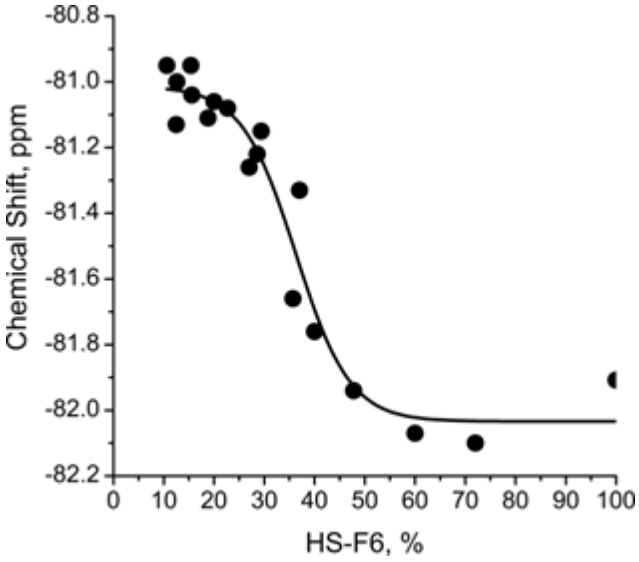

Figure 15: Chemical shift (δ) variation of CF3 groups increasing the percentage of the F-ligand in the monolayer of NP-C12/F6. Solid line serves as eye guide only.

Overall, the results pointed out that, besides the higher immiscibility between *H*- and *F*-ligands, other key parameters, such as the high steric hindrance and rigidity of the fluorinated chains, influenced the morphology of the monolayer. Therefore, only when the mismatch of ligands length was equal to eight carbon atoms, stripe-like domains were formed (**NP-C16/F6** system), driven by entropy gain. Conversely, when a difference in length of four-carbon atoms was present domains appeared as patches or elongated patches (**NP-C12/F6** system). Ligands of the same length self-organized in Janus domains (**NP-C12/F10**), as expected. However, if both ligands were shorter as in **NP-C8/F6** case, the experimental and theoretical results suggested the formation of a SAM with no specific morphology. Finally, the presence of a branched ligand in the monolayer (**NP-brC12/F6** system) promoted a random organization.

3.2 Water-soluble NPs

Decorating NPs with hydrophilic and uncharged polymers such as poly-ethylene glycol (PEG), a process known as "PEGylation", as well as functionalizing nanoparticles with stealth polymers (e.g., charged or zwitterionic polymers) has become a common strategy to impart water solubility and resistance to nonspecific protein adsorption, promoting their

usage for numerous biomedical applications, such as bioimaging, biosensing, drug delivery, diagnostics, and therapy. (190)

3.2.1 Polyethylene Glycol Coated Nanoparticles

Starting from the design principles obtained from the previous analysis and aiming to investigate the behavior of mixed SAM-protected AuNPs once in contact with a biological environment, F- and H- ligands were modified adding polyethylene glycol (PEG) chains of different length on the top (Figure 16).

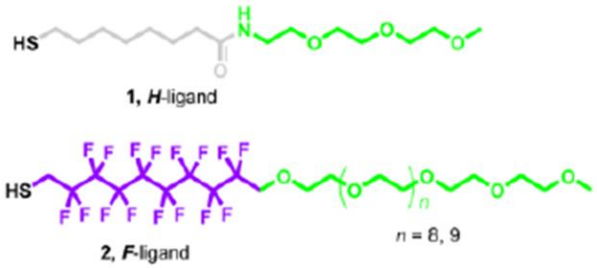

Figure 16: chemical structure of the PEGylated F- and H- ligand

We considered two mixed-monolayer C8TEG/F8PEG AuNPs (namely M1-C8T/F8P and M2-C8T/F8P), as well as the reference homoligand AuNPs for comparison, with only F8PEG (indicated as F8P) or C8TEG (C8T), as well as those formed with C8PEG ligands (C8P). Some of the relevant characteristics of these SAM-AuNPs are summarized in Table 2.

SAM-AuNP	Core diameter [a] (nm)	Core composition [b]	Monolayer composition [c]		NP diameter [d] (nm)
			Ligand ratio	N° ligands	
M1-C8T/F8P	1.6 ± 0.4	Au_{140}	C8TEG: F8PEG	24: 32	6.6 ± 0.1
M2-C8T/F8P	1.9 ± 0.7	Au_{260}	C8TEG: F8PEG	20: 36	6.7 ± 0.2
F8P	2.4 ± 0.7	Au_{459}	F8PEG	76	7.6 ± 0.2
C8T	2.0 ± 0.3	Au_{223}	C8TEG	73	6.2 ± 0.1
C8P	1.7 ± 0.3	Au_{201}	C8PEG	69	7.3 ± 0.1

Table 2: Main features of SAM-AuNPs used in this investigation. [a] From TEM measurements. [b] Calculated from TGA and TEM analysis. [c] Calculated from TGA analysis and for mixed-monolayers using the ligand ratio determined by ^{1}H NMR on decomposed NPs. [d] From atomistic simulations, considering both core and ligand shell.

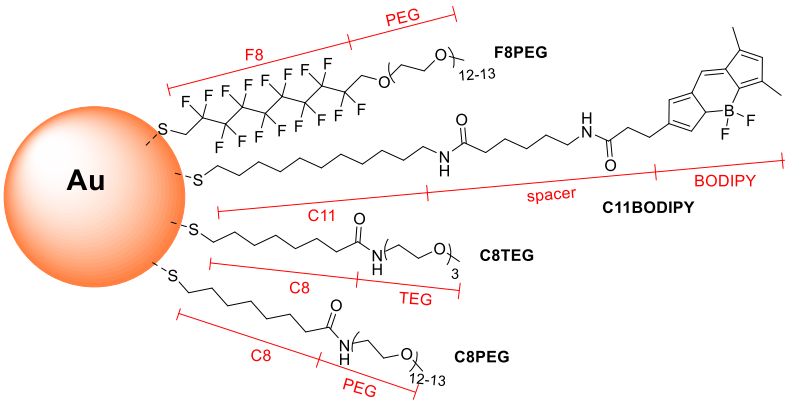

Figure 17: Structure of thiolated ligands used in this study to pattern the surface of AuNPs.

While C8P were very hydrophilic, due to the thick polar PEG surface layer (see Figure 17), C8T, with the thin TEG surface layer, were significantly more hydrophobic. The other NPs had an intermediate hydrophilicity, due to the presence of the amphiphilic F8PEG chains.

The extensive length of ligand chains (more than 14 atoms) and the presence of an outer layer of disordered PEG chains prevented the use of common experimental techniques as STM, AFM, X-ray to assess the morphology of the monolayer. Thus, the only way to have a detailed picture of the molecular organization of the thiolates was to resort to a theoretical approach.

3.2.2 Computational details

3.2.2.1 Dissipative Particle Dynamics

The spontaneous assembling process of the ligands on the gold surface was investigated by means of Dissipative Particle Dynamics (DPD). The set of nanoparticles considered for this study was simulated following the procedure described in Section 3.1.1. Accordingly, we will report here only the parameters pertaining to these specific systems. The initial structure of the NP core was constructed by arranging DPD beads (Au) on a *fcc* lattice into the desired icosahedral shape and diameter. Each ligand was represented by a flexible chain model of beads connected by harmonic springs of composition reported in Table 3. Solvent (water) and ions were modelled as a single bead.

Ligand type	*Model*
C8P	$S(C)_3(F)_3$
C8T	$S(C)_3(P)_2$
F8T	$S(F)_4(P)_2$
F8P	$S(F)_4(P)_{10}$

Table 3: Coarse-grained model of each ligand considered in the study.

As described above, DPD pair-pair interaction parameters and ligand topology may be derived using a multiscale simulation protocol, combining atomistic and coarse-grained simulation. (191-195) Accordingly, we derived the following values for a_{ij}: $a_{C\text{-}C}$ = 51.6, $a_{C\text{-}F}$ = 66.0, $a_{C\text{-}P}$ = 60.1, $a_{C\text{-}S}$ = 72.0, $a_{C\text{-}W}$ = 86.6, $a_{F\text{-}F}$ = 58.8, $a_{F\text{-}P}$ = 65.1, $a_{F\text{-}S}$ = 80.0, $a_{F\text{-}W}$ = 96.6, $a_{P\text{-}P}$ = 51.6, $a_{P\text{-}S}$ = 75.0, $a_{P\text{-}W}$ = 51.6, $a_{S\text{-}S}$ = 51.6, $a_{S\text{-}W}$ = 80.0, $a_{W\text{-}W}$ = 51.6 r_C/k_BT.

A $25r_c$ X $25r_c$ X $5r_c$ simulation box was adopted, placing the monolayer protected NP in the middle of the periodic cell. Optimized adimensional values for bond and angle parameters were employed for both alkane and perfluorocarbon thiols: k_b(F-S) = 10, r_0(F-S) = 0.60, k_θ(F-F-S) = 0, θ_0 (F-F-S) = 180, k_b(F-F) = 10, r_0(F-F) = 0.69, k_θ(F-F-F) = 10, θ_0 (F-F-F) = 110, k_b(F-P) = 10, r_0(F-P) = 0.69, k_θ(F-F-P) = 10, θ_0 (F-F-P) = 109, k_b(P-P) = 10, r_0(P-P) = 0.62, k_θ(F-P-P) = 10, θ_0 (F-P-P) = 109, k_θ(P-P-P) = 10, θ_0 (P-P-P) = 108, k_b(C-S) = 10, r_0(C-S) = 0.50, k_θ(C-C-S) = 0, θ_0 (C-C-S) = 180, k_b(C-C) = 10, r_0(C-C) = 0.60, k_θ(C-C-C) = 10, θ_0 (C-C-C) = 110, k_b(C-P) = 10, r_0(C-P) = 0.61, k_θ(C-C-P) = 5, θ_0 (C-C-P) = 109, k_b(P-P) = 10, r_0(P-P) = 0.62, k_θ(C-P-P) = 5, θ_0 (C-P-P) = 109.

Each initial configuration was first equilibrated for $1x10^4$ steps and a time step of Δt=0.01τ. Then, additional $8x10^6$ time steps (Δt=0.02 τ) were performed increasing the interaction parameters till their actual value.

3.2.2.2 Atomistic simulation

Once equilibrated, the CG-NP structures were mapped back to all-atom (AA) configurations to gain insights into molecular-level details of ligand and shell properties. The monolayers were equilibrated in explicit water and ions (Na+ and Cl-) at room temperature. All systems were minimized by 1000 steps of Steeped Descent followed by 3000 steps of Conjugated Gradient algorithms. The temperature was then raised to 300 K in 20 ps of NVT molecular dynamics (MD) simulation (Langevin thermostat, time step of 1 fs, collision frequency 1.0),

followed by the equilibration of the density for 10 ns with a Berendsen barostat (pressure relaxation time of 2 ps, time step of 2 fs). At the end, we switched to a Monte Carlo barostat and performed data collection for a total of 20 ns. AA simulations were performed by means of AMBER 14 suite of software (196), employing gaff2 (197, 198) forcefield.

3.2.2.3 Results

CG calculations showed that the H- and F- ligands self-organize in well-separated Janus type domains for M1-C8T/F8P, while regular stripes of alternating C8TEG and F8PEG thiols characterize the shell of M2-C8T/F8P system (Figure 18). This is in line with a previously described conceptual framework on how parameters such as core size, ligand ratio and length mismatch concur to determine C8TEG/F8PEG domains shape. (199) In that context, we proposed that for small Au radius (~ 1.6 nm) the thiols tend to organize in two distinct domains, as predicted for M1-C8T/F8P. Slightly larger Au cores instead result in self-sorting of ligands into alternating ribbons, as this maximizes entropy and minimize enthalpy contribution (as is the case for M2-C8T/F8P). The final structures can be compared to those of the homoligand Au-NPs in Figure 18.

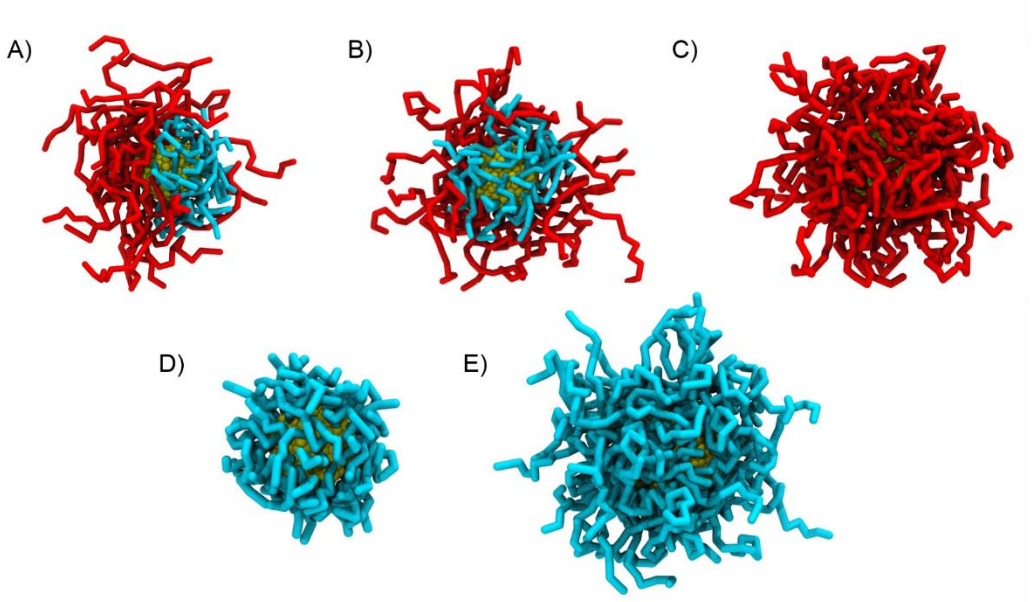

Figure 18: ***Self-assembled mixed monolayer organization of SAM-^{Au}NP.*** *M1-C8T/F8P (A), M2-C8T/F8P (B), F8P (C), C8T (D), and C8P (E) as obtained from coarse-grained calculations in solvent. Color code: red, F8PEG-thiolates; cyan, C8TEG/C8PEG-thiolates; yellow, gold core. Water and ions are not shown for clarity.*

A detailed molecular-level picture of ligand conformation and monolayer properties was obtained from atomistic MD simulations, starting from the corresponding solvated CG structures. (see Figure 19).

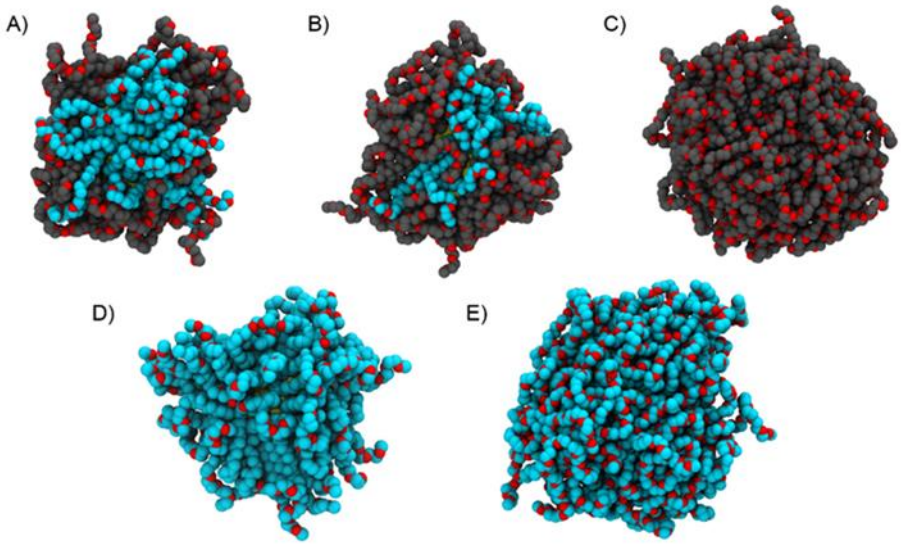

Figure 19: ***Examples of simulation snapshots obtained from AA-MD.*** *The simulations, run in solvent, illustrate ligand organization on the gold surface for (A) M1-C8T/F8P, (B) M2-C8T/F8P, (C) F8P, (D) C8T, and (E) C8P. F8PEG and C8TEG/C8PEG carbon atoms are in grey and cyan, respectively, while oxygen atoms are in red. Water and inorganic ions are not shown for the sake of clarity.*

The snapshots showed the fluid nature of the outer shell of the monolayers when the PEGylated portion of the thiolates is longer (as in F8P or C8P, see Figure 19 **A-C** and Figure 19**E**). When the PEGylated portion is shorter (as in C8T), there is a local chain compaction that affects either the external and the internal part of the shell (Figure 19 **D**).

With respect to the inner part of the monolayer, while longer PEGylated fragments lead to disordered external surfaces, a degree of ordering is observed in the inner part of the monolayer, with evidence of bundling involving both the F- and H- portion of the ligands (see Figure 17 and Figure 20).

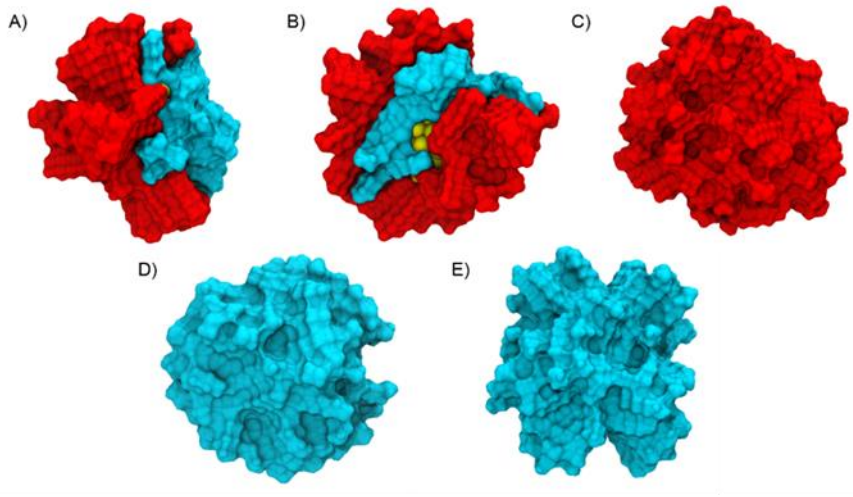

Figure 20: ***Examples of AA-MD simulation snapshots illustrating ligand organization on the gold surface.*** *Only the hydrophobic portion of each thiolate (i.e., C8 part of C8TEG or C8PEG, and F8 part of F8PEG, see* ***Scheme 1****) is depicted as red and cyan molecular surface, respectively, to emphasize ligand bundling and arrangement in the inner part of the monolayer. (A) M1-C8T/F8P, (B) M1-C8T/F8P, (C) F8P, (D) C8T, and (E) C8P.*

Due to the small core size (~ 2 nm) the degree of compaction is less than the one observed for larger core diameters, coated with ligands of similar length. This happens because the reduced core dimension, with respect to the ligand length, gave a high conformational freedom to the chains, which reduced inter-ligand interactions and prevented their compaction.

In the mixed ligand cases the presence of immiscible ligands organized in nanoscale domains made the hydrophobic distribution less "regular" with respect to homoligand systems, resulting in a morphology dependent behavior. This visual inspection was also supported by comparison of the radial distribution functions for F8PEG, C8TEG, and C8PEG ligands in each NP system (Figure 21).

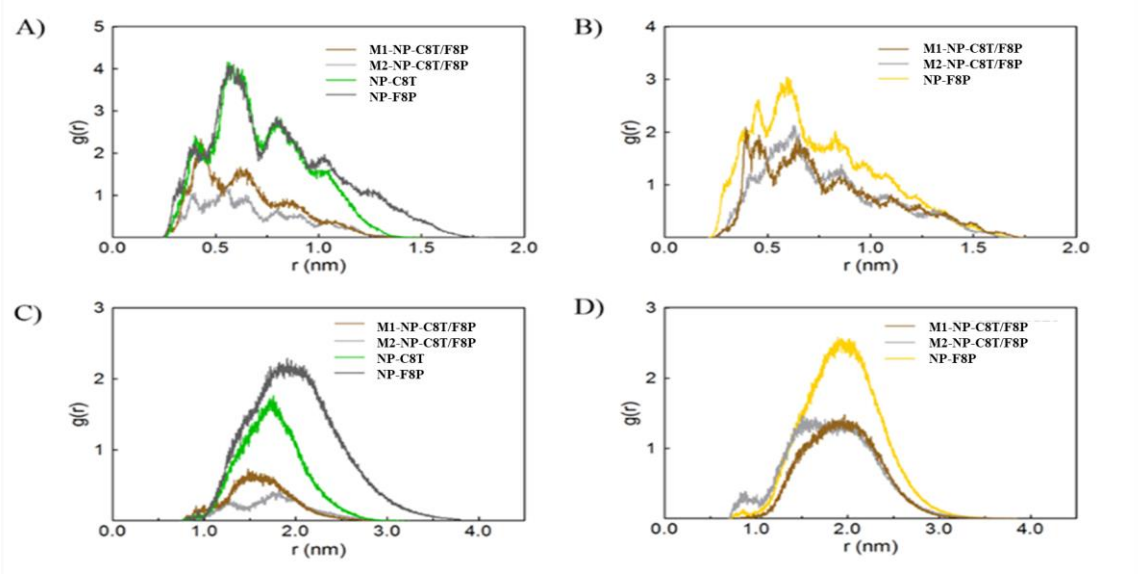

Figure 21: ***Radial distribution functions g(r) of all NPs in solution calculated from AA-MD trajectories****. Distances are measured relative to the surface of the gold core. Panels (A) and (B) refer to the alkyl portion of the hydrogenated (C8TEG and C8PEG) and fluorinated (F8PEG) ligands, respectively, whilst panels (C) and (D) report the distribution of the TEG/PEGylated moieties, respectively.*

We then characterized the five different types of monolayer in terms of *global* structural properties:

- NP radius of gyration (R_g),
- molecular asphericity (δ),
- solvent accessible surface area (*SASA*),

which, when considered together, provided information regarding the water-NP interface.

Table 4 lists these values for each system and Figure 22illustrates *SASA* contributions.

SAM-AuNP	$\boldsymbol{R_g}$ (nm)	$\boldsymbol{\delta}$	***SASA*** (nm^2)
M1-C8T/F8P	1.98 (0.01)	0.35 (0.13)	111.5 (7.0)
M2-C8T/F8P	2.04 (0.02)	0.32 (0.14)	116.8 (6.3)
F8P	2.40 (0.01)	0.31 (0.08)	122.2 (10.1)
C8T	1.81 (0.02)	0.24 (0.07)	146.7 (6.6)
C8P	2.24 (0.02)	0.34 (0.05)	125.7 (15.7)

Table 4: ***Comparison of radius of gyration (R_g), asphericity (δ) and solvent accessible surface area (SASA)*** *for the SAM-^{Au}NPs considered in this work. Simulation uncertainties are given in parenthesis.*

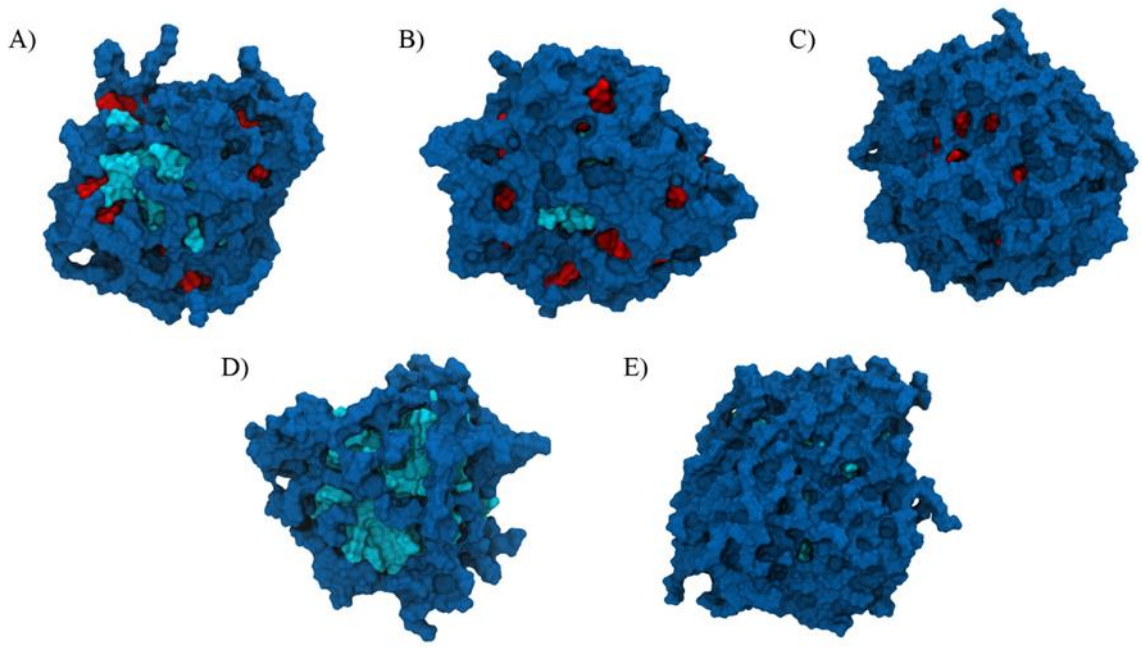

Figure 22: ***SASA contributions in SAM-AuNPs****, stemming from PEG/TEGylated (blue), fluorinated (red), and hydrogentaed (cyan) moieties of M1-C8T/F8P (A), M2-C8T/F8P (B), F8P (C), C8T (D), C8P (E).*

Analyzing the global properties, all systems exhibited similar shape and SASA, except for the C8T system. The AuNPs coated with mixed ligand monolayers showed the same values indicating that it is not possible to distinguish the nanoscale morphology, at this scale level, when these NPs are in solution. Similarities in measurable structural characteristics of NPs with differently organized monolayers have been observed also for other types of gold core NPs covered with mixtures of immiscible ligands in aqueous solutions. (200-204; 65; 86)

3.2.3 Anionic H-/F- mixed monolayer nanoparticle

The exploration of the ligand structure highlighted that the difference in length between hydrogenated and fluorinated ligands is a critical parameter to be taken into account for obtaining NPs with acceptable solubility properties. The fluorinated thiol must be short enough, compared to the hydrogenated ligand, to form fluorinated domains sufficiently small to be masked from the solvent. At the same time, this parameter has a great impact on the overall monolayer organization. (208) In what follows, we explore this aspect from the

computational point of view, studying a series of H-/F-mixed monolayer AuNPs with different surface charges by using a mixture of ligands as reported in

Figure 23. The sodium salts of the 11-mercaptoundecansulfonic acid (HMUS), 12-mercaptododecanesulfonic acid (HMDDS) and 16-mercaptohxadecanesuflonic acid (HMHDS) were used to provide NPs with permanent negative charges. These thiols were used in combination with 1H,1H,2H,2H-perfluoro-1-octanethiol (HF6) as the fluorinated components.

For all systems we considered different ligand (H/F) ratios (1:1 and 2:1). The influence of the size of the core on the monolayer morphology was also assessed by increasing the diameter from 1.6 nm to 3 till 4.2 nm. This study allowed to identify how the shell morphology changes due to the different ligand ratio, different relative length between ligands and core dimensions in the presence of anionic a fluorinate ligands.

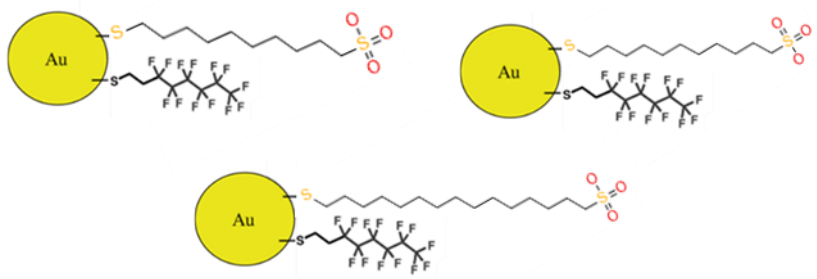

Figure 23: NP-MUS/F6 (left), NP-MDDS/F6 (right) and NP-MHDS/F6 (bottom)

3.2.4 Computational details

3.2.4.1 Dissipative Particle Dynamics

The spontaneous assembling process of the ligands on the gold surface was investigated by means of Dissipative Particle Dynamics (DPD). The set of nanoparticles considered for this study was simulated following the procedure described in Section 3.1.1. Accordingly, we will report here only the parameters pertaining to these specific systems. The initial structure of the NP core was constructed by arranging DPD beads (Au) on a *fcc* lattice into the desired icosahedral shape and diameter. Each ligand was represented by a flexible chain model of

beads connected by harmonic springs of composition reported in Table 5. Solvent (water) and ions were modelled as a single bead.

Ligand type	*Model*
HMUS	$S(C)_5Q$
HMDDS	$S(C)_6Q$
HMHDS	$S(C)_8Q$
F6	$SC(F)_3$

Table 5: Coarse-grained model of each ligand.

As described above, DPD pair-pair interaction parameters and ligand topology may be derived using a multiscale simulation protocol, combining atomistic and coarse-grained simulation. (191-195)

Accordingly, we derived the following values for a_{ij}: $a_{C\text{-}C}$ = 51.6, $a_{C\text{-}E}$ = 60.5, $a_{C\text{-}F}$ = 66.0, $a_{C\text{-}Q}$ = 68.9, $a_{C\text{-}S}$ = 72.0, $a_{C\text{-}W}$ = 63.8, $a_{F\text{-}F}$ = 58.8, $a_{F\text{-}E}$ = 64.3, $a_{F\text{-}Q}$ = 55.1, $a_{F\text{-}S}$ = 80.0, $a_{F\text{-}W}$ = 62.3, $a_{Q\text{-}Q}$ = 72.6, $a_{Q\text{-}E}$ = 71.2, $a_{Q\text{-}S}$ = 80.0, $a_{Q\text{-}W}$ = 26.0, $a_{S\text{-}S}$ = 51.6, $a_{S\text{-}W}$ = 80.0, $a_{S\text{-}E}$ = 72.0, $a_{W\text{-}W}$ = 51.6, $a_{W\text{-}E}$ = 61.0, $a_{E\text{-}E}$ = 51.6 k_BT.

A 24rc X 24rc X 24rc simulation box was adopted, placing the monolayer protected NP in the middle of the periodic cell. Optimized adimensional values for bond and angle parameters were employed for both alkane and perfluorocarbon thiols: k_b(C-S) = 10, r_0(C-S) = 0.50, k_θ(C-C-S) = 0, θ_0 (C-C-S) = 180, k_b(C-C) = 10, r_0(C-C) = 0.60, k_θ(C-C-C) = 10, θ_0 (C-C-C) = 110, k_b(C-Q) = 10, r_0(C-Q) = 0.45, k_θ(C-C-Q) = 10, θ_0 (C-C-Q) = 110.

Each initial configuration was first equilibrated for $1x10^4$ steps and a time step of $\Delta t=0.01\tau$. Then, additional $8x10^6$ time steps ($\Delta t=0.02$) were performed increasing the interaction parameters till their actual value.

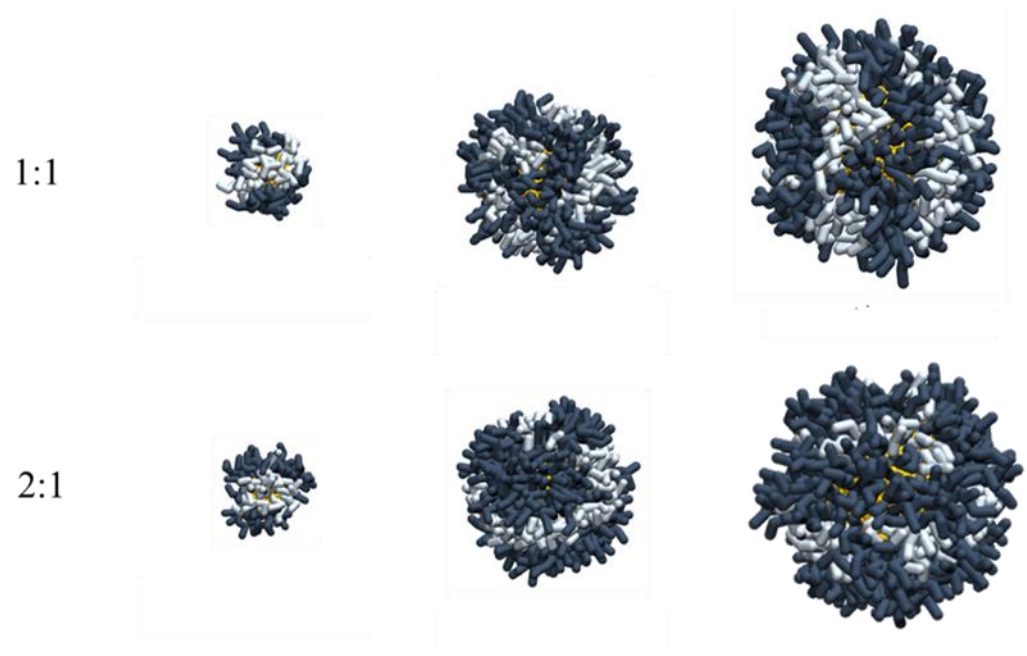

Figure 24: NP-MUS/F6 AuNPs. MUS ligand (deep blue), F6 ligand (light grey), AuNP (yellow). Water and inorganic ions are not shown for the sake of clarity.

Considering the NP-MUS/F6 set (Figure 24), when the core diameter is small (2 nm), the two ligands phase-separated resulting in the presence of a F-belt that involves all the NP surface for 1:1 ratio and only a part of the core for 2:1 proportions. Increasing the diameter to 3 nm, the monolayer organization evolved. When the ligands are present in an equal proportion, calculations revealed the presence of stripe-like domains, while a belt and patches constituted by MUS chains were formed. Increasing the diameter to 4.2 nm lead to an organization more ordered and to the presence of regular stripe domains for 1:1 MUS/F6 ligand ratio and stripe-like domains for 2:1 MUS/F. Typically, domain dimensions was in a range of 0.9 and 1 nm.

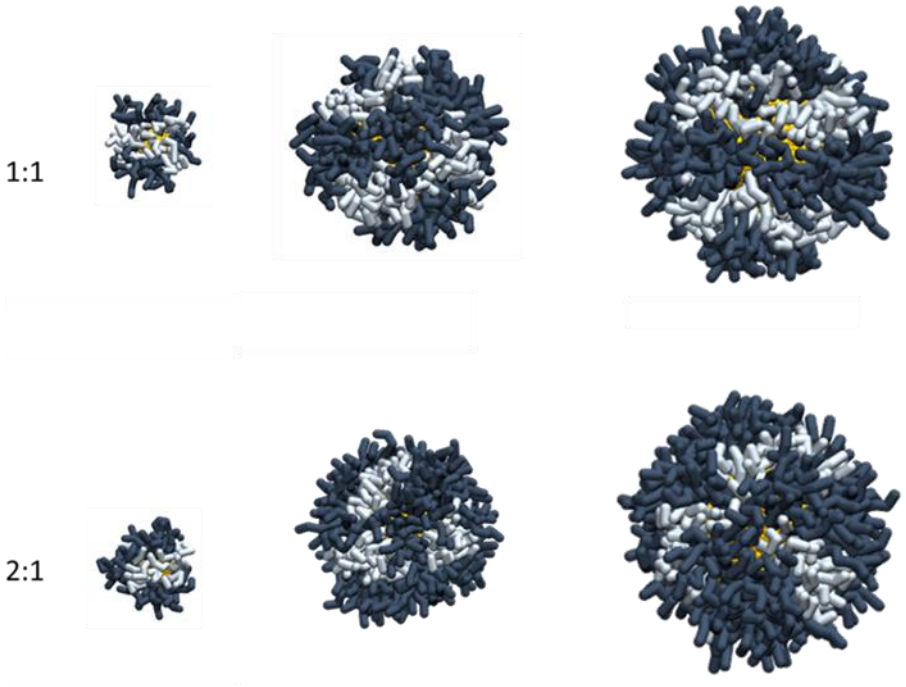

Figure 25: NP-MDDS/F6 AuNPs. MDDS ligand (deep blue), F6 ligand (light grey), AuNP (yellow). Water and inorganic ions are not shown for the sake of clarity.

Analyzing the NP-MDDS/F6 structures, (Figure 1), when the diameter is small (2nm), the two ligands phase-separated resulting in the presence of a F-belt that in both cases involved only partially the surface of the NP. Increasing the diameter to 3 nm, the monolayer organization evolved and lead to the presence of stripes for the 1:1 ratio, while for the second ratio considered, elongated patches of F- thiolates were present. Increasing the diameter to 4.2 nm the 3D organizations persisted. Typically, domain dimension found in a range of 0.78 and 1 nm.

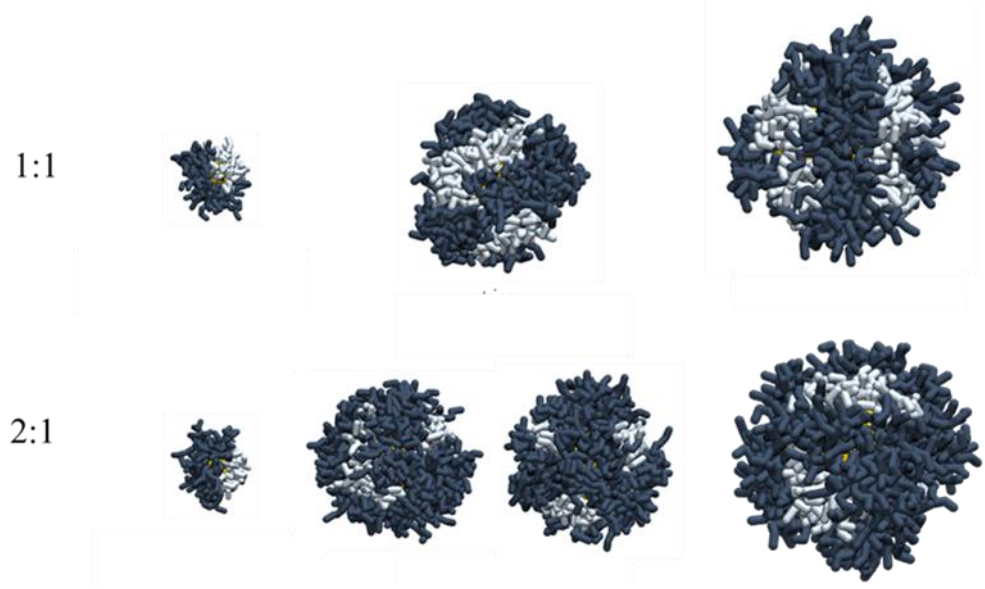

Figure 26: NP-MHDS/F6 AuNPs. MHDS ligand (deep blue), F6 ligand (light grey), AuNP (yellow). Water and inorganic ions are not shown for the sake of clarity

Moreover, in the case of longest chains (NP-MHDS/F6) (Figure 26) when the diameter is 1.6 nm, both cases present a Janus morphology. Increasing the diameter from 3 till 4.2 nm, it could be appreciated how in the 1:1 case the organization presented stripe domains, while in the other case the organization evolved in elongated patches (average domain dimensions around 1 nm).

Increasing the diameter, for all systems and for each ratio considered, lead to a different morphology. For really small diameter was present an F- belt was present, or a defined phase-separated morphology as expected, while for smaller curvature radius an overall striped or elongated patched morphology was found. The well-defined nanostructured morphology can be appreciated better as soon as the charged ligand was longer. This can be explained by a bigger free volume available for the MHDS chains rather than the MDDS or the MUS thiolates that promote the formation of interfaces between immiscible ligands.

Due to the well-established ability of fluorinated thiolates to self-sort on the surface of AuNPs we are confident that these systems will significantly widen the span of NP systems with anisotropic monolayers to probe the interactions of nanosized matter with the biological environment. (208)

3.2.5 Zwitterionic Nanoparticles

In recent years, to enhance the selective accumulation of NPs at tumor tissues, some types of pH-responsive zwitterionic polymers have been designed, which possess high biocompatibility and pH sensitivity. These polymers are nearly electroneutral at normal tissue pH and become positively charged at tumor tissue pH, which can dramatically enhance the electrostatic interaction between polymer-coated NPs and negatively charged membranes, thus the cellular uptake efficiency of NPs could be greatly improved. (209)

It is urgent and of great significance to deeply explore the characteristics of the pH-responsive zwitterionic polymer-coated NPs to promote their use in biomedical applications. As indicated by some recent reviews, keeping the balance between the delivery efficiency and toxicity of NPs should be carefully considered. (210)

For these reasons, a new type of water soluble nanoparticles, named zwitterionic nanoparticles (ZW AuNPs), were investigated by computational techniques. In these systems, the alkylic chains were replaced by two zwitterionic ligands, each of them considered again in mixture with perfluoresane thiols (

Figure 27).

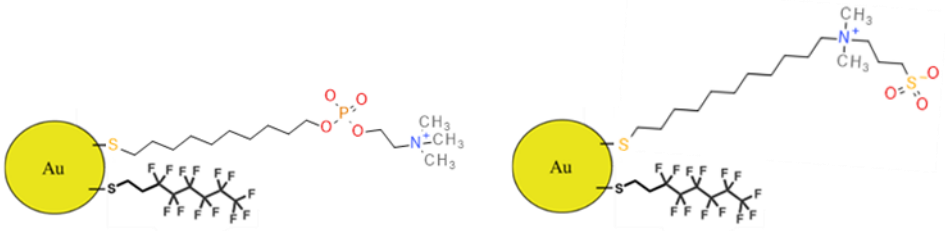

Figure 27: ZW1/F6 (left) and ZW2/F6 (right) AuNPs

3.2.6 Computational details

3.2.6.1 Dissipative Particle Dynamics

The spontaneous assembling process of the ligands on the gold surface was investigated by means of Dissipative Particle Dynamics (DPD). The set of nanoparticles considered for this study was simulated following the procedure described in Section 3.1.1. Accordingly, we will report here only the parameters pertaining to these specific systems. The initial structure of the NP core was constructed by arranging DPD beads (Au) on a *fcc* lattice into the desired

icosahedral shape and diameter. Each ligand was represented by a flexible chain model of beads connected by harmonic springs of composition reported in Table 6. Solvent (water) and ions were modelled as a single bead.

Ligand type ZW1	*Model*
ZW1	$S(C)_5PEb$
ZW2	$S(C)_5bEQ$

Table 6: Coarse-grained model of each ligand considered in the study

As described above, DPD pair-pair interaction parameters and ligand topology were derived using a multiscale simulation protocol, combining atomistic and coarse-grained simulation. (191-195)

Accordingly, we derived the following values for a_{ij}: $a_{CL\text{-}CL}$ = 51.6, $a_{CL\text{-}NA}$ = 51.6, $a_{CL\text{-}P}$ = 51.6, $a_{CL\text{-}Au}$ = 51.6, $a_{CL\text{-}b}$ = 51.6, $a_{CL\text{-}C}$ = 57.6, $a_{CL\text{-}E}$ = 57.6, $a_{CL\text{-}F}$ = 58.3, $a_{CL\text{-}Q}$ = 78.3, $a_{CL\text{-}S}$ = -10.0, $a_{CL\text{-}W}$ = 75.7, $a_{NA\text{-}NA}$ = 51.6, $a_{NA\text{-}P}$ = 51.6, $a_{NA\text{-}Au}$ = 51.6, $a_{NA\text{-}b}$ = 51.6, $a_{NA\text{-}C}$ = 57.6, $a_{NA\text{-}E}$ = 57.6, $a_{NA\text{-}F}$ = 58.3, $a_{NA\text{-}Q}$ = 78.3, $a_{NA\text{-}S}$ = -10.0, $a_{NA\text{-}W}$ = 75.7, $a_{P\text{-}P}$ = 51.6, $a_{P\text{-}Au}$ = 51.6, $a_{P\text{-}b}$ = 51.6, $a_{P\text{-}C}$ = 57.6, $a_{P\text{-}E}$ = 57.6, $a_{P\text{-}F}$ = 58.3, $a_{P\text{-}Q}$ = 78.3, $a_{P\text{-}S}$ = -10.0, $a_{P\text{-}W}$ = 75.7, $a_{Au\text{-}Au}$ = 51.6, $a_{Au\text{-}b}$ = 51.6, $a_{Au\text{-}C}$ = 57.6, $a_{Au\text{-}E}$ = 57.6, $a_{Au\text{-}F}$ = 58.3, $a_{Au\text{-}Q}$ = 78.3, $a_{Au\text{-}S}$ = -10.0, $a_{Au\text{-}W}$ = 75.7, $a_{b\text{-}b}$ = 51.6, $a_{b\text{-}C}$ = 51.6, $a_{b\text{-}E}$ = 60.5, $a_{b\text{-}F}$ = 66.0, $a_{b\text{-}Q}$ = 68.9, $a_{b\text{-}S}$ = 72.0, $a_{b\text{-}W}$ = 63.8, $a_{C\text{-}C}$ = 51.6, $a_{C\text{-}E}$ = 60.5, $a_{C\text{-}F}$ = 66.0, $a_{C\text{-}Q}$ = 68.9, $a_{C\text{-}S}$ = 72.0, $a_{C\text{-}W}$ = 63.8, $a_{F\text{-}F}$ = 58.8, $a_{F\text{-}E}$ = 64.3, $a_{F\text{-}Q}$ = 55.1, $a_{F\text{-}S}$ = 80.0, $a_{F\text{-}W}$ = 62.3, $a_{Q\text{-}Q}$ = 72.6, $a_{Q\text{-}E}$ = 71.2, $a_{Q\text{-}S}$ = 80.0, $a_{Q\text{-}W}$ = 26.0, $a_{S\text{-}S}$ = 51.6, $a_{S\text{-}W}$ = 80.0, $a_{S\text{-}E}$ = 72.0, $a_{W\text{-}W}$ = 51.6, $a_{W\text{-}E}$ = 61.0, $a_{E\text{-}E}$ = 51.6 r_C/k_BT.

A 25rc X 25rc X 5rc simulation box was adopted, placing the monolayer protected NP in the middle of the periodic cell. Optimized adimensional values for bond and angle parameters were employed for both alkane and perfluorocarbon thiols: k_b(C-S) = 10, r_0(C-S) = 0.50, k_θ(C-C-S) = 0, θ_0 (C-C-S) = 180, k_b(C-C) = 10, r_0 (C-C) = 0.60, k_b(C-C-C) = 30, θ_0 (C-C-C) = 130, k_b(C-b) = 10, r_0(C-b) = 0.80, k_θ(C-C-b) = 30, θ_0 (C-C-b) = 130, k_b(E-b) = 10, r_0(E-b) = 0.50, k_θ(C-E-b) = 30, θ_0 (C-E-b) = 130, k_b(E-Q) = 10, r_0(E-Q) = 0.80, k_θ(E-b-Q) = 30, θ_0 (E-b-Q) = 130.

Each initial configuration was first equilibrated for $1x10^4$ steps and a time step of $\Delta t=0.01\tau$. Then, additional $8x10^6$ time steps ($\Delta t=0.02$) were performed increasing the interaction parameters till their actual value.

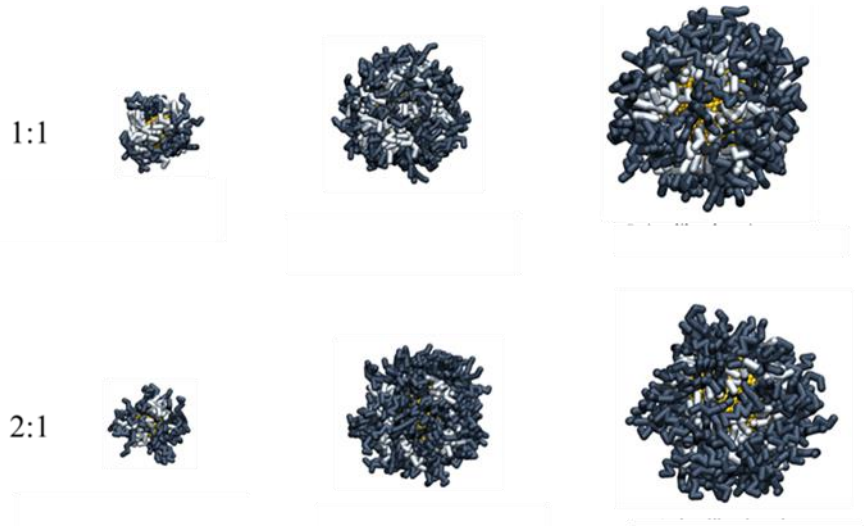

Figure 28: ZW1/F6 AuNPs. ZW1 ligand (deep blue), F6 ligand (light grey). Solvent and ions were omitted for clarity.

The overall results (Figure 28, Figure 29) show that, regardless the chemical different structure of ZW1 and ZW2 ligand, when the core dimension is about 2 nm, the shell presents a phase-separated organization for 1:1 ligand ratio and a perfluorinated belt for 2:1 ligand ratio; while, increasing the core dimensions up to 3 nm, the structure evolved in striped/stripe-like domains which persisted also when the diameter is 4 nm in size.

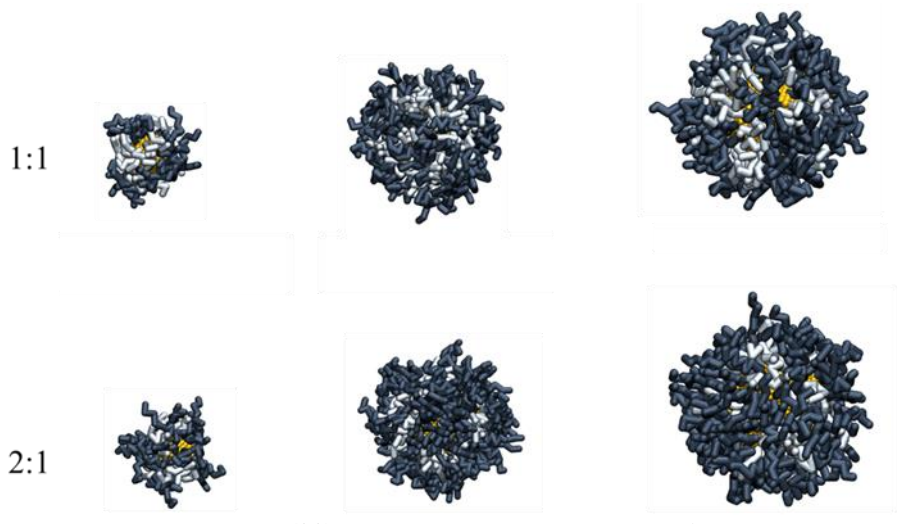

Figure 29: ZW2/F6 AuNPs. ZW1 ligand (deep blue), F6 ligand (light grey). Solvent and ions were omitted for clarity

An overall comparison between the employment of different charged ligands mixed with perfluorinated thiols, in order to obtain water soluble NPs to be used as an alternative to PEGylated systems, can be gained discussing the results obtained from the computational evaluation of the anionic and the zwitterionic nanoparticles. Regarding the anionic NPs we consider for the comparison the MHDS thiols which have a comparable length with respect to the zwitterionic ligands.

Comparing these systems at the smallest diameter while for the anionic system there is a complete phase-separation, for the zwitterionic systems an F-belt is formed as a consequence of the electrostatic repulsion which prevents the thiolates to stay closely packed as in a Janus morphology. The same effect is present also in the other morphology, when the diameter increased, where the presence of positive and negative charges on the same chain (ZW1 and ZW2) seems to lead to an increased number of interfaces between domains favoring the striped-like SAM organization.

3.2.7 Influence of synthesis condition on the morphology of the self-assembled monolayer

The synthesis of gold nanoparticles protected by mixtures of mercaptoalkylsulfonate and perfluorinated thiols with a dispersion of the core diameter lower than 10% may be fulfilled using a modification of a procedure previously reported by Stucky (211). Briefly, a solution of the two thiols in deoxygenated ethanol is added to an ethanol solution of $HAuCl_4$ and the reaction is let to stir at room temperature. Then, a solution of $NaBH_4$ in ethanol is added in 15 minutes and the color change to violet. The mixture is stirred for 3 h, and then the dispersion is centrifuged obtaining a black precipitate. The solid is then washed with a hot solution of ethanol and purified by size exclusion chromatography on Sephadex G-75 in water. NMR experiments on decomposed NPs showed that a small quantity of triphenylphosphine (TFP), from the gold precursor used for the synthesis, is incorporated into the monolayer and is not released after the purification. Thus, we were wondering if and how this could affect the way in which ligands self-organize on the gold surface.

We considered gold nanoparticles of 4 nm in diameter and protected by a mixture of a 2:1 ratio of MUS and F6 ligands (Figure 30) suspended in a 1:1 ethanol:toluene solution at 86 °C (synthesis conditions) and in a solution of water and 10% ethanol at 25°C (working conditions). We created the computational models of each system without triphenylphosphine and in presence of 8 (2.5%) and 16 (5%) molecules of TFP.

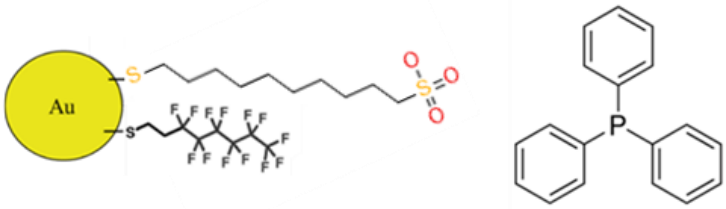

Figure 30: MUS/F6 AuNP (left) and TFP (right)

3.2.8 Computational details

3.2.8.1 Dissipative Particle Dynamics

The spontaneous assembling process of the ligands on the gold surface was investigated by means of Dissipative Particle Dynamics (DPD). The set of nanoparticles considered for this study was simulated following the procedure described in Section 3.1.1. Accordingly, we will report here only the parameters pertaining to these specific systems. The initial structure of the NP core was constructed by arranging DPD beads (Au) on a *fcc* lattice into the desired icosahedral shape and diameter. Each ligand was represented by a flexible chain model of beads connected by harmonic springs of composition reported in Table 7. To reproduce the peculiar structure and hinderance of the triphenylphosphine molecule we decided to adopt the CG model reported in Table 7. Solvents were modelled as a single bead.

Ligand type	*Model*
HMUS	$S(C)_5Q$
F6	$SC(F)_3$
TFP	$P(B)_9$

Table 7: Coarse-grained model of each Anionic NPs ligand and triphenylphosphine

As described above, DPD pair-pair interaction parameters and ligand topology were derived using a multiscale simulation protocol, combining atomistic and coarse-grained simulation. (191-195)

Therefore, we employed the following values for a_{ij}: $a_{C\text{-}C} = 51.6$, $a_{C\text{-}E} = 60.5$, $a_{C\text{-}F} = 66.0$, $a_{C\text{-}Q} = 68.9$, $a_{C\text{-}S} = 72.0$, $a_{C\text{-}W} = 63.8$, $a_{F\text{-}F} = 58.8$, $a_{F\text{-}E} = 64.3$, $a_{F\text{-}Q} = 55.1$, $a_{F\text{-}S} = 80.0$, $a_{F\text{-}W} = 62.3$, $a_{Q\text{-}Q} = 72.6$, $a_{Q\text{-}E} = 71.2$, $a_{Q\text{-}S} = 80.0$, $a_{Q\text{-}W} = 26.0$, $a_{S\text{-}S} = 51.6$, $a_{S\text{-}W} = 80.0$, $a_{S\text{-}E} = 72.0$,

$a_{W\text{-}W}$ = 51.6, $a_{W\text{-}E}$ = 61.0, $a_{E\text{-}E}$ = 51.6, $a_{P\text{-}P}$ = 51.6, $a_{P\text{-}b}$ = 51.6, $a_{P\text{-}C}$ = 57.6, $a_{P\text{-}E}$ = 57.6, $a_{P\text{-}F}$ = 58.3, $a_{P\text{-}Q}$ = 78.3, $a_{P\text{-}S}$ = -10.0, $a_{P\text{-}W}$ = 75.7, $a_{B\text{-}P}$ = 51.6, $a_{B\text{-}b}$ = 51.6, $a_{B\text{-}C}$ = 57.6, $a_{B\text{-}E}$ = 57.6, $a_{B\text{-}F}$ = 58.3, $a_{B\text{-}Q}$ = 78.3, $a_{B\text{-}S}$ = -10.0, $a_{B\text{-}W}$ = 75.7 r_C/k_BT.

A $28r_C$ X 28 r_C X 28 r_C simulation box was adopted, placing the monolayer protected NP in the middle of the periodic cell. Optimized adimensional values for bond and angle parameters were employed for both alkane and perfluorocarbon thiols: k_b(C-S) = 10, r_0(C-S) = 0.50, k_θ(C-C-S) = 0, θ_0 (C-C-S) = 180, k_b(C-C) = 10, r_0(C-C) = 0.60, k_θ(C-C-C) = 10, θ_0 (C-C-C) = 110, k_b(C-Q) = 10, r_0(C-Q) = 0.45, k_θ(C-C-Q) = 10, θ_0 (C-C-Q) = 110, k_b(B-P) = 10, r_0(B-P) = 0.50, k_θ(B-B-B) = 10, θ_0 (B-B-B) = 60, k_b(B-B) = 10, r_0(B-B) = 0.60, k_θ(B-B-P) = 10, θ_0 (B-B-P) = 150, k_θ(B-P-B) = 10, θ_0 (B-P-B) = 109.

Each initial configuration was first equilibrated for 10000 steps and a time step of $\Delta t = 0.02\tau$. Then, additional 2000000 steps with the same time step (Δt = 0.02) were performed increasing the interaction parameters till their actual value.

3.2.8.2 Results

At the beginning, we simulated the system in absence of TFP at both 86 and 25 °C and using the two different solvents to be able to evaluate the effect of each single parameter more easily. Decreasing the temperature from 86°C in an ethanol/toluene solution to 25°C same solution (1 → 3), we can observe a stripe-like nanostructure of the SAM which became more defined decreasing the temperature. This effect was somewhat expected due to the lower kinetic energy provided to the ligands and the higher chemical repulsion between the chains and from this evidence it was possible to assess that temperature increased domains formation. For this reason, changing only the solvent (3 → 4), from ethanol/toluene to ethanol/water, or changing both solvent and temperature (1 → 2), the SAM morphology evolved from stripe-like to elongated patches. From these evidences, it was possible to assess that there are two effects playing a role: the one of the temperature, which increases domains definition, and the one of the solvent that modifies domains morphology (gFigure 31).

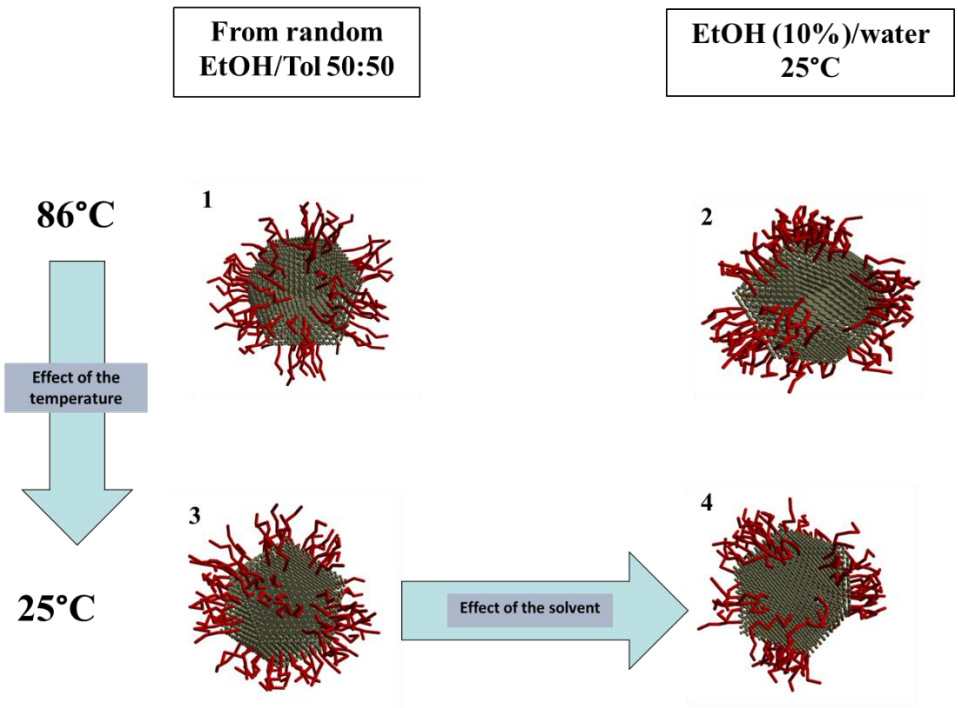

gFigure 31: No triphenylphosphine systems

To understand if and how the presence and distribution of triphenylphosphine molecules on NP surface might influence the monolayer nanostructure, we placed 8 and 16 TFP molecules displaced both randomly and in two ordered domains on the gold surface.

At the lower TFP percentage, either for the random and ordered case, the SAM morphology changed from a stripe-like, in synthesis conditions, to elongated patches involving the triphenylphosphine molecules (Figure 32).

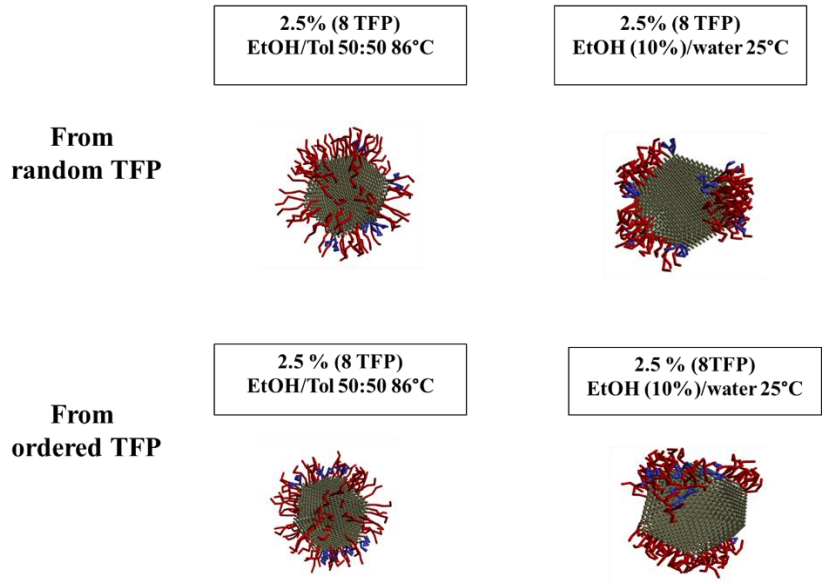

Figure 32: 8 TFP systems

Increasing the concentration, under synthesis conditions, the morphology was found to be stripe-like for the ordered system and random in the random case. In both cases the morphology changed, under working condition, showing patches, smaller for the random system than in the ordered one, either involving the triphenylphosphine molecules (Figure 33).

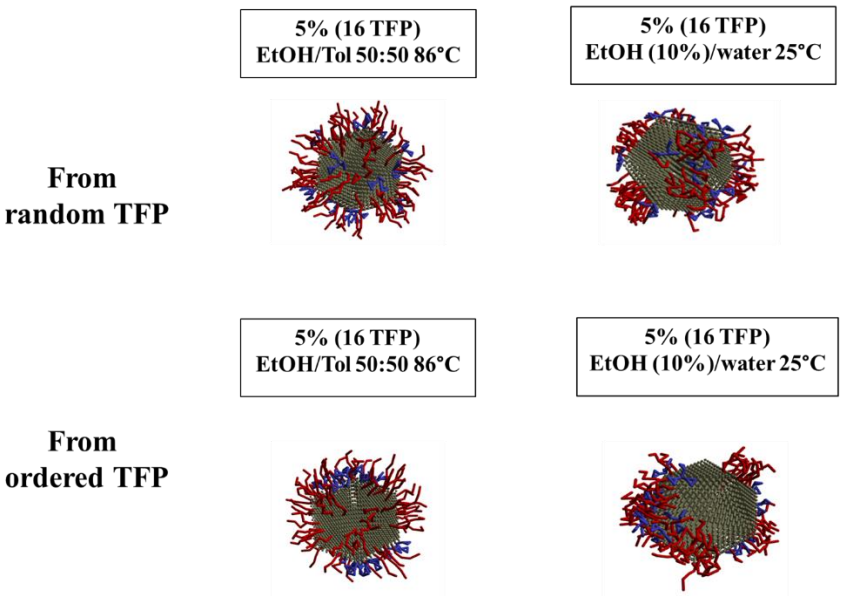

Figure 33: 16 TFP systems

The presence of TFP in the systems showed how triphenylphosphine tends to interact within the F6 domains increasing their definition and compaction even at very small concentrations.

Chapter 4. *Interaction of coated gold nanoparticles with membranes*

Cell membrane is evidently one of the principal physical barrier to cellular internalization of nanoparticles (NPs). Membrane models are currently employed to understand the influence of the physicochemical properties of NPs on their interactions with bilayers under controlled experimental conditions. Thanks to the availability of ever-increasing computing power, several theoretical studies have recently been performed to probe molecular aspects of NP–membrane interactions. The most widely applied computational techniques are classical methods such as MD, which enable exploration of structural evolution and structure–activity relationships in biological systems with atomic-level resolution. (212) However, most biological phenomena occur on time and length scales not yet accessible to MD calculations, and more simplistic techniques such as CG (213, 214) or (almost) purely thermodynamic methods (215) become necessary. (92)

We selected binary mixtures of hydrogenated or fluorinated thiols (C8TEG and F8PEG, see Scheme 1, chapter 3) to prepare water-soluble SAM-protected AuNPs. (216) These ligands were amphiphilic, with the thiol-substitute segment (C8 and F8 in Scheme 1) being the immiscible part, while the external segments were either TEG or PEG, making the surface water-soluble. (216-219)

All the *in-silico* results were complemented by Surface Plasmon Resonance (SPR) and in vitro experiments performed by the group of prof. Sabrina Pacor and prof. Alessandro Tossi (Department of Life Sciences, University of Trieste), of which a synthesis is reported in the App).

4.1 Computational details

4.1.1 Coarse-grained simulations

Coarse-grain molecular dynamics simulation (CG-MD) is a powerful tool for studying NP–biomembrane interactions allowing to model larger systems and longer times than traditional all-atom (AA) simulations.(220-222) As a typical CG force field, the Martini force field can simulate biological systems, including lipid membranes, proteins, and genes and in recent

times has been employed widely to investigate nanomaterial behavior in bio-environments.(223)

To describe our ligands within the MARTINI framework, we resolved to a blend of 4-to-1 and 3-to-1 mapping schemes, as represented in Figure 34.

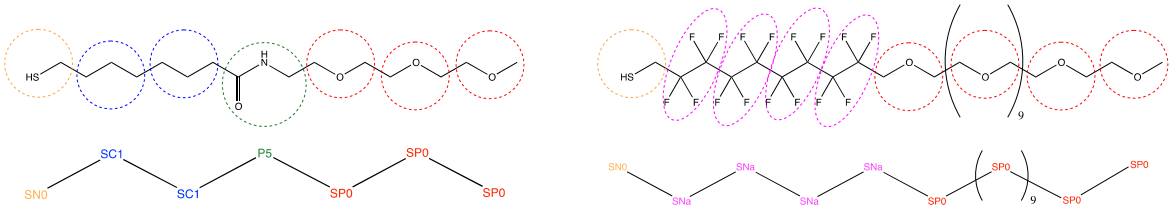

Figure 34: Model of C8TEG (left) and F8PEG (right) ligands in the framework of the MARTINI forcefield

To model the PEG/TEG units, the SP0 bead as introduced by the group of Rossi was chosen, (224) while the SC4 representation was given to the gold atoms. The remaining bead types were assigned based on the relative water/octanol partition coefficients. Bonded interactions were described with harmonic (bonds), cosine-harmonics (non-PEG/TEG angles), restricted bending potential (PEG/TEG angles) and Ryckaert−Bellemans (PEG/TEG dihedrals) functions. (225) As standard procedure for modelling new molecules, we reproduced the distributions of bonds and angles from AA simulations, tuning accordingly the parameters for the bonded interactions (Figure 35).

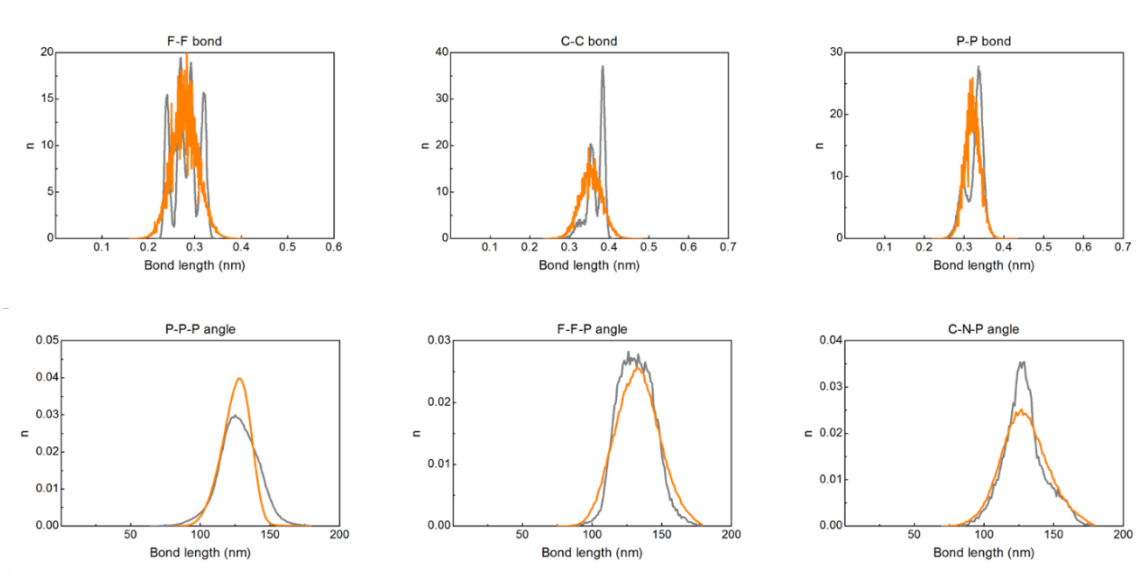

Figure 35: Exemplificative distribution of bonds and angles obtained for M1-C8T/F8P. The data from AA simulation are reported in grey, while the corresponding data from MARTINI calculation are in orange.

.

The tuning of the bonded interactions for the alkyl portion of the two ligands was made in a nanoparticle-specific way, to better reflect the effects of the interactions between ligands in the self-assembled monolayer.

The two membranes considered in this thesis were described as a single-component bilayer (pure 1,2-dioleoyl-sn-glycero-3-phosphocholine (DOPC)) or a three-component bilayer using the MARTINI model for DOPC, sphingomyelin (SPHI) and cholesterol (CHOL). All membrane models were built using the insane.py (226) script, and the same tool was used to solvate the model and place the NPs above the membranes. The ternary mixture of DOPC, SPHI, and CHOL was selected as a representative system with an average CHOL level resembling biological membrane (~25% mol). We built the molecular DOPC: SPHI: CHOL = 1: 2: 1 structure such as to resemble a zoomed portion of the mixture as it appeared in AFM images but in 2D periodic conditions. (227) DOPC- and SPHI-rich domains were constructed to have a content of ~15 % and ~37 % CHOL, respectively. (228)

NPs were placed in water phase approx. 8-9 nm away from the bilayer. Different initial orientations (relative to the C8/F8 interface) were explored for M1- and M2-C8T/F8P. All MARTINI systems were minimized by 50000 steps of minimization, followed by 100 ns of equilibration. The v-rescale algorithm was used for temperature control (coupling time of 1 ps, temperature 300 K), and the pressure was kept at 1 atm by a Berendsen algorithm (coupling time of 5 ps, semi-isotropic in simulations with membranes). We then switched to a Parrinello-Rahman algorithm for pressure control (coupling time of 12 ps) and performed the data collection. Electrostatic and Van der Waals interactions were treated as the standard for MARTINI simulations performed with GROMACS on GPU. (230)

4.1.2 Umbrella sampling calculations

Umbrella sampling (231, 232) calculations were employed to retrieve the potential of mean force (PMF) along a reaction coordinate. We chose as reaction coordinate the distance, in the *z* direction, from the center of mass (COM) of the NP and the COM of the membrane. The latter was not computed over all lipids but were considered only lipids within a cylinder of radius 2.5 nm centered at the solute and aligned along the *z* axis (GROMACS option "pull-coord1-geometry = cylinder"). A steered MD simulation was performed to obtain the

starting configurations along the reaction coordinate, with a pulling velocity of 0.1 m/s and a force constant of 5000 kJ mol^{-1} nm^{-2}. From the trajectory, we extracted main windows separated by 1 nm from each other along the reaction coordinate, and these were equilibrated for 400 ns with their reaction coordinate kept fixed with a force of 2500 kJ mol^{-1} nm^{-1}. From each one of these equilibrated windows, 4 windows were spawned (at -0.4, -0.2, +0.2, +0.4 nm from the original reaction coordinate of the main window). All windows obtained were equilibrated for another 50 ns with their reaction coordinate kept fixed, and then data collection was performed for 100 ns with a force constant of 1250 kJ mol^{-1} nm^{-1}.

4.2 Results

To understand how self-assembled monolayer protected NPs interact with such a complex system we firstly developed a computational model to evaluate the interaction of NPs with a nanostructured monolayer (Stripe and Janus) and a simple model membrane made of 1,2-dioleoyl-sn-glycero-3-phosphocholine (DOPC) lipid; currently employed both in experimental and simulation studies involving model membranes and NPs.

Previous analysis of the fluid nature of the outer shell, in terms of global structural properties (radius of gyration, molecular asphericity and solvent accessible surface area) of the monolayers indicated that is not possible to distinguish them in the presence of solvent. However, we were interested in understanding if the presence of a different monolayer organization could lead to a different interacting behavior in the presence of membranes.

We performed the analysis of the interaction with DOPC model membrane evaluating *in silico* the adhesion trend for different AuNP-PEG systems characterized by both mixed and homoligand self-assembled monolayers. NPs were placed in bulk solution and let approach freely the membrane. NPs reached and then maintained an equilibrium distance value, suggesting that binding is stable over time (Figure 36).

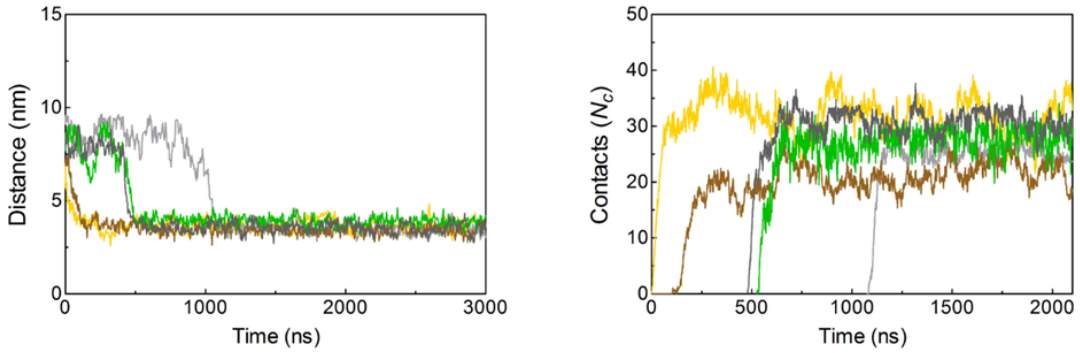

Figure 36: ***Time sequence of the distance and number of contacts between SAM-^{Au}NP and DOPC membrane****. The sequence measures the distance from the center of mass of the NP and membrane surface over the first 3 µs (left) or the number of contacts N_C between ligand and membrane over the first 2 µs (right) for the different NPs. A contact was counted when the distance between one bead of NP and one bead of DOPC was smaller than 0.6 nm. Color code: M1-C8T/F8P, brown; M2-C8T/F8P, light grey; F8P, yellow; C8T, green; C8P, dark grey.*

Regardless of the monolayer composition, once the NP has established its first contact with the upper leaflet, it was rapidly stabilized in the proximity of the membrane and quickly reached a fully adsorbed state (Figure 37).

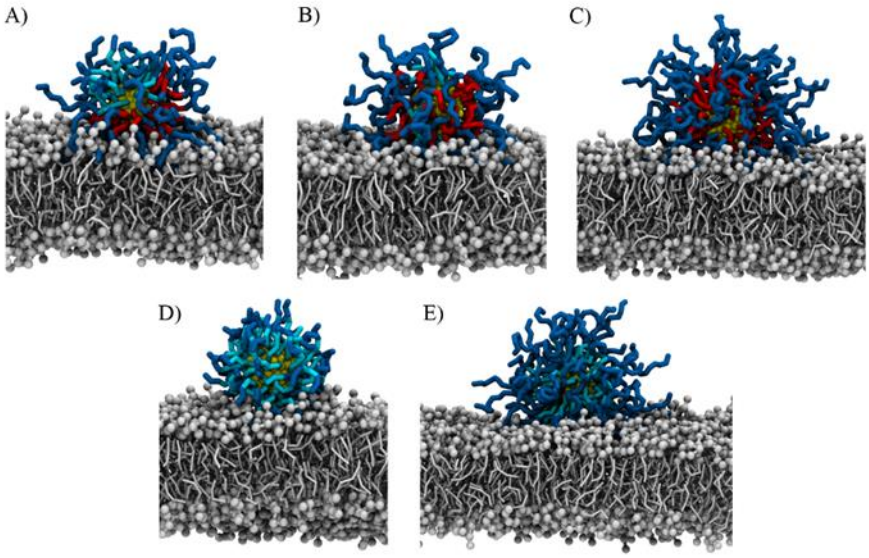

Figure 37: ***Equilibrated simulation snapshots of SAM-^{Au}NP interacting with DOPC membranes****. M1-C8T/F8PEG (A), M2-C8T/F8P (B), F8P (C), C8T (D), C8P (E) adopt a position close to DOPC-water interface. The hydrophilic poly(ethylene oxide) component of the ligands is colored in blue, while the hydrophobic F8-/C8-chains are highlighted in red and cyan, respectively. The gold core is shown in yellow. DOPC headgroups and tails are portrayed as grey spheres and sticks, respectively. Water molecules and inorganic ions are not shown for clarity.*

The values of free energy of binding were calculated through the umbrella sampling technique. The umbrella sampling allows to calculate the free energy difference between the bind and unbind NP state through virtual unbinding experiments. Potential of mean force (PMF) profiles, see Figure 38, were calculated for all the systems and showed how the free energy changed due to the particle adhesion as a function of the distance from the center of the membrane.

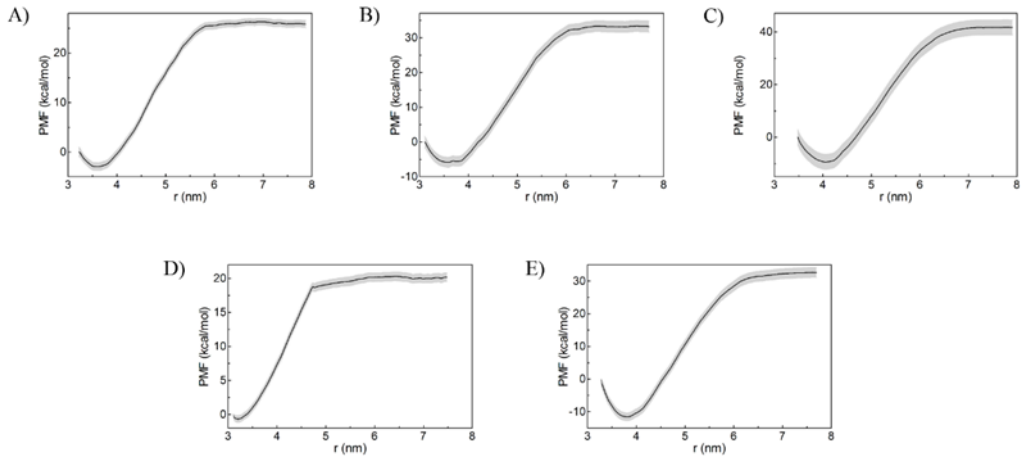

Figure 38: ***Free energy profiles (PMF) related to the transfer of SAM-^{Au}NP from the DOPC-water interface to solvent solution.*** *M1-C8T/F8P (A), M2-C8T/F8P (B), F8P (C), C8T (D), C8P (E). Standard deviations are reported as a grey shaded area.*

The difference in force value between the bulk water and the lipid-interface state calculated from the PMF profiles is directly related to the energy required to detach the NP from the membrane surface (ΔG_{adh}) and this represents a measure of the binding strength of the given SAM-AuNP. ΔG_{adh} values for the five systems investigated are reported in Table 3.

Starting from the homoligand systems we considered three different NP types. The first and the second present ligands with the same PEG length (8 monomers) but differ in the hydrophobic part. The second and the third present the same hydrophobic part but differ in the length of PEG (8 monomers and 3 monomers). From the values of ΔG (Table 1, Table 8: Computational analysis of adhesion energy and contacts at the interface between SAM-AuNPs and a DOPC membrane. SAM-AuNP/DOPC interaction assessed in terms of: [a)] Adhesion energy (kcal mol^{-1}); [b)] Total number of NP ligands in contact with the lipid bilayer (distance < 0.6 nm between ligand and lipid beads in CG simulations); [c)] Contribution to the total number of contacts N_C pertaining to C8TEG and F8PEG chains, respectively; [d)] Relative number of NP-DOPC contacts involving hydrophilic ligand moieties (PEG, TEG);

[e] Relative number of NP-DOPC contacts involving hydrophobic ligand moieties (C8, F8).) we could appreciate that NPs with the same PEG length, that present the perfluorurate hydrophobic part, have a higher affinity with the respect of NP with the hydrogenate hydrophobic part. Moreover, the presence of the longest PEG chain seems to favor the interaction with the external part of the bilayer. This supports the hypothesis that ligand flexibility in SAM-AuNPs enables them to expose the inner hydrophobic portion of the shell when they face the membrane, indicating a highly adaptive behavior.

SAM-AuNP	ΔG_{adh} [a]	N_C [b]	**Contacts**	
			Hydrophilic (%) [d]	**Hydrophobic (%)** [e]
M1-C8T/F8P	-28.6 ± 1.5	21 ± 2 (0/21) [c]	59	41
M2-C8T/F8P	-38.9 ± 1.0	25 ± 1 (3/22) [c]	63	37
F8P	-51.0 ± 1.2	32 ± 2	73	27
C8T	-20.7 ± 0.7	28 ± 2	53	47
C8P	-44.1 ± 0.8	31 ± 2	72	28

Table 8: Computational analysis of adhesion energy and contacts at the interface between SAM-AuNPs and a DOPC membrane. SAM-AuNP/DOPC interaction assessed in terms of: [a] Adhesion energy (kcal mol^{-1}); [b] Total number of NP ligands in contact with the lipid bilayer (distance < 0.6 nm between ligand and lipid beads in CG simulations); [c] Contribution to the total number of contacts N_C pertaining to C8TEG and F8PEG chains, respectively; [d] Relative number of NP-DOPC contacts involving hydrophilic ligand moieties (PEG, TEG); [e] Relative number of NP-DOPC contacts involving hydrophobic ligand moieties (C8, F8).

Therefore, we investigated if the presence of nanostructured morphologies influenced the adhesion and we found out that Stripe morphology promoted more favorable interactions. To have a deeper insight of this different behavior, we characterized the nano-bio interface calculating the number of contacts and the normalized number of contacts, of the PEGylated and non-PEGylated part, with respect to the overall contacts number. Homoligand NPs had the higher number of contacts and the PEGylated part mediated the interaction while the presence of a nanostructured organization decreased the number of total contacts increasing contacts of the hydrophobic part (almost all were F8PEG).

It is possible that, when patterned NPs approached the lipid bilayer, the greater internal constraint due to increased chain association is reflected in a decreased capacity of ligands to adapt in a responsive manner. Consequently, the average number of chains involved in the binding event is lower than in the case of homoligand NPs. This distinct, morphology-

dependent behavior was surprising given the relatively limited difference in F8PEG and C8TEG domain dimension due to the small core size of the nanoparticles.

The different affinity towards the membrane have been complemented and confirmed by the SPR experimental results performed by Dr. Filomena Guida of the group of prof. Sabrina Pacor and prof. Alessandro Tossi, Department of Life Sciences, University of Trieste). (*Figure 1*)

The sensorgrams, obtained through the SPR analysis (Fig.39) confirmed that both Janus and Striped NPs are able to bind the DOPC liposomes. In both cases the sensorgrams showed a rapid binding kinetics, supporting the MD prediction, and a concentration-dependent increasing in RU that suggested a good adhesion capacity to the membrane surface. Interestingly, the affinity constant (K_D) estimated from the binding curves was significantly lower (K_D = 80 uM) for the Striped system than for the Janus one (K_D = 330 uM).

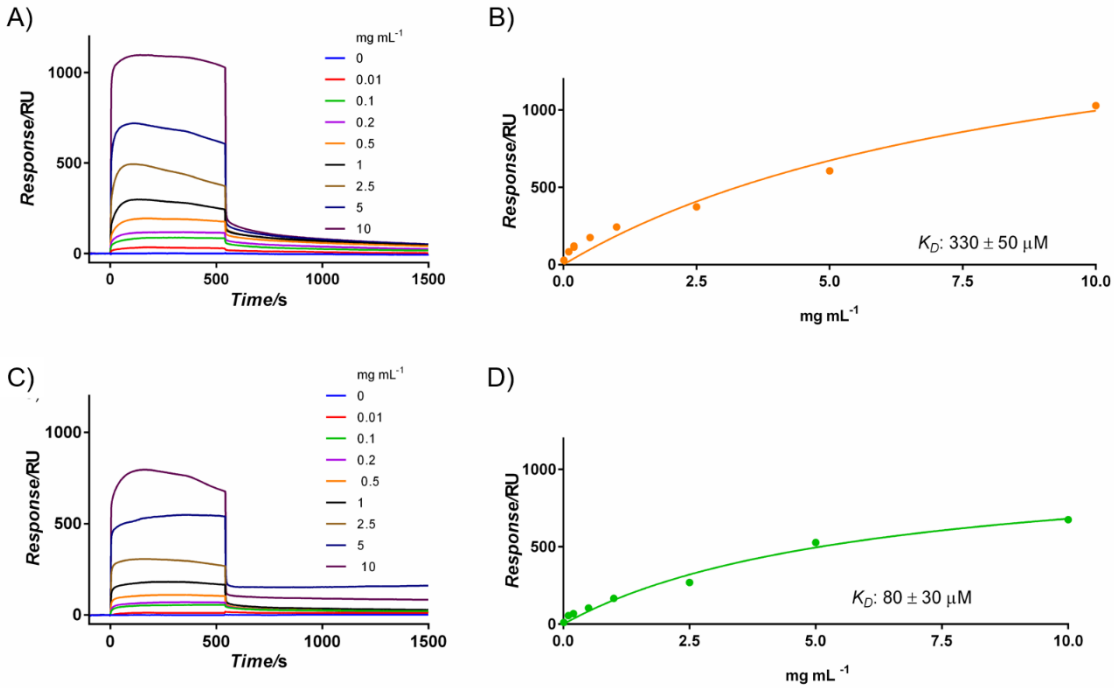

Figure 39: ***Binding sensorgrams (A-C) and binding curves (B-D) for M1- (A-B) and M2-C8T/F8P (C-D) AuNPs.*** *Sensorgrams were obtained flowing SAM-AuNPs at increasing concentrations (as shown) over DOPC LUVs immobilized on an L1 sensor chip. Binding curves were fitted using the "Affinity-Steady State" mathematical model. Shown is one experiment out of five different evaluations with very similar results.*

To complete the comparison, the affinity of the homoligand nanoparticles was tested using the same SPR setup. Both of the PEGylated homoligand NPs exhibited a good binding capacity to the DOPC LUV surface. F8P showed a marginally higher affinity than C8P (K_D

= 60 ± 10 and 118 ± 22 μM, respectively), experimentally confirming MD results indicating the higher affinity of fluorinated ligands toward DOPC.

4.3 Interaction of self-assembled monolayer protected nanoparticles with complex model membranes

In order to reduce the gap between single component synthetic bilayers and real multicomponent cell membranes, we built a multi-component membrane model. A ternary mixture of DOPC, sphingomyelin (SM) and cholesterol (CH) was chosen as a representative system, with cholesterol levels (∼25%). Atomic Force Microscopy (AFM) images of a supported DOPC/SM/CH bilayer were obtained and used to develop a multicomponent molecular model able to reproduce the experimental domain organization (Figure 40).

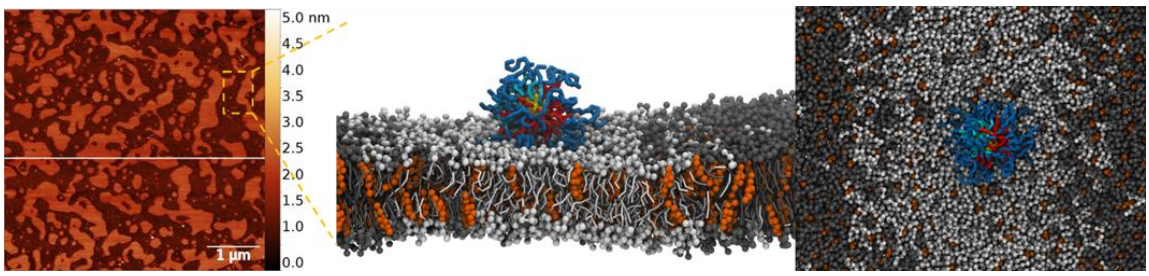

Figure 40: AFM image of supported DOPC/SPHI/CHOL bilayer and equilibrated simulation snapshot of M1-C8T/F8P interacting with the same ternary mixture. (Left panel) AFM images (scan size 5x5 nm^2) in non-contact mode of a supported membrane prepared from a DOPC/SPHI/CHOL mixture with scale bar 1 μm. Lateral view (middle panel) and top view (right panel) of a M1-C8T/F8P adhered to the DOPC/SPHI/CHOL bilayer. The hydrophilic PEG component of the ligands is colored in blue, while the hydrophobic F8 and C8 moieties are highlighted in red and cyan, respectively. The gold core is shown in yellow. DOPC headgroups and tails appear as light grey spheres and sticks, respectively, while for SPHI they are in dark grey. CHOL molecules are highlighted as orange spheres. Water and inorganic ions are not shown for clarity.

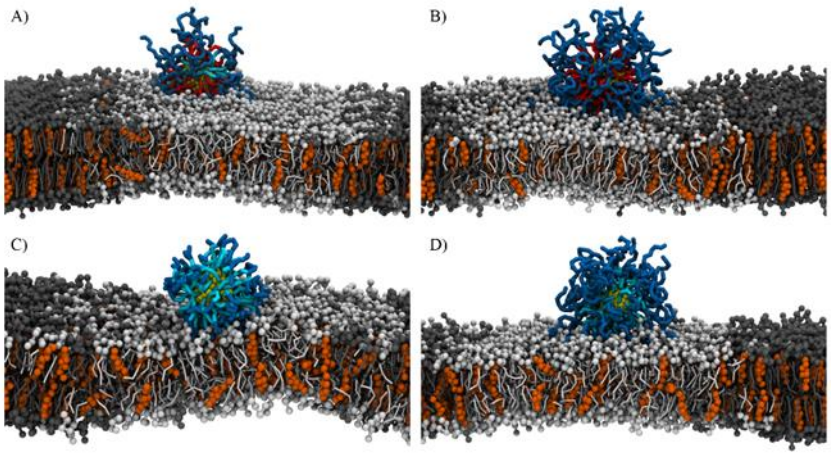

Figure 41: ***Equilibrated simulation snapshots of SAM-^{Au}NP interacting with DOPC/SPHI/CHOL membranes****: M1-C8T/F8P (A), F8P (B), C8T (C), C8P (D). The hydrophilic poly(ethylene oxide) component of the ligands is colored in blue, while the hydrophobic F8 and C8 chains are highlighted in red and cyan, respectively. The gold core is shown in yellow. DOPC headgroups and tails appear as light grey spheres and sticks, respectively, while for SPHI they are in dark grey. CHOL molecules are highlighted as orange spheres. Water and inorganic ions are not shown for clarity.*

Also in this case, we performed simulations for both mixed and homoligand NPs and we were interested in understanding if the presence of a multicomponent membrane composition would lead to a different behavior once the NPs come in contact with the bilayer.

We found out that, regardless the SAM organization, all the NPs preferred to contact the membrane within the DOPC-rich domain. As previously, both the striped and Janus system expose most the fluorinated ligands. (Figure 40 and Figure 41).

The main features of the NP/multi-component-membrane interface was preserved with respect to a simple DOPC membrane; in terms of the relative number of the hydrophilic/hydrophobic contacts for each system and the increased *Nc* in homoligand SAMs with respect to the nanostructured monolayers (Table 9). However, the absolute N_C values decreased by 2-3 contacts as compared with DOPC membrane. It is well established that the presence of cholesterol can greatly influence the physical properties of the membrane (such as fluidity), so the reduction in the number of contacting ligands may be an effect linked with the amount of CH present in the system.

SAM-AuNP	ΔGadh a)	NC b)	Contacts	
			Hydrophilic (%) d)	Hydrophobic (%) e)
M1-C8T/F8P	-22.0 ± 1.2	18 ± 2 (0/18) c)	60	40
M2-C8T/F8P	-31.1 ± 1.1	23 ± 1 (2/21) c)	66	34
F8P	-42.3 ± 1.4	29 ± 1	75	25
C8T	-15.5 ± 0.9	26 ± 1	55	45
C8P	-37.0 ± 1.1	28 ± 1	74	26

Table 9: Computational analysis of adhesion energy and contacts at the interface between SAM-^{Au}NPs and a DOPC/SPHI/CHOL membrane.

This new set of simulations confirmed that the molecular information associated with the nanoscale organization of the NP remains as relevant to multi-component synthetic membranes as for the mono-component ones.

Taken together, results suggest that even small changes in the molecular features of the monolayer may significantly affect the interaction of SAM-AuNPs with model membranes demonstrating the key role of nanoparticles' interfacial properties in their functional activity. Moreover, these small changes in the molecular structure of the monolayer lead to a substantial difference in cells that can be appreciate by confocal microscope analysis and flux cytometry with absence of citotossicity appreciated. (Appendix C)

4.4 Interaction of coated gold nanoparticles with proteins

The interaction of proteins with nanomaterials needed to be distinct from the interaction of proteins with bulk materials of the same composition. The highly curved surfaces of nanomaterials influenced protein–protein interactions. (254) For example, there is substantial cooperativity during the adsorption of human serum albumin to 100 nm, but not 5 nm gold nanoparticles. (255) For example, the density of albumin adsorbed to gold nanoparticles increases significantly as the size decreases below 30 nm. (256) Increasing surface curvature tends to lower the affinity of a protein to the nanomaterial, presumably by decreasing the area of interaction. On the other hand, proteins adsorbed to highly curved nanoparticles tended to undergo fewer changes in conformation than those adsorbed to less curved surfaces. However, the tendency of smaller nanoparticles to preserve protein conformation seems to be protein-dependent. Fibrinogen, for example, undergoes larger structural changes on smaller rather than larger SiO_2 nanoparticles.

Most studies carried out so far involved NPs with homogeneous surfaces while only a few have considered the influence of surface heterogeneity at the nanoscale, especially in a comparable size range to proteins. Some studies on patterned NPs have shown that the surface ligand composition and morphology affect how proteins bind. Fluorescence quenching, dynamic light scattering (DLS), circular dichroism (CD), and isothermal titration calorimetry (ITC) have been performed with striped and randomly monolayer protected NPs suggesting different "side-on" or "end-on" bovine serum albumin (BSA) conformations on gold NP, depending on its monolayer organization. If the shell presented randomly distributed ligands, the binding was mainly mediated by electrostatic interactions, while for a striped surface, there was a combination of different interactions due to the presence of both polar and apolar groups in in the shell. (124). In another combined experimental/computational investigation, interactions of cytochrome *c* with nanostructured surfaces formed by mixtures of 6-mercapto-1-hexanol (MH) and octanethiol ligands were explored using both protein assays and computational MD simulations (125). The key role of the surface structural and chemical heterogeneity of nanoscale patterned NPs was confirmed by both experimental and computational results. It was shown that the interaction between proteins and NPs is determined by the surface heterogeneity of the NPs, but also depended both on the scale of protein heterogeneity and its size (126; 242).

The interaction of proteins with nanomaterials needed to be distinct from the interaction of proteins with bulk materials of the same composition. The highly curved surfaces of nanomaterials influenced protein–protein interactions. (254) For example, there is substantial cooperativity during the adsorption of human serum albumin to 100 nm, but not 5 nm gold nanoparticles. (255) For example, the density of albumin adsorbed to gold nanoparticles increases significantly as the size decreases below 30 nm. (256)

Rational design of NPs remained a challenge due to the lack of a deep knowledge of the molecular mechanisms underlying the formation of the protein corona on different NPs surfaces. Having this in mind, we considered a second biointerface for our M1- and M2-C8TEG/F8P NPs (see Chapter 3.1). These nanoparticles feature a Janus and striped surface, respectively, and our calculations, supported by experimental evidences, demonstrated that their behavior in contact with simple and complex lipid membranes is different. Thus, we wondered if this is the case also in presence of proteins. We choose the Human Serum Albumin (HSA) upon all proteins because it is the most abundant serum protein and it is the first protein that typically binds the surface of nanomaterials.

4.4.1 Human Serum Albumin computational results

4.4.2 Computational methods

4.4.2.1 Coarse-grained simulations

The coarse-grained (CG) models of M1- and M2-C8TEG/F8P NPs were built as previously descripted in Chapter 3.2.1.2, while the CG model for the HSA was obtained thought the standard procedure for Gromacs. Using the *martinize.py* script the atomistic structure of the HSA was converted into a CG model and a suitable Martini topology was generate, then the CG protein was minimized and solvated with water and counter ions (267). Then each initial configuration was first equilibrated in NVT for 16 ns and then in NPT for other 100 ns. Then, we performed simulations of 2 μs for each system.

4.4.2.2 Atomistic simulations

The atomistic file for the M1- and M2-C8TEG/F8P NPs were the same used in Chapter 3.2.1, while the pdb file of the HSA has been downloaded from the Protein Data Bank. Each initial configuration, constructed starting from the correspondent CG model, was first equilibrated for 5 ns, temperature was then raised to 300 K in molecular dynamics (MD) simulation (Langevin thermostat, time step of 1 fs, collision frequency 1.0), followed by the equilibration of the density for 10 ns with a Berendsen barostat (pressure relaxation time of 2 ps, time step of 2 fs). At the end, we switched to a Monte Carlo barostat and performed data collection for a total of 2 μs. AA simulations were performed by means of AMBER 14 suite of software (196), employing gaff2 (197, 198) forcefield.

4.4.3 Results

We started considering the interaction of HAS with M1- and M2-C8T/F8P NPs at coarse-grain level. This was necessary to simulate a system in which the relative size of protein and nanoparticle is comparable. The NP surface cannot be thus represented as a flat surface and both protein and ligands possessed great flexibility and need time to reach the final equilibrium state.

Consequently, we developed a computational CG procedure which considered a 2:1 protein-nanoparticle binding for each NPs. We placed the two HSA far from the NP surface at a

distance which was a compromise that let both the nanoparticle and the protein time and space to find their respective energetically favorable position (Figure 43). The two HSA were placed in solution in the *up* position due to preliminary calculations, performed on a 1:1 NP:HSA system (Figure 42), that pointed out that this was the preferential binding position for the HSA.

Figure 42: HSA starting position. Up (left), back-on (right).

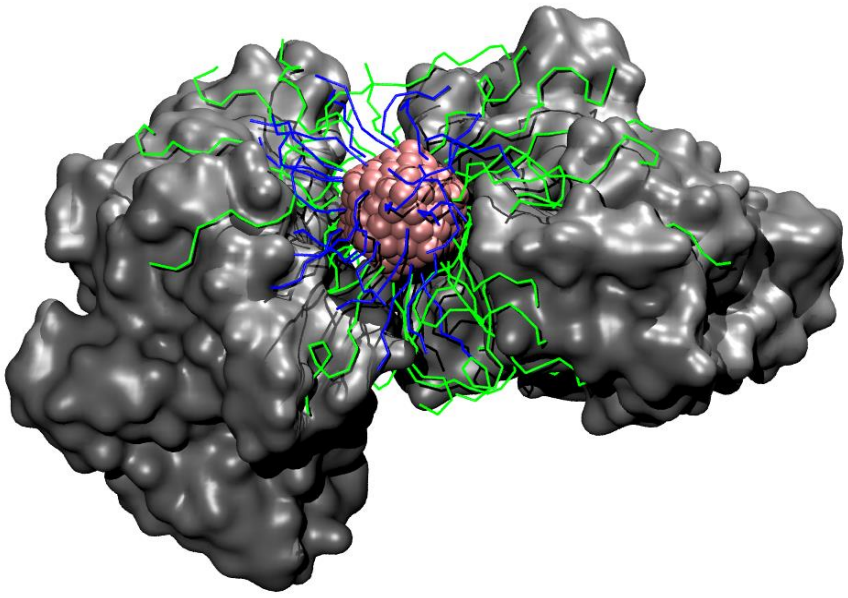

Figure 43: equilibrated snapshot of a M1-C8T/F8P-AuNPs interacting with the two HSA. F8P ligand (green), C8T ligand (blue). Solvent not shown for clarity.

From the computational evidences the two HSA were able to bind the nanoparticle and both NP and proteins had time and space to adjust its relative binding position. Therefore, we investigated which kind of amino acids were involved in the interactions. It turned out that the amphiphilic amino acids were the ones that contact more the nanoparticle shell, consistently with the amphiphilic character of our ligands. In particular, Lysine (Lys), Glutamic acid (Glu) and Aspartic Acid (Asp) (Figure 44) were the ones that made more contacts with the surface of the nanoparticle. This is probably due to the chemical nature of their side chains. We hypothesized that the longer is the alkyl part of the chain the higher is the total number of contacts and that also the difference in bulkiness of the side chains may play a role in the interaction. In particular, Lys, which presents the longest alkyl chain and thinner side chain, is the one that made the highest number of contacts with respect to Glu and Asp, which present a gradually shorter alkyl chain and bulkier side chain, respectively.

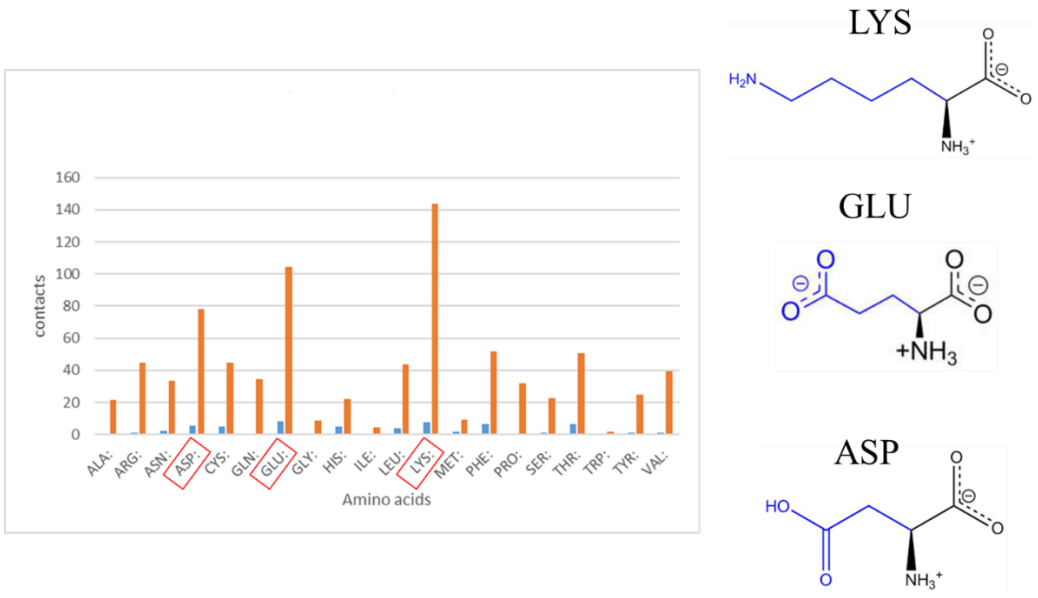

Figure 44: Histogram showing the number of the amino acid involved in binding the human serum albumin. Blue column represented the number of amino acid that contacted the C8T ligand, orange column the number of amino acid contacting the F8P ligand. On the right the chemical representation of the three most contacting amino acids.

Further useful insights (free energy of binding ΔG_b, number of contacts with HSA involving the PEGylated and the non-PEGylated part of the ligands, number of amino acids contacting the F8P and C8T chains) were also collected and are reported in Table 10. No major differences appear in the value of the free energy of binding, suggesting that the different

nanostructure organization does not play a role in it, in contrast to what happened with membranes. Albumin preferred to interact with the F8P ligands rather than with the C8T, contacting in greater extent both the PEGylated and the non-PEGylated part of the chain. This is probably due to the great flexibility of both protein and ligands, which allowed thiols to follow exactly the conformation of the protein surface. As a consequence, also the amino acid involved in binding came in contact mostly with the fluorinated thiols.

	ΔG_b [kcal/mol]	% non-PEG C8T	% non-PEG F8P	% PEG C8T	% PEG F8P	Contacts res-F8P	Contacts res-C8T
M2-C8T/F8P	-3318.3 ± 2650.2	28.7 (19)	57.7 (36)	30.6 (19)	80.8 (36)	713	38
M1-C8T/F8P	-3290.9 ± 2704.9	15.4 (24)	84.0 (32)	16.2 (24)	93.6 (32)	845	15

Table 10: comparison of the interaction of HSA with M1- and M2- NPs. In the table are reported the values of free energy of binding ΔG_b, number of contacts involving the PEGylated components (% PEG C8T/F8P), number of contacts involving the non-PEGylated parts (% non-PEG C8T/F8P), number of amino acid contacting F8P (contacts res-F8P) and the C8T (contacts res-C8T) ligands.

The CG model employed due to the great complexity of the system did not provide a rationale to determine if different morphologies influenced the binding affinity towards the human serum albumin as they did with the membranes. Probably this is related, again, with the comparable size of the two actors or it could be that little differences cannot be appreciated at this level of coarse graining. For this reason, we set up an atomistic model of the systems and from the preliminary results, at a visual inspection of the trajectories (Figure 45), seems that the binding of the striped NPs involved a higher number of ligands which would probably result in a higher affinity with respect to the Janus NPs. Further evaluations are, to date, in progress.

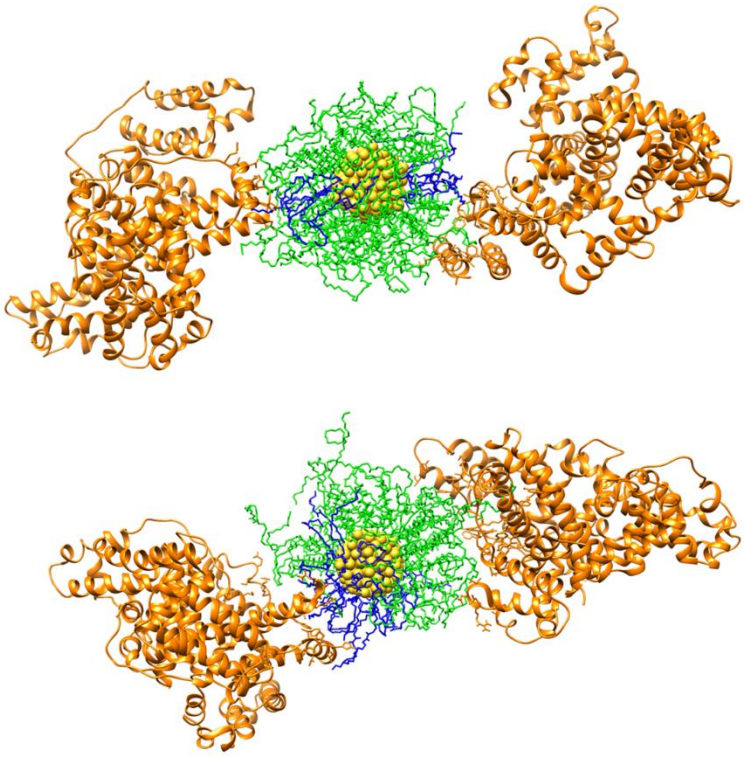

Figure 45: 2 HSA binding Striped-AuNP (up), Janus-AuNP (bottom). HSA in orange, C8TEG in blue, F8PEG in green and gold in yellow.

Chapter 5. *Supramolecular binding of small molecules in coated gold nanoparticles*

5.1 Molecular investigation of crystal violet binding to coated gold nanoparticles

Monodisperse AuNPs functionalized in polymer encapsulations doped with photosensitized dyes have demonstrated remarkable antimicrobial properties. For example, crystal violet (CV) and methylene blue (MB) were incorporated into medical grade polymers before encapsulating sub-10nm AuNPs. Significant antimicrobial enhancement was achieved both in dark and light conditions with the presence of AuNPs, especially the AuNPs of 2 nm size. (257-259) However, the detailed physical/chemical mechanism of this intriguing interplay has not been revealed thoroughly. Considering AuNPs have no bactericidal effects intrinsically, it is of great importance to investigate the mechanism of this synergistic effect comprehensively. In this study, we aim to attach CV directly to the AuNPs with thiol capping by inducing both electrostatic and intermolecular interactions. Adjusting the experimental conditions enables the optimization of the association constant. To this aim, we investigated by means of molecular dynamics calculation the interaction of CV covered with a self-assembled monolayer of 11-mercaptosulfonic acid (MUS). As a dye, the Crystal Violet changes its color depending on the pH and at different pH presents different protonation states. Accordingly, three different conditions were taken into account for calculation, acid, neutral and basic pH.

This work was conducted during my stay abroad as a part of collaboration with the group of prof. Stefan Guldin (UCL, London, UK).

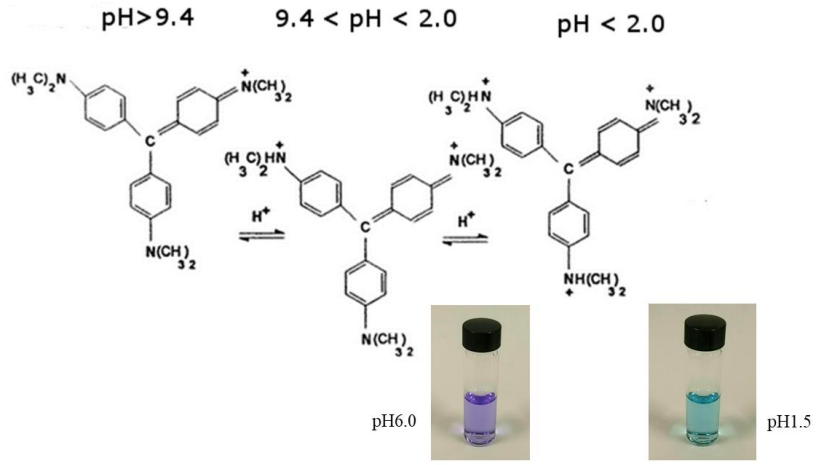

Figure 46: Crystal Violet protonation states carrying a different charge and changing its color depending on the pH

5.1.1 Computational details

These homoligand MUS modified Au NPs were simulated at the atomistic level employing Amber software, gaff2 Force Field and the TIP3P water model. Atomistic simulations were performed in explicit solvent (water) and ions (Na+ and Cl-) at room temperature. All systems were minimized by 1000 steps of Steeped Descent followed by 3000 steps of Conjugated Gradient algorithms. The temperature was then raised to 300 K in 20 ps of NVT molecular dynamics (MD) simulation (Langevin thermostat, time step of 1 fs, collision frequency 1.0), followed by the equilibration of the density for 10 ns with a Berendsen barostat (pressure relaxation time of 2 ps, time step of 2 fs). At the end, we switched to a Monte Carlo barostat and performed data collection for a total of 2 us. AA simulations were performed by means of AMBER 14 suite of software (196), employing gaff2 (197, 198) forcefield. Regarding the structure of the CV molecule, to characterize the different charges present at different pH (Figure 46), we used the Resp Esp charge Derived (R.E.D) tool to parametrize it. R.E.D minimizes molecular structures and allows to automatically derive RESP and ESP charge values to build force field libraries for new molecules/molecular fragments.

Then we performed the energetical analysis (using the MMPBSA procedure) for each system. For the entropy evaluation the *&nmode* calculation was used, which is unique to the normal mode calculations used to approximate vibrational entropies, while to evaluate the enthalpic components the *&pb* calculation was used. The *&pb* is unique to Poisson Boltzmann calculation.

5.1.2 Results

To begin, we developed a model of a 1:1 AuNP:CV system for each pH to determine whether the starting position of the CV might affect its final binding position on the NP surface. In particular, we placed the CV molecule in standing-up (Figure 47a on the left) and in a laying-down position (Figure 47a on the right). From the atomistic simulation results, it was clear that the Crystal Violet molecule presented a preferential binding position independently from the initial position and the pH. From a visual inspection of the trajectories, the CV molecules preferred to stay bound in the free space through the MUS bundles close to the alkyl chain of the thiols (Figure 47b).

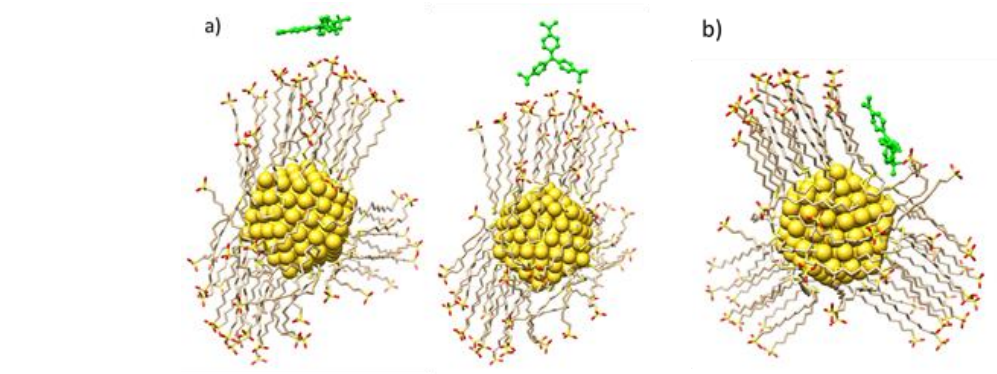

Figure 47: Snapshots of the molecular dynamics trajectory showing: a) different starting positions, b) final binding state for 1:1 MUS-AuNP at pH < 2.0. Simulations were carried in water and in presence of ionic strength (100 mM NaCl). Solvent is not shown for clarity.

To distinguish which kind of interactions drive the binding of CV to the functionalized surface at the different pH, we resorted to MMPBSA analysis. The graphs clearly show the affinity of the CV is higher at acid pH and decrease at basic pH (Figure 48).

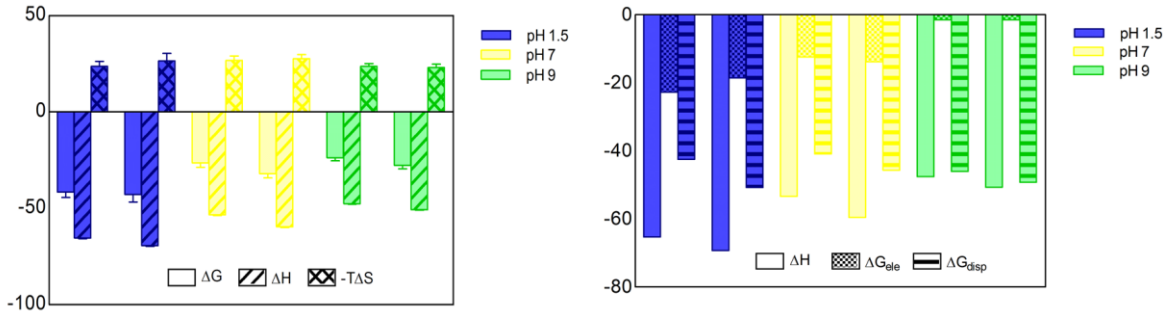

Figure 48: Averaged MM/PBSA binding energies (kcal/mol) for AuNP:CV 1:1 systems. Free energy of binding (ΔG), and enthalpic (ΔH) and entropic (-TΔS) terms (left panel). Electrostatic and hydrophobic contribution to the enthalpy binding component (right) panel). Data are reported for two different CV starting positions.

From the thermodynamics, it is known that the free energy of binding (ΔG) depends on a balance of entropic (ΔS) and enthalpic (ΔH) components ($\Delta G = \Delta H - T\Delta S$). The values revealed that, while the ΔG decreased within the pH, the variation in entropy ΔS was always unfavorable to the binding regardless the pH and almost constant in the three different conditions. At the same time, the enthalpic contribution was favorable to the binding and decreased with the pH (Figure 48 left panel). It is clear that the interaction is essentially enthalpy driven. Therefore, to evaluate which enthalpic component mainly contribute to the binding of the CV, the ΔH term was analyzed in term of its electrostatic (ΔH_{ele}) and dispersive (ΔH_{disp}) components. Plotting the data (Figure 48 right panel), the electrostatic component decreases within the pH for all systems, while the dispersive one remains constant over the pH and drives the molecular binding. Due to the chemical structure of the molecules involved in the interaction, it was expected that the driving force had to be electrostatic. However, the computational results clearly show that the main contribution comes from the hydrophobic forces.

Furthermore, to mimic an environment as close as possible to the experimental conditions and to figure out which is the maximum payload for these NPs at the three-different pH, atomistic simulations were then performed with an increased number of CV molecules (5, 10, 20).

The results showed that, regardless the pH, not all the 20 CV molecules were bound demonstrating that the maximum payload for these nanoparticles had been reached. At basic pH, about 17 molecules stay bound, while 12 and 13 CV are able to stably bind the gold nanoparticle at acid and neutral pH, respectively (Figure 49). In all cases, the dye bound in the free space through the bundles, when possible, as seen in the case with only one CV.

When possible, the dye occupied the same preferential binding position found in the simulations with one CV molecule.

The energy analysis performed on all systems at the three-different pH reveals that the trend emerged for 1:1 systems is maintained also at higher CV loadings.

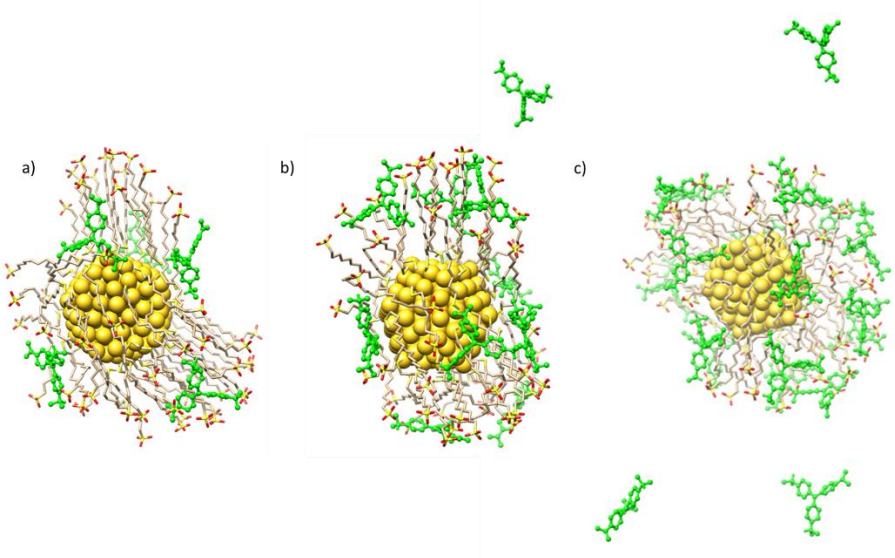

Figure 49: Equilibrated snapshot of the molecular dynamic trajectories showing: a) 5 CV:1 AuNP, b) 10 CV:1 AuNP and c) 20 CV:1 AuNP. Simulations were carried in water and in presence of ionic strength. Solvent is not shown for clarity.

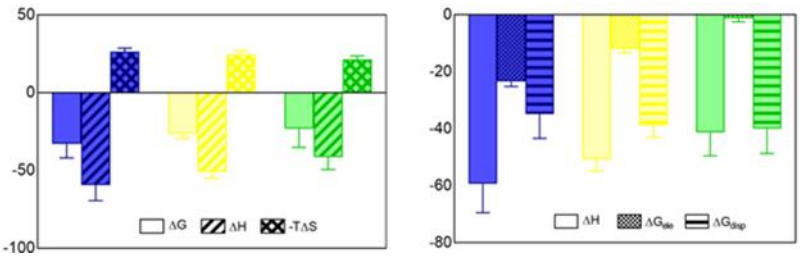

Figure 50: CV-averaged MM/PBSA binding energies (kcal/mol) for the highest payload systems. Free energy of binding (ΔG), and enthalpic (ΔH) and entropic (-TΔS) terms (left panel). Electrostatic and hydrophobic contribution to the enthalpy binding component (right) panel. Data are averaged on the number of CV molecules bound at the highest payload for each pH value (acid pH in blue, neutral pH in yellow and basic pH in green).

As seen before, the affinity is higher in acid conditions than in neutral and basic ones (Figure 48 left panel). While the binding energy decreases as a function of pH, the entropic term ΔS remaines always unfavorable to the binding and almost constant regardless the pH. Overall, the binding is driven by enthalpy and becomes less favorable at basic pH. The enthalpic contribution ΔH was split into its electrostatic (ΔH_{ele}) and dispersive (ΔH_{disp}) components

(Figure 50 right panel). Analyzing the data, the electrostatic component decreases with the pH, while the dispersive one remains constant regardless the pH. Taking all the evidences together, it is clear that the binding of CV to a MUS-modified NPs is not driven by electrostatic forces but by the dispersive ones.

So far, we have looked at the binding event as a whole. Due to the presence of multiple binding sites, we were also interested in investigating if the binding of a CV molecule influences the affinity of the other CV units, namely if there is a sort of cooperative effect. We analyzed the energetical values of ΔG, ΔH and ΔS for each CV molecule bounded to the AuNP together with the corresponding average values and the ones of the relative 1:1 system (Figure 51).

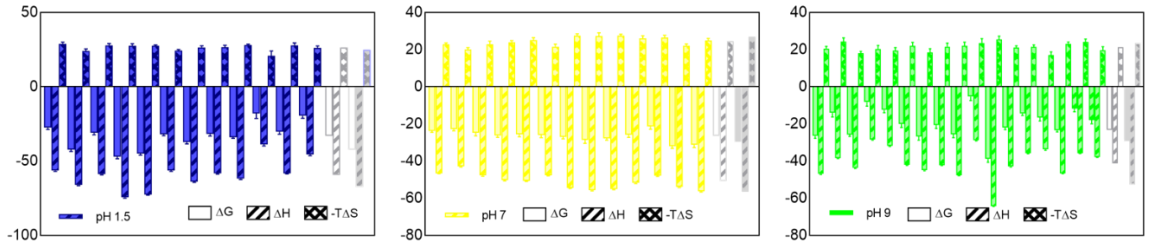

Figure 51: Main components (ΔG, ΔH, ΔS) of the free energy of binding for the systems at different pH (acid in blue, neutral in yellow and basic in green). The values relative to ach CV bound (full bars) together with the average values (white shaded bars) and the relative 1:1 systems.

Based on these evidences (Figure 51), it seems that the binding may be not cooperative as the main energetic parameters almost lay in the same range and we could take the average values as representative for all the systems. The same behavior could be observed when isolating the enthalpic term (Figure 52).

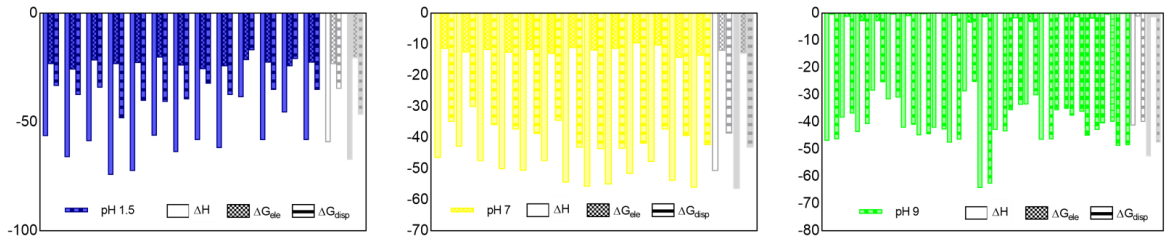

Figure 52: 20CV systems MM/PBSA binding energies (kcal/mol) of each bounded CV molecule together with the average values and the relative 1:1 values. The values relative to each CV bound (full bars) together with the average values (white shaded bars) and the relative 1:1 systems

Further analysis has been conducted to gain more details on the molecular properties of the interaction involving MUS-AuNPs and CV. In particular, the number of MUS ligands contacting each CV molecule (with a contact distance of 5Å) and the contact solvent Accessible Surface Area (SASA) of CV, averaged over all the molecules in stable binding (Table 11).

pH	1.5	7	9
Total contacts	69	81	99
Averaged contacts	6	6	6
SASA ($Å^2$)	155 ± 37	192 ± 30	192 ± 50

Table 11: Total and averaged number of contacts (contact distance 5Å) between CV and MUS ligands and contact Solvent Accessible Surface Area (SASA) of single CV bound to the monolayer.

.

The data indicate that on average each CV molecule is able to interact with six MUS ligands and this number is not much influenced by the pH of the solution. Clearly, the total number of contacts increases at higher pH, since the number of CV molecules bound is higher than that at lower pH. At the same time, each CV binds the monolayer exposing a surface area, which is slightly lower at lower pH with respect to neutral and acid pH. It is possible that, at acid pH, when CV brings three charges, the electrostatic repulsion between adjacent positive charged molecules is not fully screened by negative flexible ligands. As a consequence, the molecular conformation of the binding site may be slightly different and this reflects in a different value of the contact SASA parameter. This speculation also agrees with the fact that the monolayer is able to accommodate the lowest number of CV molecules when the pH is acid.

5.2 Molecular sensors for doxorubicin binding

One major need of oncologists is to know in real-time the drug concentration in blood when treating patients with chemotherapy. Especially for anticancer drugs the therapeutic window, i.e. the drug range between a concentration too low to reach the therapeutic goal and a concentration causing severe adverse toxic effects in the patient, is quite small. (260)

Conventional standard methods for therapeutic drug monitoring (261) are rather slow and costly off-line procedures. For example, gold nanoparticles developed so far were able to bind a target molecule such as the commonly used chemotherapy drug doxorubicin (DOXO) in molecular receptors formed by the ligand shell on their surface but they were not sufficient to perform phase transfer from hydrophilic to hydrophobic environment. (262-265) These receptor sites were created by the molecular arrangement of a mono or binary mixture of functional ligands. One ligand, normally, was responsible for AuNPs solubility in various media (solvent, plasma, blood) and the second one, normally in minority, conducted the binding event. This strategy will lead to a robust and reliable point-of-care sensing platform with real time precision for sensing of chemotherapeutic drugs in small samples of blood samples at very low drugs concentrations (Figure 53). Therefore, innovative drug capturing nanoparticles capable to bind DOXO from human blood and selectively phase transfer upon binding are pivotal.

The discrimination between drug and its metabolite would be carried out on the atomic level and only the right molecule will undergo transfer into a different phase (e.g. liquid crystal), where their concentration will be measured. The receptor sites can be created by the molecular arrangement of a binary mixture of bifunctional ligands. Thiol group anchored the ligands to the gold NPs and the second functional groups forming the receptor site could be designed in order to perfectly match the desired system with calculated affinity. The perfect DOXO receptor would be chosen accordingly with different NP parameters (ligand composition, size, etc.) to improve the binding properties to DOXO.

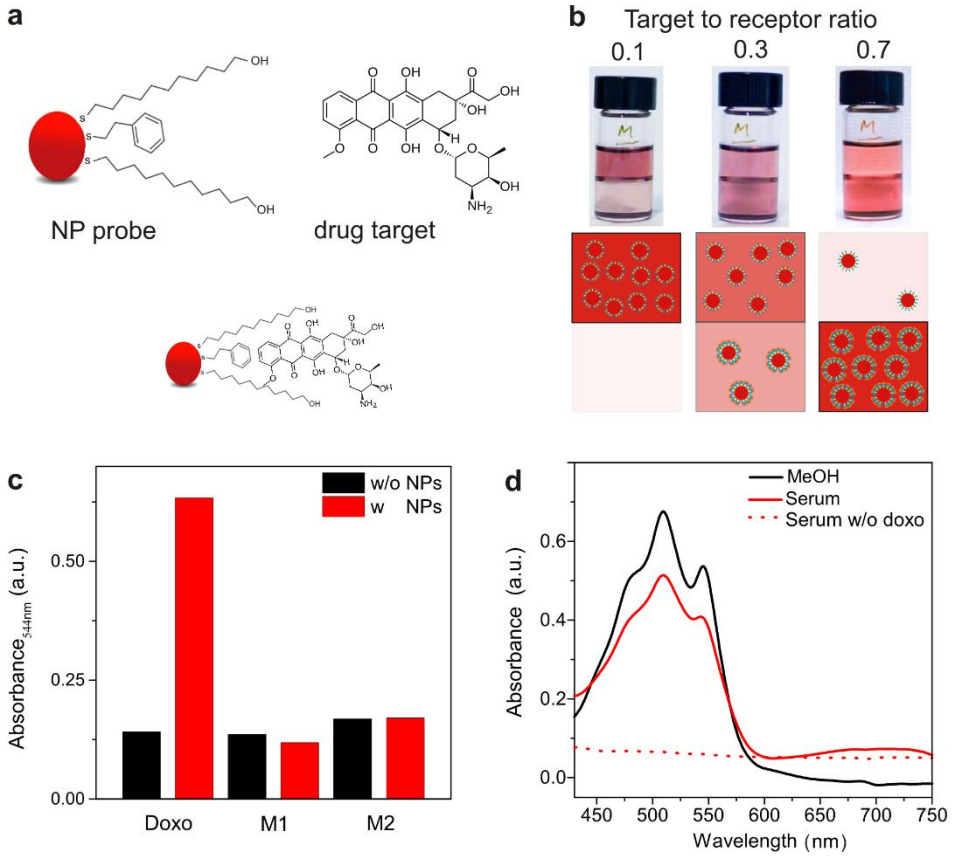

Figure 53: (a) DOXO selective gold NPs; (b) separation of DOXO in MeOH (top) and LC phase (bottom); (c) selectivity for DOXO loaded NPs in LC; (d) NP-DOXO absorbance after extraction from MeOH and from serum in UV-Vis spectroscopy. [*Courtesy of Prof. Stefan Guldin of University College London]*

Having this in mind and as a part of a collaboration with the group of prof. Stefan Guldin (Department of Chemical Engineering, University College London, London), we studied by means of molecular calculations different gold nanoparticles (4 nm in diameter) covered by a mixture of 1-hexadecane thiols (hereafter named as C16) and pyridine/4-ethylpyridine thiols (named Py/EPy, respectively) (Figure 54) in a ratio of C16: Py/EPy 1:1 to be used as a carrier for DOXO.

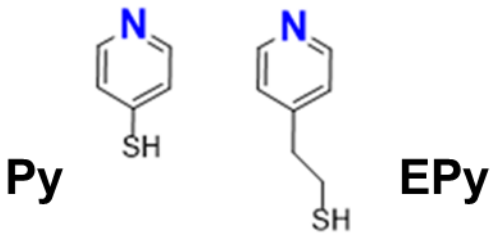

Figure 54: chemical structure of Py and EPy thiols.

The aim of this investigation was twofold. First, we would like to predict if and how the two mixtures (C16/Py and C16/EPy) of ligands phase-separate on the gold surface and which was the molecular 3D organization of the chains in the monolayer. This could be achieved by simulating the spontaneous self-assembly of the ligands via Dissipative Particle Dynamics as done before for other blends of functional thiols. Second, once the mesoscale structures were obtained, we were interested in studying their ability to bind DOXO (and its analog for comparison) through molecular recognition mechanisms. This was done by converting the corresponding coarse-grained structures into atomistic models and studying the interaction event via molecular dynamics calculations.

5.2.1 Computational details

5.2.1.1 Dissipative Particle Dynamics details

The spontaneous assembling process of the ligands on the gold surface was investigated by means of Dissipative Particle Dynamics (DPD). The set of nanoparticles considered for this study was simulated following the procedure described in Section 3.1.1. Accordingly, we will report here only the parameters pertaining to these specific systems. The initial structure of the NP core was constructed by arranging DPD beads (Au) on a *fcc* lattice into the desired icosahedral shape and diameter. Each ligand was represented by a flexible chain model of beads connected by harmonic springs of composition reported in Table 12. Solvent (methanol) was modelled as a single bead.

Ligand type	*Model*
C16	$S(C)_8$
PEy	$SCP(B)_3$
Py	$S(B)_3$

Table 12: Coarse-grained model of each ligand considered in the study

As described above, DPD pair-pair interaction parameters and ligand topology were derived using a multiscale simulation protocol, combining atomistic and coarse-grained simulation. (191-195)

Therefore, we employed the following values for a_{ij}: $a_{B\text{-}B}$ = 60.0, $a_{B\text{-}S}$ = 72.0, $a_{B\text{-}M}$ = 52.8, $a_{C\text{-}B}$ = 58.3, $a_{C\text{-}C}$ = 55.5, $a_{C\text{-}S}$ = 72.0, $a_{C\text{-}M}$ = 60.1, $a_{M\text{-}M}$ = 51.6, $a_{S\text{-}S}$ = 51.6, $a_{S\text{-}M}$ = 80.0, $a_{B\text{-}B}$ = 60.0, $a_{B\text{-}S}$ = 72.0, $a_{B\text{-}M}$ = 52.8, $a_{C\text{-}B}$ = 58.3, $a_{C\text{-}C}$ = 55.5, aC-$_{CP}$ = 53.3, $a_{C\text{-}S}$ = 72.0, $a_{C\text{-}M}$ = 60.1, $a_{CP\text{-}B}$ = 55.2, $a_{CP\text{-}CP}$ = 54.6, $a_{CP\text{-}S}$ = 72.0, $a_{CP\text{-}M}$ = 56.4, $a_{M\text{-}M}$ = 51.6, $a_{S\text{-}S}$ = 51.6, $a_{S\text{-}M}$ = 80.0 r_C/k_BT.

A 19r_C X 19r_C X 19r_C simulation box was adopted, placing the monolayer protected NP in the middle of the periodic cell. Optimized adimensional values for bond and angle parameters were employed for both alkane and perfluorocarbon thiols: k_b(B-S) = 40, r_0(B-S) = 0.39, k_θ(B-B-S) = 40, θ_0 (B-B-S) = 110, k_b(B-B) = 40, r_0 (B-B) = 0.49, k_θ(B-B-B) = 40, θ_0 (B-B-B) = 60, k_b(CP-S) = 40, r_0(CP-S) = 0.39, k_θ(B-CP-S) = 40, θ_0 (B-CP-S) = 110, k_b(B-B) = 40, r_0 (B-B) = 0.49, k_θ(B-B-B) = 40, θ_0 (B-B-B) = 60, k_b(B-CP) = 40, r_0 (B-CP) = 0.39, k_θ(B-B-CP) = 40, θ_0 (B-B-CP) = 150.

Each initial configuration was first equilibrated for 1x10^4 steps and a time step of $\Delta t=0.01\tau$. Then, additional 8x10^6 time steps (Δt = 0.02) were performed increasing the interaction parameters till their actual value.

5.2.1.2 Atomistic molecular dynamics details

Once equilibrated, the CG-NP structures were mapped back to all-atom (AA) configurations to gain insights into molecular-level details of ligand and shell properties. The monolayers were equilibrated in explicit Methanol at room temperature. All systems were minimized by 1000 steps of Steeped Descent followed by 3000 steps of Conjugated Gradient algorithms. The temperature was then raised to 300 K in 20 ps of NVT molecular dynamics (MD) simulation (Langevin thermostat, time step of 1 fs, collision frequency 1.0), followed by the equilibration of the density for 10 ns with a Berendsen barostat (pressure relaxation time of 2 ps, time step of 2 fs). At the end, we switched to a Monte Carlo barostat and performed data collection for a total of 20 ns. AA simulations were performed by means of AMBER 14 suite of software (196), employing gaff2 (197, 198) forcefield. The molecule of doxorubicin was modelled, as previously done for the crystal violet, with the R.E.D tool.

We loaded the C16/EPy AuNPs with 40 molecules of doxorubicin to evaluate which was the maximum payload for these nanoparticles (as done before in the CV case). The computational results pointed out that at the value of 40 these NPs are able to carry on their surface 40 molecules as max.

Then we performed the energetical analysis (using the MMPBSA procedure) for each system. For the entropy evaluation the &nmode calculation was used, which is unique to the normal mode calculations used to approximate vibrational entropies, while to evaluate the enthalpic components the &pb calculation was used. The &pb is unique to Poisson Boltzmann calculation.

5.2.1.3 Results

Simulations pointed out a stripe-like organization either in presence of Py and EPy, more defined in the EPy-case then in the Py-case as shown in Figure 55. This also proves the sensibility of the CG model adopted since the two ligands (Py and EPy) are different only for one chain bead. Since the patterning appeared more defined and the domains more separated in the C16/EPy mixture we chose it for further investigations.

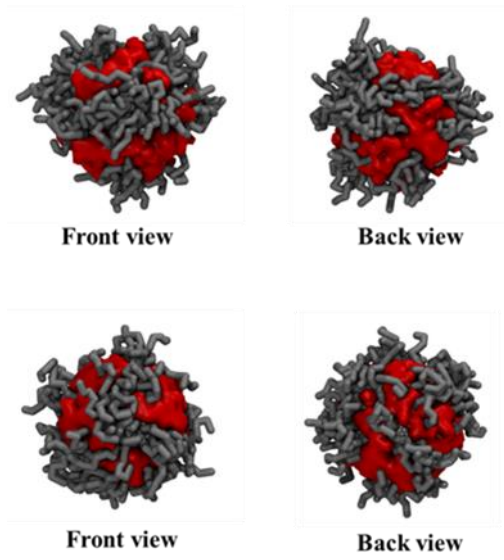

Figure 55: Equilibrated snapshots of 1:1 C16-EPy (top) and C16/Py (bottom) AuNPs. Simulations were performed in methanol, which is not shown for clarity. For each system a front and side view are shown. EPy is shown as surface to enhance the visibility of the domains. C16 ligand (grey) and EPy (red).

In principle, a random organization of the ligand is suitable for binding DOXO due to the ability of creating a larger number of binding site than a stripe-like morphology. To address if different nanostructures of the SAM could influence the interaction of DOXO with AuNPs, we converted the DPD structure of the C16/EPy into an atomistic model and compared its binding ability to a AuNP covered with a random 1:1 mixture of the same ligands.

To set up an environment closest to the experimental conditions the AA models were created using a 1:40 AuNP:DOXO ratio (Figure 56). Moreover, to evaluate the molecular recognition ability of these AuNPs, the binding of these nanoparticles with Dunorubicinone, an analogous of the Doxorubicin, (hereafter named as DOXI) was analyzed.

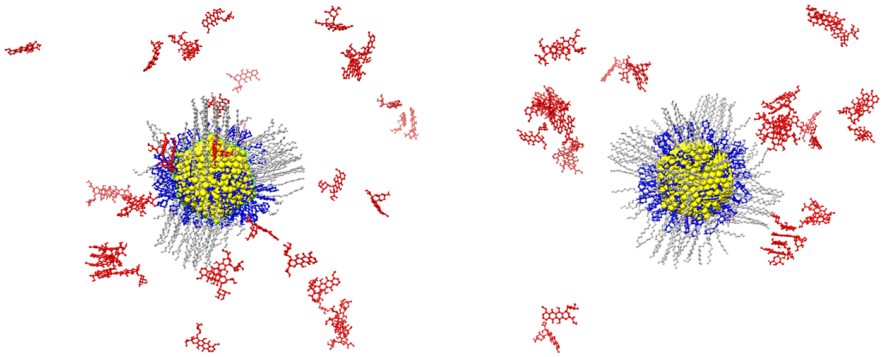

Figure 56: 1:40 AuNP:DOXO Striped (left panel) and Random (right panel) systems. Solvent was not shown for clarity.

The table below reports the number of DOXO and DOXI molecules able to bind the AuNP.

	Stripe	Random
DOXO	9/40	3/40
DOXI	15/40	12/40

Table 13: number of DOXO and DOXI molecules able to bind the AuNP.

From the data, it appears that the SAM morphology may influence the binding of small molecules on mixed monolayers. If we consider the DOXO molecule for instance, we see that a striped morphology can accommodate up to 9 DOXO molecules and the interaction involves mainly the EPy ligands (Figure 57). At the same time, the same ligands but with a random organization are less effective in capturing the drug molecules from solution and the number of DOXO bound decreases to 3. This also holds considering the second analyte, but with a lower difference between the two nanostructures. The major difference between the analytes considered is the absence of the sugar ring in the lateral chain of DOXI. This makes the molecules much less bulky. It is clear that the recognition process depends both on the nanoscale morphology and the chemical nature of the analyte, with the combination of the two.

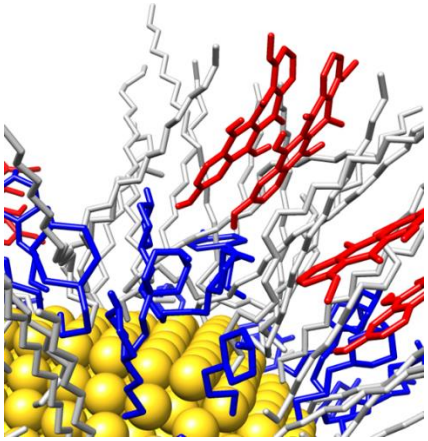

Figure 57: example of the binding of DOXI to the striped NP.

As previously done for the AuNPs carrying the crystal violet dye, we performed an energetical analysis (Figure 48, Figure 50) of the binding event to understand if the presence of a nanostructured morphology affects the affinity of DOXO and its analogues towards the monolayer. The averaged data are reported in Figure 58.

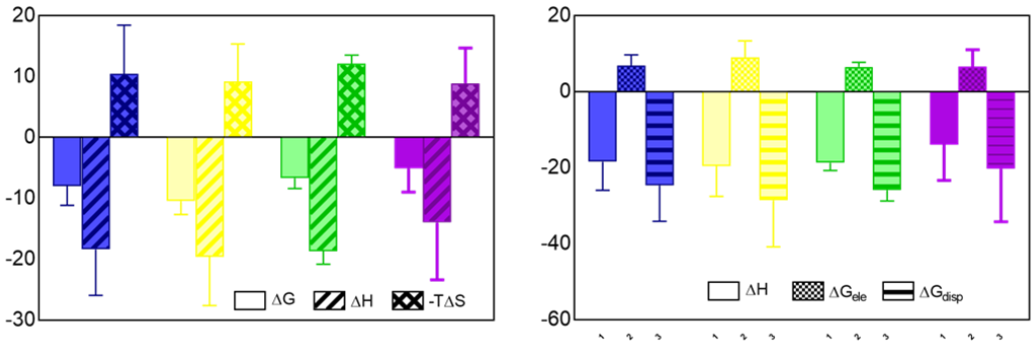

Figure 58: DOXO/DOXI-averaged MM/PBSA binding energies (kcal/mol) for the highest payload systems. Free energy of binding (ΔG), and enthalpic (ΔH) and entropic (-TΔS) terms (left panel). Electrostatic and hydrophobic contribution to the enthalpy binding component (right) panel). Data are averaged on the number of DOXO/DOXI molecules. Color legend: striped-AuNP in complex with DOXI (blue) and DOXO (yellow), Random-AuNP in complex with DOXI (green) and DOXO (violet).

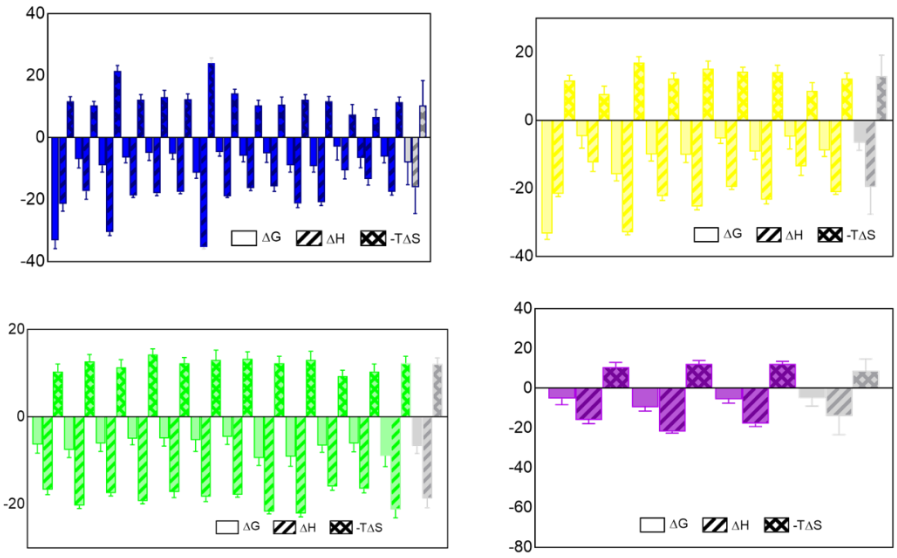

Figure 59: Main components (ΔG, ΔH, ΔS) of the free energy of binding for the systems. The values relative to each DOXO/DOXI bound (full bars) together with the average values (light grey shaded bars). Color legend: striped-AuNP in complex with DOXI (blue) and DOXO (yellow), Random-AuNP in complex with DOXI (green) and DOXO (violet).

Based on these evidences (Figure 59, Figure 58), it seems that the binding may be not cooperative as the main energetic parameters almost lay in the same range and we could take the average values as representative for all the systems. The same behavior could be observed when isolating the enthalpic term (Figure 60).

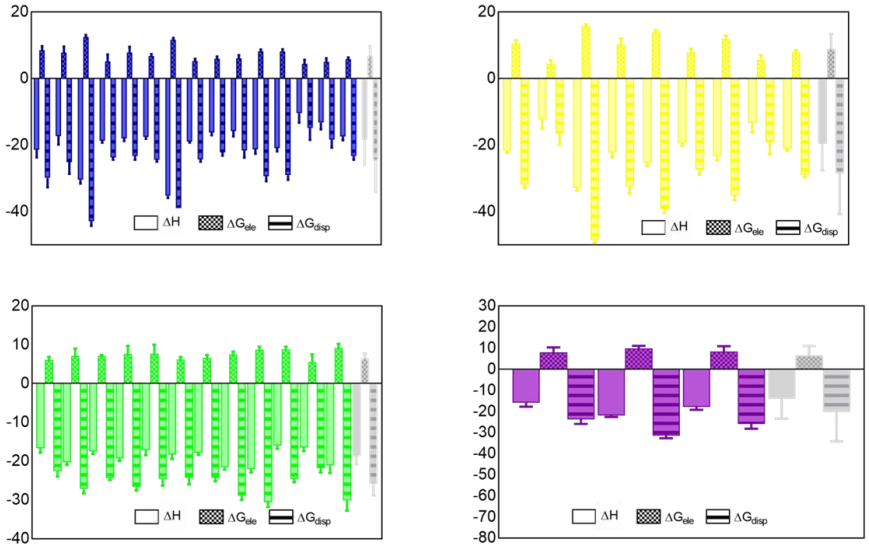

Figure 60: 40 DOXO/DOXI systems MM/PBSA binding energies (kcal/mol) of each bounded DOXO/DOXI molecule together with the average values. The values relative to each CV bounded (full bars) together with the average values (white shaded bars). Striped-AuNP bonded with DOXI (blue), with DOXO (yellow), Random-AuNP bonded with DOXI (green), with DOXO (violet).

As done before for the CV systems, we also evaluated the binding of DOXO and DOXI in terms of total and averaged number of contacts for each bound molecules) (Table 14).

	Stripe_doxo	Stripe_doxi	Random_doxo	Random_doxi
Total contacts	23	41	21	38
Averaged contacts	3	3	7	3

Table 14: Total and averaged number of contacts (contact distance 5Å) between DOXO/DOXI and C16/PEy ligands.

Molecules are considered bonded if they are able to stay attached to the NP surface (5 Å cut off distance) for at least 20 ns. From this analysis turns out that the Random-DOXO complex made the highest number of contact per molecule, 7, with respect to the other systems which made 3 contacts per molecule. This is probably due to the different steric hindrance of the molecule that allows the contact with an increased number of ligand. These data should not be misleading. The energetical analysis show that both systems loading the Dunorubicinone present the higher affinity (ΔG = -7.9 and Δ = -6.7 for Striped and Random in complex with DOXI respectively) for the binding, notwithstanding the low averaged number of contacts per molecule.

The binding analysis of small molecules demonstrate again how important are both the SAM nanostructure, present on the nanoparticle surface, and the chemical properties of the loading. Remembering that we can tune the SAM in order to improve the molecular recognition of specific biomolecules, we think that this is only one of the steps in the right direction to understand more and more details regarding how engineered nanoparticles can be used in such field like drug delivery and nanomedicine in general.

Chapter 6. *Secondary projects*

6.1 9-Aminoacridine-based agents impair the bovine viral diarrhea virus

The Bovine Viral Diarrhea is a highly contagious infectious disease that affects cattle. The causative agent is a single-stranded RNA virus (bovine viral diarrhea virus or BVDV) which belongs to the *Pestivirus* genus. This virus is responsible for a range of clinical manifestations including abortion, teratogenesis, respiratory problems. Despite the accessibility to vaccines against BVDV and the implementation of massive eradication or control programs, this virus still constitute a serious, agronomical burden.

With the aim of improving the activity of anti-*Pestivirus* agents, in the present work three prototypes – namely compounds **AVR15**, **AVR17** and **AVR26** have been selected to explore some chemical additional features based on the 9-aminoacridine scaffold (Figure 61).

Together with this three lead compounds 18 novel derivatives were synthesized and tested for anti-BVDV activity in cell-based assays. (266)

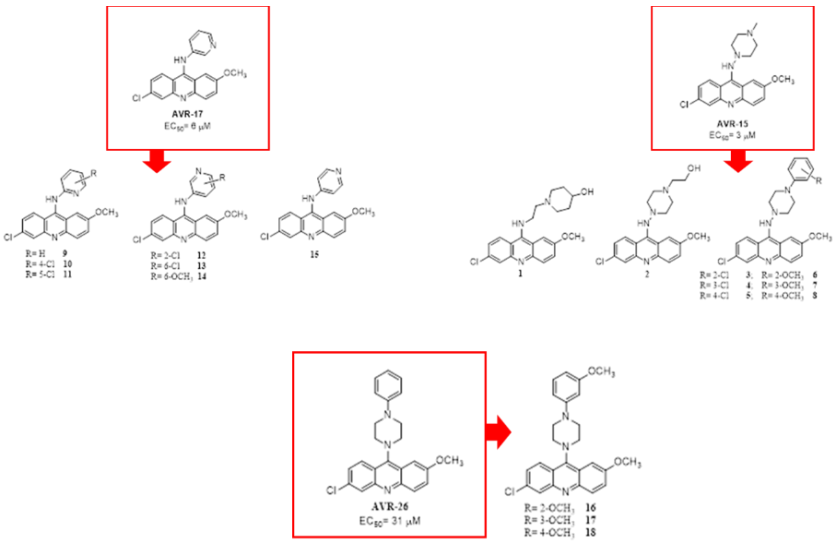

Figure 61: of the novel 9-aminoacridine-based derivatives investigated in the present work.

All the compounds were evaluated for antiviral activity and sixteen out of twenty-one compounds (76%) proved to selectively inhibit BVDV replication.

Cpd	BVDV EC_{50} (μM) [b]	MDBK CC_{50} (μM)[c]	SI[c] CC_{50}/EC_{50}
AVR15	3.0	>100	>33.3
1	11.5	>100	>8.7
2	0.80	9.2	11.5
3	7.5	>100	>13.3
4	>100	>100	-
5	68	68	1
6	2.9	46	15.9
7	35	54	1.5
8	11.9	43	3.6
AVR17	6	>100	>16.7
9	34	34	1
10	38	>100	>2.6
11[e]	10.3	100	9.7
12[e]	>100	>100	-
13	8	80	10
14	1.2	40	33.3
15	63	>100	1.6
AVR26	31	>100	>3.2
16	20.2	>100	>5.0
17	59	>100	1.7
18	75	75	1
2'-C-metilguanosine	1.7	>100	>58.8
Ribavirin	8.0	>100	>12.5

Figure 62: Compounds that reached (green) and surpass (red) the safety profile of Ribavirin (blue).

The most active compounds exhibited against BVDV an EC50 range from 0.8 to 11.5 μM and interestingly, the most promising compounds reached (in green) or surpassed (in red) the potency and the safety profile of Ribavirin (in blue), see Figure 62; especially compound 2 and 14 show the best EC50 values (Figure 63).

Cpd	BVDV EC_{50} (μM) [b]	MDBK CC_{50} (μM)[c]	SI[c] CC_{50}/EC_{50}
AVR15	3.0	>100	>33.3
1	11.5	>100	>8.7
2	0.80	9.2	11.5
3	7.5	>100	>13.3
4	>100	>100	-
5	68	68	1
6	2.9	46	15.9
7	35	54	1.5
8	11.9	43	3.6
AVR17	6	>100	>16.7
9	34	34	1
10	38	>100	>2.6
11[c]	10.3	100	9.7
12[c]	>100	>100	-
13	8	80	10
14	1.2	40	33.3
15	63	>100	1.6
AVR26	31	>100	>3.2
16	20.2	>100	>5.0
17	59	>100	1.7
18	75	75	1
2'-C-metilguanosine	1.7	>100	>58.8
Ribavirin	8.0	>100	>12.5

Figure 63: Antiviral activity against BVDV and cytotoxicity of the three prototypes (AVR) and of new 9-aminocridine derivatives 1–18. b) Compound concentration (μM) required to achieve 50% protection of MDBK cells from the BVDV-induced cytopathogenicity, as determined by the MTT method. c) Compound concentration (μM) required to reduce the viability of mock-infected MDBK cells by 50%, as determined by the MTT method. d) SI= selectivity index.

Since the RNA-dependent RNA-polymerase plays a critical role in viral replication we decided to investigate whether our newly synthesized 9-aminoacridine derivatives were able to act as inhibitor of this viral enzyme. A set of 6 compounds (i.e., **AVR15**, **2**, **6**, **AVR17**, **14**, and **AVR26**) was selected and four out of six demonstrated potent inhibition of the BVDV RdRp. These data (Figure 64) support the hypothesis that this new series of 9-aminoacridine derivatives target the BVDV replication.

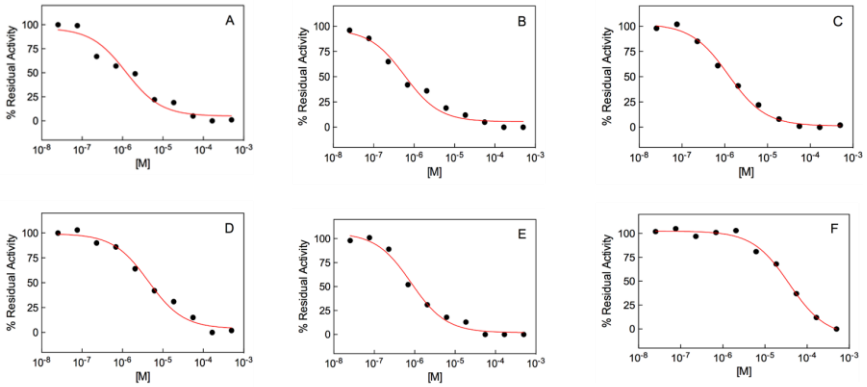

Cpd	IC_{50} (µM)
AVR15 (A)	1.2
2 (B)	0.62
6 (C)	0.88

Cpd	IC_{50}(µM)
AVR17 (D)	4.3
14 (E)	0.81
AVR26 (F)	38

Figure 64: In vitro BVDV RdRp inhibition by selected new 9-aminoacridine derivatives. All experiments were run in triplicate. Errors on IC_{50} are within 15%.

To investigate the binding mode of all compounds against the viral BVDV RdRp, thermodynamic studies were performed using isothermal titration calorimetry (ITC). The dissociation constant (K_d) and the enthalpy (ΔH_b) were calculated directly from the ITC measurement, while the binding free energy (ΔG_b) and the entropy ($-T\Delta S_b$) were calculated indirectly knowing enthalpy and the dissociation constant. ITC measurements on each compound are listed in Figure 65, while Figure 66 showed some representative ITC results, for the same 6 compounds previously selected. (266)

Cpd	K_d (μM)	ΔG_b (kcal/mol)	ΔH_b (kcal/mol)	$-T\Delta S_b$ (kcal/mol)	*n* (-)
AVR15	0.91	-8.24	-11.26	3.02	0.92
1	9.1	-6.88	-13.84	6.96	1.10
2	0.57	-8.52	-14.07	5.55	1.03
3	4.8	-7.26	-12.46	5.20	0.98
4	38	-6.03	-10.43	4.40	1.00
5	41	-5.99	-10.37	4.38	1.04
6	0.95	-8.22	-13.52	5.30	0.95
7	23	-6.33	-11.96	5.63	0.99
8	8.6	-6.91	-13.15	6.24	0.93
AVR17	0.98	-8.20	-11.94	3.74	1.03
9	15	-6.58	-10.21	3.63	1.01
10	21	-6.38	-10.15	3.77	0.98
11	18	-6.48	-10.09	3.61	0.96
12	44	-5.45	-8.87	3.42	0.90
13	1.8	-7.84	-11.53	3.69	0.92
14	0.72	-8.38	-12.39	4.01	1.05
15	31	-6.15	-9.87	3.72	0.89
AVR26	28	-6.21	-11.42	5.21	1.08
16	22	-6.36	-11.76	5.40	1.11
17	39	-6.02	-11.00	4.98	0.99
18	48	-5.89	-10.78	4.89	0.91

Figure 65: ITC determined thermodynamic data of all synthesized 9-aminoacridine derivatives binding to the BVDV RdRp. $DG_b = DH_b\_TDS_b$. $DG_b = RT \ln K_d$. n = number of binding site. All experiments were run in triplicate. Errors on DH_b are within 5%.

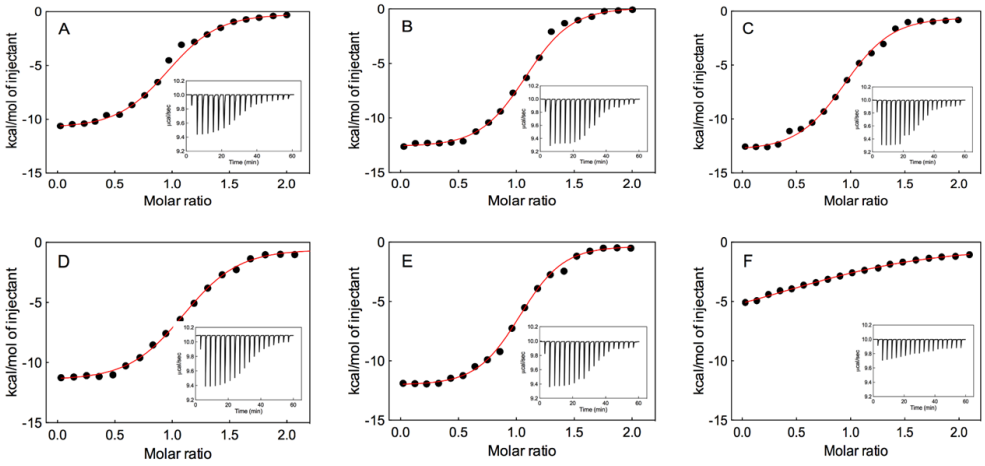

Figure 66: Representative ITC binding isotherms for AVR15 (A), 2 (B), 6 (C), AVR17 (D), 14 (E), and AVR26 (F) titrations into BVDV RdRp solutions. Inserts: ITC raw data.

The binding affinity of all compounds in complex with the BVDV RdRp could also be measured by molecular modeling. $\Delta G_{b,comp}$ values could be correlated with their experimental counterpart and they were in excellent agreement with the corresponding ITC-data, see Figure 67 (left panel). (266)

In Figure 67 (right panel) an example of computational protein-ligand binding in a box of water and ions.

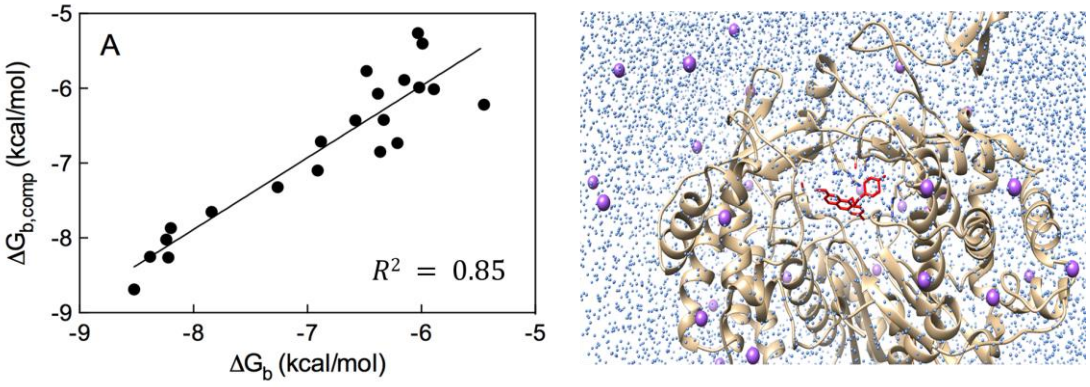

Figure 67: Correlation between computational and ITC-derived free energy of binding for all new 9-aminoacridine derivatives in complex with the BVDV RdRp (left panel). Example of one of the compound bonded to the BVDV (right panel). Ions (violet balls), water (light blue).

In order to understand how these novel compounds bind to BVDV RdRp, binding affinities have been evaluated by studying the corresponding molecular dynamics trajectories.

We have reported in this work the evaluation of the three compounds exhibiting the highest affinity, but the same evaluation has been carried out on all the most promising compounds.

Starting with the most potent compound 2, the inspection of the trajectory revealed that this molecule is able to bind the BVDV RdRp through the engagement of a bifurcated hydrogen bond (HB) between the –NH group and the side chains of E265 and R285, as shown in Figure 68. Another permanent HB is also detected between the methoxy substituent on the acridine scaffold and the ammonium group of K26. Lastly, a third HB between the hydroxyethyl group of 2 and the positively charged side chain of K525 further stabilize the protein/ligand complex. (266)

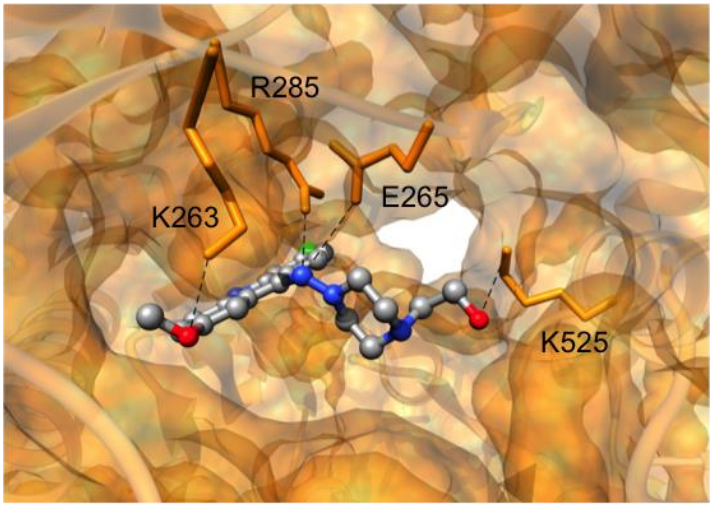

Figure 68: Equilibrated snapshots of compounds 2 in complex with the BVDV RdRp. The protein is portrayed as a transparent orange ribbon, together with its van der Waals surface. Compounds are shown as atom-colored sticks-and-balls (C, gray; N, blue; O, red; Cl, green). Hydrogen atoms, water molecules, ions and counterions are omitted for clarity.

The inspection of the trajectory of compound 3 showed that besides the same two stabilizing HBs, was engaged in a favorable π-cation interaction was detected between the ortho-chlorine and the positively charged side chain of R529 (Figure 69). In summary, the position of the Cl atom contributed in orienting the molecule within the binding pocket. (266)

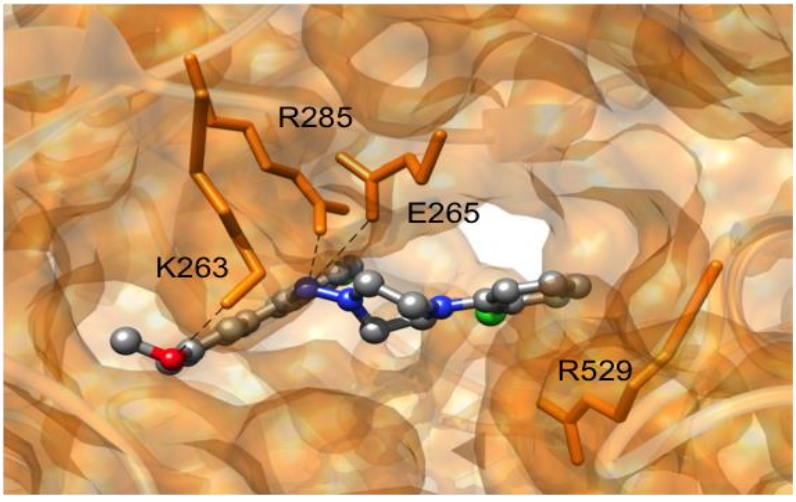

Figure 69: Equilibrated snapshots of compounds 3 in complex with the BVDV RdRp. The protein is portrayed as a transparent orange ribbon, together with its van der Waals surface. Compounds are shown as atom-colored sticks-and-balls (C, gray; N, blue; O, red; Cl, green). Hydrogen atoms, water molecules, ions and counterions are omitted for clarity.

Compound 8, with a metoxy group at the *para* position, not able to perform the π -cation interaction described for 3, is involved in a further HB interaction between its metoxy substituent and the same residue R529 (Figure 70).

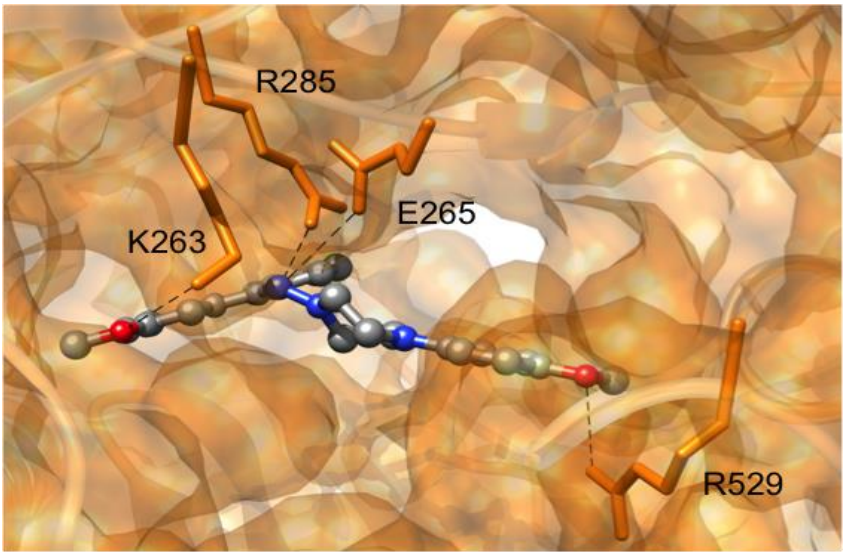

Figure 70: Equilibrated snapshots of compounds 8 in complex with the BVDV RdRp. The protein is portrayed as a transparent orange ribbon, together with its van der Waals surface. Compounds are shown as atom-colored sticks-and-balls (C, gray; N, blue; O, red; Cl, green). Hydrogen atoms, water molecules, ions and counterions are omitted for clarity.

Conclusion

The analysis of different sets of mixed-monolayer NPs obtained by using mixtures of immiscible hydrogenated and fluorinated ligands, PEGylated ligands, mixtures of anionic and fluorinated ligands and zwitterionic and fluorinated thiols offered a unique background for understanding the formation of specific patterns once ligands self-assemble but also for developing some rules to tune the monolayer nanostructure. From these evaluations, we assessed that if our fluorinated thiols have the same chain length, the NP presents a phase-separated morphology; when there is a mismatch of ligands length, the overall SAM organization exhibited stripe-like domains or patches and if branched ligands are employed the phase-segregation is disfavored and a random organization is promoted. Although we obtained these design principles from simple models, they present a general validity and are currently employed by our group to synthesize and characterize more complex nanoparticles. Then, investigating the role of different nanostructured SAM protected NPs in the interaction with lipid bilayers, cells and proteins, we discovered a dissimilar behavior due to the ligand composition and structure of the SAM, in particular stripe-like domains acted differently from the homoligand and Janus systems, when interacting with lipids and cells. From our computational simulations we assessed that the different affinities depend both on the molecular characteristic and organization of the shell that allow a different number and type of ligands to be involved in the interaction with the membrane. At cellular level the dissimilar behavior of differently patterned nanoparticles, found during the *in-silico* evaluation, was observed also in terms of a different time/concentration dependent internalization capacity. These results demonstrate how a smart choice of the mixture of ligands employed, together with a precise pattern of the SAM, is a potential strategy to tune the interaction of nanoparticles with membranes.

Moreover, nanomaterials with precise surface organization can be tailored to selectively interact with other objects in a specific manner. During a three months collaboration in the group of Prof. Stefan Guldin (University College of London), we investigated at the molecular level how the crystal violet (CV), a powerful antimicrobial and antibacterial dye swell-encapsulated in polyurethane employed in some British pilot-hospital to coat surfaces, interact with homoligand MUS-SAM protected gold nanoparticles. The evaluation took into account three different pH and the relative protonation states of the CV elucidating the role

of the energy components in driving the binding. Another example of supramolecular binding of small molecules have been evaluated. In this case the binding of Doxorubicin and its analogues to mixed SAM protected gold NPs have been considered with the aim of using these NPs as a carrier for the chemotherapeutical drug. Different SAM morphologies were considered to understand how different nanostructures can influence the ability of NPs to target specific molecules.

References

[1] Blanco E, Shen H, Ferrari M (2015) Principles of nanoparticle design for overcoming biological barriers to drug delivery. Nat Biotech 33:941–951

[2] Chen R, Riviere JE (2016) Biological and environmental surface interactions of nanomaterials: characterization, modeling, and prediction. Wiley Interdiscip Rev Nanomed Nanobiotechnol 9:1440

[3] Chou LYT, Ming K, Chan WCW (2011) Strategies for the intracellular delivery of nanoparticles. Chem Soc Rev 40:233–245

[4] Mahon E, Salvati A, Baldelli Bombelli F, Lynch I, Dawson KA (2012) Designing the nanoparticle-biomolecule interface for "targeting and therapeutic delivery". J Control Release 161:164–174

[5] Ryu JH, Lee S, Son S, Kim SH, Leary JF, Choi K, Kwon IC (2014) Theranostic nanoparticles for future personalized medicine. J Controlled Release 190:477–484

[6] Wolfram J, Shen H, Ferrari M (2015) Multistage vector (MSV) therapeutics. J Controlled Release 219:406–415

[7] Whitesides, G. M. The "Right" Size in Nanobiotechnology. Nat. Biotechnol. 2003, 21, 1161−5.

[8] Variola, F.; Vetrone, F.; Richert, L.; Jedrzejowski, P.; Yi, J.-H.; Zalzal, S.; Clair, S.; Sarkissian, A.; Perepichka, D. F.; Wuest, J. D.; et al. Improving Biocompatibility of Implantable Metals by Nanoscale Modification of Surfaces: An Overview of Strategies, Fabrication Methods, and Challenges. Small 2009, 5, 996−1006.

[9] Ruoslahti, E.; Bhatia, S. N.; Sailor, M. J. Targeting of Drugs and Nanoparticles to Tumors. J. Cell Biol. 2010, 188, 759−68.

[10] Dhar, S.; Liu, Z.; Thomale, J.; Dai, H.; Lippard, S. J. Targeted Single-Wall Carbon Nanotube-Mediated Pt(IV) Prodrug Delivery Using Folate as a Homing Device. J. Am. Chem. Soc. 2008, 130, 11467−76.

[11] Xie, J.; Chen, K.; Lee, H.-Y.; Xu, C.; Hsu, A. R.; Peng, S.; Chen, X.; Sun, S. Ultrasmall c(RGDyK)-Coated Fe3O4 Nanoparticles and Their Specific Targeting to Integrin αvβ3-rich Tumor Cells. J. Am. Chem. Soc. 2008, 130, 7542−3.

[12] Poon, Z.; Chen, S.; Engler, A. C.; Lee, H.; Atas, E.; von Maltzahn, G.; Bhatia, S. N.; Hammond, P. T. Ligand-Clustered "Patchy" Nanoparticles for

Modulated Cellular Uptake and in vivo Tumor Targeting. Angew. Chem., Int. Ed. Engl. 2010, 49, 7266−7270.

[13] Panyam, J. Biodegradable Nanoparticles for Drug and Gene Delivery to Cells and Tissue. Adv. Drug Delivery Rev. 2003, 55, 329−347.

[14] Goldberg, M. S.; Xing, D.; Ren, Y.; Orsulic, S.; Bhatia, S. N.; Sharp, P. A. Nanoparticle-Mediated Delivery of siRNA Targeting Parp1 Extends Survival of Mice Bearing Tumors Derived from Brca1-Deficient Ovarian Cancer Cells. Proc. Natl. Acad. Sci. U.S.A. 2011, 108, 745−50.

[15] Duncan, B.; Kim, C.; Rotello, V. M. Gold Nanoparticle Platforms as Drug and Biomacromolecule Delivery Systems. J. Controlled Release 2010, 148, 122−7.

[16] Kim, D.; Park, S.; Lee, J. H.; Jeong, Y. Y.; Jon, S. Antibiofouling Polymer-Coated Gold Nanoparticles as a Contrast Agent for in vivo Xray Computed Tomography Imaging. J. Am. Chem. Soc. 2007, 129, 7661−5.

[17] Park, J.-H.; Gu, L.; von Maltzahn, G.; Ruoslahti, E.; Bhatia, S. N.; Sailor, M. J. Biodegradable Luminescent Porous Silicon Nanoparticles for in vivo Applications. Nat. Mater. 2009, 8, 331−6.

[18] Von Maltzahn, G.; Park, J.-H.; Agrawal, A.; Bandaru, N. K.; Das, S. K.; Sailor, M. J.; Bhatia, S. N. Computationally Guided Photothermal Tumor Therapy Using Long-Circulating Gold Nanorod Antennas. Cancer Res. 2009, 69, 3892−900.

[19] Murphy, C. J.; Gole, A. M.; Stone, J. W.; Sisco, P. N.; Alkilany, A. M.; Goldsmith, E. C.; Baxter, S. C. Gold Nanoparticles in Biology: Beyond Toxicity to Cellular Imaging. Acc. Chem. Res. 2008, 41, 1721− 30.

[20] Webster, T. J.; Ergun, C.; Doremus, R. H.; Siegel, R. W.; Bizios, R. Specific Proteins Mediate Enhanced Osteoblast Adhesion on Nanophase Ceramics. J. Biomed. Mater. Res. 2000, 51, 475−83.

[21] Shang, W.; Nuffer, J. H.; Muñiz-Papandrea, V. A.; Colón, W.; Siegel, R. W.; Dordick, J. S. Cytochrome C on Silica Nanoparticles: Influence of Nanoparticle Size on Protein Structure, Stability, and Activity. Small 2009, 5, 470−6.

[22] Linse, S.; Cabaleiro-Lago, C.; Xue, W.-F.; Lynch, I.; Lindman, S.; Thulin, E.; Radford, S. E.; Dawson, K. A. Nucleation of Protein Fibrillation by Nanoparticles. Proc. Natl. Acad. Sci. U.S.A. 2007, 104, 8691−6.

[23] Casals, E.; Pfaller, T.; Duschl, A.; Oostingh, G. J.; Puntes, V. Time Evolution of the Nanoparticle Protein Corona. ACS Nano 2010, 4, 3623−32.

[24] Lynch, I.; Dawson, K. A.; Linse, S. Detecting Cryptic Epitopes Created by Nanoparticles. Science 2006, 327, 14−20

[25] Goldberg, M. S.; Xing, D.; Ren, Y.; Orsulic, S.; Bhatia, S. N.; Sharp, P. A. Nanoparticle-Mediated Delivery of siRNA Targeting Parp1 Extends Survival of Mice Bearing Tumors Derived from Brca1-Deficient Ovarian Cancer Cells. Proc. Natl. Acad. Sci. U.S.A. 2011, 108, 745−50.

[26] Duncan, B.; Kim, C.; Rotello, V. M. Gold Nanoparticle Platforms as Drug and Biomacromolecule Delivery Systems. J. Controlled Release 2010, 148, 122−7.

[27] Kim, D.; Park, S.; Lee, J. H.; Jeong, Y. Y.; Jon, S. Antibiofouling Polymer-Coated Gold Nanoparticles as a Contrast Agent for in vivo Xray Computed Tomography Imaging. J. Am. Chem. Soc. 2007, 129, 7661−5

[28] Marco P. Monopoli *et al.* Biomolecular coronas provide the biological identity of nanosized materials, *Nature nanotechnology* 7, (2012).

[29] Cedervall, T. *et al.* Understanding the nanoparticle–protein corona using methods to quantify exchange rates and affinities of proteins for nanoparticles. *Proc. Natl Acad. Sci. USA* 104, 2050–2055 (2007).

[30] Nel, A. E. *et al.* Understanding biophysicochemical interactions at the nano–bio interface. *Nature Mater.* 8, 543–557 (2009).

[31] Lynch, I. & Dawson, K. A. Protein–nanoparticle interactions. *Nano Today* 3, 40–47 (2008).

[32] Aggarwal, P., Hall, J. B., McLeland, C. B., Dobrovolskaia, M. A. & McNeil, S. E. Nanoparticle interaction with plasma proteins as it relates to particle biodistribution, biocompatibility and therapeutic efficacy. *Adv. Drug Deliv. Rev.* 61, 428–437 (2009).

[33] Tenzer, S. *et al.* Nanoparticle size is a critical physicochemical determinant of the human blood plasma corona: a comprehensive quantitative proteomic analysis. *ACS Nano* 5, 7155–7167 (2011).

[34] Ge, C. *et al.* Binding of blood proteins to carbon nanotubes reduces cytotoxicity. *Proc. Natl Acad. Sci. USA* 108, 16968–16973 (2011).

[35] Ang, J. C., Lin, J-M., Yaron, P. N. & White, J. W. Protein trapping of silica nanoparticles. *Soft* Matter 6, 383–390 (2010).

[36] Jennifer E et al. Engineering nanomaterials for biomedical applications requires understanding the nano-bio interface: a perspective. J. Phy. Chem. Lett., 2012, 3, 3149-3158

[37] Blanque, R.; Meakin, C.; Millet, S.; Gardner, C. R. Gen. Pharmac. **1998,** 31, 301-306

[38] Boisselier, E.; Astruc, D. Chem. Soc. Rev. **2009,** 38, 1759-1782

[39] Ying Jiang; Engineering the nano-bio interface of gold nanoparticles for biomedical applications. 2016, Doctoral Dissertation

[40] Fang S-B, Tseng WY, Lee H-C, Tsai C-K, Huang J-T, Hou S-Y. J.Microbial. Meth. 2009;77: 225–228

[41] Nam JM, Park SJ, Mirkin CA. J. Am. Chem. Soc. 2002; 124:3820–3821.

[42] Yi-Cheun Yeh, Brian Creran, Vincent M. Rotello, Article Gold Nanoparticles_Preparations, Properties, And Applications In Bionanotechnology, Nanoscale. 2012, 4(6): 1871-1880

[43] Nam JM, Thaxton CS, Mirkin CA. Science. 2003; 301:1884–1886

[44] Liu G, Mao X, Phillips JA, Xu H, Tan W, Zeng L. Anal. Chem. 2009; 81:10013–10018

[45] Bunz UHF, Rotello VM. Angew. Chem. Int. Edit. 2010; 49:3268–3279.

[46] VM, Prakash YS, Mukherjee P. Nano Lett. 2010; 10:2543–25

[47] Verma A, Uzun O, Hu Y, Hu Y, Han H-S, Watson N, Chen S, Irvine andF, Stellacci DJ. Nat. Mater. 2008; 7:588–595

[48] Rosi NL, Giljohann DA, Thaxton CS, Lytton-Jean AKR, Han MS, Mirkin CA. Science. 2006; 312:1027–1030

[49] Ghosh PS, Kim C-K, Han G, Forbes NS, Rotello VM. ACS Nano. 2008; 2:2213–2218

[50] Alric C, Taleb J, Le Duc G, Mandon C, Billotey C, Le Meur-Herland A, Brochard T, Vocanson F, Janier M, Perriat P, Roux S, Tillement O. J. Am. Chem.Soc. 2008; 130:5908–5915

[51] Popovtzer R, Agrawal A, Kotov NA, Popovtzer A, Balter J, Carey TE, Kopelman R. Nano Lett. 2008; 8:4593–4596

[52] Love JC1, Estroff LA, Kriebel JK, Nuzzo RG, Whitesides GM, Self-assembled monolayers of thiolates on metals as a form of nanotechnology, *Chem Rev.*, 2005 Apr;105(4):1103-69

[53] Abraham Ulman, Formation and Structure of Self-Assembled Monolayers, Chem. Rev., 1996; 96(4): 1533-1554

[54] Daniel K Schwartz, Mechanisms and Kinetics of Self-Assembled Monolayer Formation, Annu. Rev. Phys. Chem, 2001; 52: 107-37

[55] Colin D. Bain, George M. Whitesides, Molecular-Level Control over Surface Order in Self-Assembled Monolayer Films of Thiols on Gold, science 1988 Apr; 240: 62-63

[56] Ghorai and Sharon C. Glotzer Atomistic Simulation Study of Striped Phase Separation in Mixed-Ligand Self-Assembled Monolayer Coated Nanoparticles, *J. Phys. Chem*. C 2010, 114, 19182–19187;

[57] Jackson, A. M.; Myerson, J. W.; Stellacci, F. Spontaneous Assembly of Subnanometre-Ordered Domains in the Ligand Shell of Monolayer-Protected Nanoparticles. *Nature Mater.* 2004, *3*, 330-336

[58] Sing, C.; Ghorai, P. K.; Horsch, M. A.; Jackson, A. M.; Larson, R. G.; Stellacci, F.; Glotzer, S. C. Entropy-Mediated Patterning of Surfactant-Coated Nanoparticles and Surfaces. *Phys. Rev. Lett.* 2007, *99*, 226106

[59] Heikkilä E, Martinez-Seara H, Gurtovenko AA, Javanainen M, Häkkinen H, Vattulainen I, Akola J (2014) Cationic Au nanoparticle binding with plasma membrane-like lipid bilayers: potential mechanism for spontaneous permeation to cells revealed by atomistic simulations. J Phys Chem C 118:11131–11141

[60] P. Pengo, M. Sologan, L. Pasquato, F. Guida, S. Pacor, A. Tossi, F. Stellacci, D. Marson, S. Boccardo, S. Pricl, P. Posocco, Gold nanoparticles with patterned surface monolayers for nanomedicine: current perspectives", EBJ **2017**

[61] Jackson AM; Hu Y; Silva PJ; Stellacci F, From Homoligand to Mixed Ligand monolayer protected metal nanoparticles: a scanning tunneling microscopy investigation, J Am Chem Soc. 2006; 128(34): 11135-49

[62] Pons-Siepermann IC, Glotzer SC (2012a) Design of patchy particles using quaternary self-assembled monolayers. ACS Nano 6:3919–3924

[63] Pons-Siepermann IC, Glotzer SC (2012b) Design of patchy particles using ternary self-assembled monolayers. Soft Matter 8:6226

[64] Jackson AM, Myerson JW, Stellacci F (2004) Spontaneous assembly of sub-nanometer-ordered domains in the ligand shell of monolayer protected nanoparticles. Nat Mater 3:330–336

[65] Singh Ghorai, P. K.; Horsch, M. A.; Jackson, A. M.; Larson, R. G.; Stellacci, F.; Glotzer, S. C. Entropy-Mediated Patterning of Surfactant-Coated Nanoparticles and Surfaces. *Phys. Rev. Lett.* 2007, *99*, 226106

[66] Carney RP, DeVries GA, Dubois C, Kim H, Jin YK, Singh C, Ghorai PK, Tracy JB, Stiles RL, Murray RW, Glotzer SC, Stellacci F (2008) Size limitations for the formation of ordered striped nanoparticles. J Am Chem Soc 130:798–799

[67] DeVries GA, Brunnbauer M, Hu Y, Jackson AM, Long B, Neltner BT, Uzun O, Wunsch BH, Stellacci F (2007) Divalent metal nanoparticles. Science 315:358

[68] Devries GA, Talley FR, Carney RP, Stellacci F (2008) Thermodynamic study of the reactivity of the two topological point defects present in mixed self-assembled monolayers on gold nanoparticles. Adv Mater 20:4243–4247 Ding HM, Ma YQ (2012) Interactions between Janus particles and membranes. Nanoscale 4:1116–1122

[69] Kim H, Carney RP, Reguera J, Ong QK, Liu X, Stellacci F (2012) Synthesis and characterization of Janus gold nanoparticles. Adv Mater 24:3857–3863

[70] Ge X, Ke PC, Davis TP, Ding F (2015) A thermodynamics model for the emergence of a stripe-like binary SAM on a nanoparticle surface. Small 11:4894–4899

[71] Gentilini, C.; Franchi, P.; Mileo, E.; Polizzi, S.; Lucarini, M.; Pasquato, L. Formation of Patches on 3D SAMs Driven by Thiols with Immiscible Chains Observed by ESR Spectroscopy. *Angew. Chem., Int. Ed.* 2009, *48*, 3060–3064

[72] Krafft MP, Riess JG (2009) Chemistry, physical chemistry, and uses of molecular fluorocarbon–hydrocarbon diblocks, triblocks, and related compounds—unique “apolar” components for self-assembled colloid and interface engineering. Chem Rev 109:1714–1792

[73] Posocco P, Gentilini C, Bidoggia S, Pace A, Franchi P, Lucarini M, Fermeglia M, Pricl S, Pasquato L (2012) Self-organization of mixtures of fluorocarbon and hydrocarbon amphiphilic thiolates on the surface of gold nanoparticles. ACS Nano 6:7243–7253

[74] Şologan, M.; Cantarutti, C.; Bidoggia, S.; Polizzi, S.; Pengo, P.; Pasquato L. Routes to the Preparation of Mixed Monolayers of Fluorinated and Hydrogenated Alkanetiolates Grafted on the Surface of Gold Nanoparticles. *Faraday Discussion* 2016, DOI: 10.1039/C6FD00016A

[75] Du J, O’Reilly RK (2011) Anisotropic particles with patchy, multicompartment and Janus architectures: preparation and application. Chem Soc Rev 40:2402–2416

[76] Reguera J, Kim H, Stellacci F (2013) Advances in Janus nanoparticles. Chimia 67:811–818

[77] Song Y, Chen S (2014) Janus nanoparticles: preparation, characterization, and applications. Chem Asian J 9:418–430

[78] Walther A, Müller AHE (2013) Janus particles: synthesis, selfassembly, physical properties, and applications. Chem Rev 113:5194–5261

[79] Ulman A (1996) Formation and structure of self-assembled monolayers. Chem Rev 96:1533–1554

[80] R. Huang, R. P. Carney, F. Stellacci and B. L. T. Lau, *Nanoscale*, 2013, 5, 6928-6935

[81] R. Huang, R. P. Carney, K. Ikuma, F. Stellacci and B. L. T. Lau, *ACS Nano*, 2014, 8, 5402-5412

[82] A. Hung, S. Mwenifumbo, M. Mager, J. J. Kuna, F. Stellacci, I. Yarovsky and M. M. Stevens, *J. Am. Chem. Soc.*, 2011, 133, 1438-1450

[83] Carney RP, Carney TM, Mueller M, Stellacci F (2012) Dynamic cellular uptake of mixed-monolayer protected nanoparticles. Biointerphases 7:17

[84] Sabella S, Carney RP, Brunetti V, Malvindi MA, Al-Juffali N, Vecchio G, Janes SM, Bakr OM, Cingolani R, Stellacci F, Pompa PP (2014) A general mechanism for intracellular toxicity of metalcontaining nanoparticles. Nanoscale 6:7052–7061

[85] Van Lehn RC, Alexander-Katz A (2015) Pathway for insertion of amphiphilic nanoparticles into defect-free lipid bilayers from atomistic molecular dynamics simulations. Soft Matter 11:3165–3175

[86] R. C. Van Lehn and A. Alexander-Katz, *J. Phys. Chem. C*, 2013, 117, 20104-20115

[87] A. Verma, O. Uzun, Y. Hu, Y. Hu, H. S. Han, N. Watson, S. Chen, D. J. Irvine and F. Stellacci, *Nat. Mater.*, 2008, 7, 588-595

[88] Anderluh G, Beseničar M, Kladnik A, Lakey JH, Maček P (2005) Properties of nonfused liposomes immobilized on an L1 Biacore chip and their permeabilization by a eukaryotic pore-forming toxin. Anal Biochem 344:43–52

[89] Beseničar M, Maček P, Lakey JH, Anderluh G (2006) Surface plasmon resonance in protein–membrane interactions. Chem Phys Lipids 141:169–178

[90] Lelimousin M, Limongelli V, Sansom MSP (2016) Conformational changes in the epidermal growth factor receptor: role of the transmembrane domain

investigated by coarse-grained metadynamics free energy calculations. J Am Chem Soc 138:10611–10622

[91] Saunders MG, Voth GA (2013) Coarse-graining methods for computational biology. Annu Rev Biophys 42:73–93

[92] G. Rossi and L. Monticelli, *Biochim. Biophys. Acta*, 2016, 1858, 2380-2389

[93] Elani Y, Purushothaman S, Booth PJ, Seddon JM, Brooks NJ, Law RV, Ces O (2015) Measurements of the effect of membrane asymmetry on the mechanical properties of lipid bilayers. Chem Commun 51:6976–6979

[94] Fadeel B, Xue D (2009) The ins and outs of phospholipid asymmetry in the plasma membrane: roles in health and disease. Crit Rev Biochem Mol Biol 44:264–277

[95] H. M. Ding and Y. Q. Ma, *Nanoscale*, 2012, **4**, 1116-1122

[96] P. Gkeka, L. Sarkisov and P. Angelikopoulos, *J. Phys. Chem. Lett.*, 2013, 4, 1907-1912

[97] Ji QJ, Yuan B, Lu XM, Yang K, Ma YQ (2016) Controlling the nanoscale rotational behaviors of nanoparticles on the cell membranes: a computational model. Small 12:1140–1146

[98] Van Lehn RC, Alexander-Katz A (2013) Structure of mixed-monolayer-protected nanoparticles in aqueous salt solution from atomistic molecular dynamics simulations. J Phys Chem C 117:20104–20115

[99] Carney RP, Carney TM, Mueller M, Stellacci F (2012) Dynamic cellular uptake of mixed-monolayer protected nanoparticles. Biointerphases 7:17

[100] S. Sabella, R. P. Carney, V. Brunetti, M. A. Malvindi, N. Al-Juffali, G. Vecchio, S. M. Janes, O. M. Bakr, R. Cingolani, F. Stellacci and P. P. Pompa, *Nanoscale*, 2014, 6, 7052-7061

[101] Verma, A.; Uzun, O.; Hu, Y.; Hu, Y.; Han, H.S.; Watson, N.; Vhen, S.; Irvine D. J.; Stellacci, F. Surface-Structure-Regulated Cell-Membrane Penetration by Monolayer-Protected Nanoparticles. *Nature Mater.* 2008, *7*, 588-595

[102] Li Y, Li X, Li Z, Gao H (2012) Surface-structure-regulated penetration of nanoparticles across a cell membrane. Nanoscale 4:3768–3775

[103] Van Lehn RC, Alexander-Katz A (2015) Pathway for insertion of amphiphilic nanoparticles into defect-free lipid bilayers from atomistic molecular dynamics simulations. Soft Matter 11:3165–3175

[104] R. C. Van Lehn, M. Ricci, P. H. Silva, P. Andreozzi, J. Reguera, K. Voitchovsky, F. Stellacci and A. Alexander-Katz, *Nat. Commun.*, 2014, 5, 4482-4493;

[105] Van Lehn RC, Atukorale PU, Carney RP, Yang YS, Stellacci F, Irvine DJ, Alexander-Katz A (2013) Effect of particle diameter and surface composition on the spontaneous fusion of monolayerprotected gold nanoparticles with lipid bilayers. Nano Lett 13:4060–4067

[106] Heikkilä E, Martinez-Seara H, Gurtovenko AA, Javanainen M, Häkkinen H, Vattulainen I, Akola J (2014) Cationic Au nanoparticle binding with plasma membrane-like lipid bilayers: potential mechanism for spontaneous permeation to cells revealed by atomistic simulations. J Phys Chem C 118:11131–11141

[107] Jiaqi L, Hongwu Z, Zhen C, Yonggang Z (2010) Penetration of lipid membranes by gold nanoparticles: insights into cellular uptake, cytotoxicity, and their relationship. ACS Nano 4:5421–5429

[108] Monopoli MP, Aberg C, Salvati A, Dawson KA (2012) Biomolecular coronas provide the biological identity of nanosized materials. Nat Nanotechnol 7:779–786

[109] Walkey CD, Chan WC (2012) Understanding and controlling the interaction of nanomaterials with proteins in a physiological environment. Chem Soc Rev 41:2780–2799

[110] Docter D, Westmeier D, Markiewicz M, Stolte S, Knauer SK, Stauber RH (2015) The nanoparticle biomolecule corona: Lessons learned—challenge accepted? Chem Soc Rev 44:6094–6121

[111] Setyawati MI, Tay CY, Docter D, Stauber RH, Leong DT (2015) Understanding and exploiting nanoparticles' intimacy with the blood vessel and blood. Chem Soc Rev 44:8174–8199

[112] Mahmoudi M, Lynch I, Ejtehadi MR, Monopoli MP, Bombelli FB, Laurent S (2011) Protein–nanoparticle interactions: opportunities and challenges. Chem Rev 111:5610–5637

[113] Schick I, Lorenz S, Gehrig D, Tenzer S, Storck W, Fischer K, Strand D, Laquai F, Tremel W (2014) Inorganic Janus particles for biomedical applications. Beilstein J Nanotechnol 5:2346–2362

[114] Chen P, Seabrook SA, Epa VC, Kurabayashi K, Barnard AS, Winkler DA, Kirby JK, Ke PC (2014) Contrasting effects of nanoparticle binding on protein denaturation. J Phys Chem C 118:22069–22078

[115] Kim ST, Saha K, Kim C, Rotello VM (2013) The role of surface functionality in determining nanoparticle cytotoxicity. Acc Chem Res 46:681–691

[116] Kopp M, Kollenda S, Epple M (2017) Nanoparticle–protein interactions: therapeutic approaches and supramolecular chemistry. Acc Chem Res 50:1383–1390

[117] Saptarshi SR, Duschl A, Lopata AL (2013) Interaction of nanoparticles with proteins: relation to bio-reactivity of the nanoparticle. J Nanobiotechnol 11:26

[118] Wang X, Wang M, Lei R, Zhu SF, Zhao Y, Chen C (2017) Chiral surface of nanoparticles determines the orientation of adsorbed transferrin and its interaction with receptors. ACS Nano 11:4606–4616

[119] Albanese A, Tang PS, Chan WC (2012) The effect of nanoparticle size, shape, and surface chemistry on biological systems. Annu Rev Biomed Eng 14:1–16

[120] Tenzer S, Docter D, Kuharev J, Musyanovych A, Fetz V, Hecht R, Schlenk F, Fischer D, Kiouptsi K, Reinhardt C, Landfester K, Schild H, Maskos M, Knauer SK, Stauber RH (2013) Rapid formation of plasma protein corona critically affects nanoparticle pathophysiology. Nat Nanotechnol 8:772–781

[121] Walczyk D, Bombelli FB, Monopoli MP, Lynch I, Dawson KA (2010) What the cell "sees" in bionanoscience. J Am Chem Soc 132:5761–5768

[122] Walkey CD, Chan WC (2012) Understanding and controlling the interaction of nanomaterials with proteins in a physiological environment. Chem Soc Rev 41:2780–2799

[123] Pino Pd, Pelaz B, Zhang Q, Maffre P, Nienhaus GU, Parak WJ (2014) Protein corona formation around nanoparticles—from the past to the future. Mater Horiz 1:301–313

[124] Huang, R.; Carney, R. P.; Ikuma, K.; Stellacci, F.; Lau B. L. T. Effects of Surface Compositional and Structural Heterogeneity on Nanoparticle–Protein Interactions: Different Protein Configurations. *ACS Nano* 2014, *8*, 5402-5412

[125] Hung A, Mwenifumbo S, Mager M, Kuna JJ, Stellacci F, Yarovsky I, Stevens MM (2011) Ordering surfaces on the nanoscale: implications for protein adsorption. J Am Chem Soc 133:1438–1450

[126] A. Hung, M. Mager, M. Hembury, F. Stellacci, M. M. Stevens and I. Yarovsky, *Chem. Sci.*, 2013, 4, 928-937

[127] Frohlich E (2012) The role of surface charge in cellular uptake and cytotoxicity of medical nanoparticles. Int J Nanomed 7:5577–5591

[128] S. Sabella, R. P. Carney, V. Brunetti, M. A. Malvindi, N. Al-Juffali, G. Vecchio, S. M. Janes, O. M. Bakr, R. Cingolani, F. Stellacci and P. P. Pompa, *Nanoscale*, 2014, 6, 7052-7061

[129] Fratoddi I, Venditti I, Cametti C, Russo MV (2015) How toxic are gold nanoparticles? The state-of-the-art. Nano Res 8:1771–1799

[130] Henriksen-Lacey M, Carregal-Romero S, Liz-Marzán LM (2017) Current challenges toward in vitro cellular validation of inorganic nanoparticles. Bioconjug Chem 28:212–221

[131] Treuel L, Jiang X, Nienhaus GU (2013) New views on cellular uptake and trafficking of manufactured nanoparticles. J R Soc Interface 10:20120939

[132] Carney RP, Carney TM, Mueller M, Stellacci F (2012) Dynamic cellular uptake of mixed-monolayer protected nanoparticles. Biointerphases 7:17

[133] Gong N, Chen S, Jin S, Zhang J, Wang PC, Liang XJ (2015) Effects of the physicochemical properties of gold nanostructures on cellular internalization. Regen Biomater 2:273–280

[134] Mukhopadhyay A, Grabinski C, Afrooz AR, Saleh NB, Hussain S (2012) Effect of gold nanosphere surface chemistry on protein adsorption and cell uptake in vitro. Appl Biochem Biotechnol 167:327–337

[135] Saha K, Kim ST, Yan B, Miranda OR, Alfonso FS, Shlosman D, Rotello VM (2013) Surface functionality of nanoparticles determines cellular uptake mechanisms in mammalian cells. Small 9:300–305

[136] Oh E, Delehanty JB, Sapsford KE, Susumu K, Goswami R, Blanco-Canosa JB, Dawson PE, Granek J, Shoff M, Zhang Q, Goering PL, Huston A, Medintz IL (2011) Cellular uptake and fate of PEGylated gold nanoparticles is dependent on both cell-penetration peptides and particle size. ACS Nano 5:6434–6448

[137] Ritz S, Schöttler S, Kotman N, Baier G, Musyanovych A, Kuharev J, Landfester K, Schild H, Jahn O, Tenzer S, Mailänder V (2015) Protein corona of nanoparticles: distinct proteins regulate the cellular uptake. Biomacromolecules 16:1311–1321

[138] P. U. Atukorale, Y. S. Yang, A. Bekdemir, R. P. Carney, P. J. Silva, N. Watson, F. Stellacci and D. J. Irvine, *Nanoscale*, 2015, 7, 11420-11432

[139] Yang YSS, Atukorale PU, Moynihan KD, Bekdemir A, Rakhra K, Tang L, Stellacci F, Irvine DJ (2017) High-throughput quantitation of inorganic nanoparticle biodistribution at the single-cell level using mass cytometry. Nat Commun 8:14069

[140] Y. S. Yang, R. P. Carney, F. Stellacci and D. J. Irvine, *ACS Nano*, 2014, 8, 8992-9002

[141] Boccardo Silvia, B-RAF Mutations in melanoma: Translational approach to Vemurafenib therapy response, 2015, Master degree

[142] Siewert J. Marrink*[†], H. Jelger Risselada[†], Serge Yefimov[‡], D. Peter Tieleman[§], and Alex H. de Vries "The MARTINI Force Field: Coarse Grained Model for Biomolecular Simulations, . *Phys. Chem. B*, 2007, *111* (27), pp 7812–7824

[143] Maria Millsa and Ioan Andricioaei, An experimentally guided umbrella sampling protocol for biomolecules, *J. Chem. Phys*. 129, 114101, 2008

[144] Groot, R. D.; Warren, P. B. Dissipative Particle Dynamics: Bridging the Gap between Atomistic and Mesoscopic Simulation. *J. Chem. Phys.* **1997**, *107*, 4423-4435

[145] Posel, Z.; Posocco, P.; Lisal, M.; Fermeglia, M.; Pricl, S. Highly Grafted Polystyrene/Polyvinylpyridine Polymer Gold Nanoparticles in a Good Solvent: Effects of Chain Length and Composition. *Soft Matter* **2016**

[146] Walker, M.; Masters, A. J.; Wilson, M. R. Self-Assembly and Mesophase Formation in a Non-Ionic Chromonic Liquid Crystal System: Insights from Dissipative Particle Dynamics Simulations. *Phys. Chem. Chem. Phys.* **2014**, *16*, 23074-23081

[147] Vishnyakov, A.; Lee, M.-T.; Neimark, A. V. Prediction of the Critical Micelle Concentration of Nonionic Surfactants by Dissipative Particle Dynamics Simulations. *J. Phys. Chem. Lett.* **2013**, *4*, 797-802

[148] Berezkin, A. V.; Kudryavtsev, Y. V. Simulation of End-Coupling Reactions at a Polymer−Polymer Interface: The Mechanism of Interfacial Roughness Development. *Macromolecules* **2011**, *44*, 112-121

[149] Singh, C.; Ghorai, P. K.; Horsch, M. A.; Jackson, A. M.; Larson, R. G.; Stellacci, F.; Glotzer, S. C. Entropy-Mediated Patterning of Surfactant-Coated Nanoparticles and Surfaces. *Phys. Rev. Lett.* **2007**, *99* 226106

[150] Groot, R. D.; Warren, P. B. Dissipative Particle Dynamics: Bridging the Gap between Atomistic and Mesoscopic Simulation. *J. Chem. Phys.* **1997**, *107*, 4423-4435

[151] Plimpton, S. Fast Parallel Algorithms for Short-Range Molecular Dynamics. *J. Comput. Phys.* **1995**, *117*, 1-19

[152] Şologan M, Marson D, Polizzi S, Pengo P, Boccardo S, Pricl S, Posocco P, Pasquato L (2016b) Patchy and Janus nanoparticles by self-organization of mixtures of fluorinated and hydrogenated alkanethiolates on the surface of a gold core. ACS Nano 10:9316–9325

[153] M. Şologan, M. Boccalon, S. Bidoggia, C. Gentilini, L. Pasquato, P. Pengo Self-Sorting in Mixed Fluorinated/Hydrogenated Assemblies J. Supramol. Chem. 2017, 29, 808-822

[154] Krafft, M. P. Fluorocarbons and fluorinated amphiphiles in drug delivery and biomedical research. *Adv. Drug. Deliv. Rev.* 47, 209–228 (2001);

[155] Riess, J. G. Highly fluorinated amphiphilic molecules and self-assemblies with biomedical Potential. Curr. Opin. Colloid Interface Sci. 14, 294–304 (2009);

[156] Zhenjing Zhang et al. The fluorination effect of fluoroamphiphiles in cytosolic protein delivery. Nature Commun. (2018) 9:1377

[157] M. E. Kurczy, Z.-J. Zhu, J. Ivanisevic, A. M. Schyler, K. Lalwani, A. F. Santidrian, J. M. David, A. Giddabasappa, A. J. Roberts, H. J. Olivos *et al. Nature Commun.* 2015, *6*, 5998

[158] Shimizu T., Teranishi T., Hasegawa S., Miyake M. Size Evolution of Alkanethiol-Protected Gold Nanoparticles by Heat Treatment in the Solid State. *J. Phys. Chem*. B 2003, 107, 2719-2724

[159] Xiang Liu et al. Determination of monolayer-protected gold nanoparticle ligand-shell morphology using NMR, Nature Communications, 2012, 3, 1182

[160] Gezelter, J. D., *et al.* OPENMD, an Open Source Engine for Molecular Dynamics. Available at http://openmd.net.

[161] Fleury, B.; Cortes-Huerto, R.; Taché, O.; Testard, F.; Menguy, N.; Spalla, O. Gold Nanoparticle Internal Structure and Symmetry Probed by Unified Small-

Angle X-Ray Scattering and X-Ray Diffraction Coupled with Molecular Dynamics Analysis. *Nano Lett.* **2015**, *15*, 6088-6094

[162] Posocco, P.; Gentilini, C.; Bidoggia, S.; Pace, A.; Franchi, P.; Lucarini, M.; Fermeglia, M.; Pricl, S.; Pasquato, L. Self-Organization of Mixtures of Fluorocarbon and Hydrocarbon Amphiphilic Thiolates on the Surface of Gold Nanoparticles. *ACS Nano* **2012**, *6*, 7243-7253

[163] Sun, H.; Mumby, S. J.; Maple, J. R.; Hagler, A. T. An Ab Initio Cff93 All-Atom Force Field for Polycarbonates. *J. Am. Chem. Soc.* **1994**, *116*, 2978-2987

[164] Scocchi, G.; Posocco, P.; Danani, A.; Pricl, S.; Fermeglia, M. To the Nanoscale, and Beyond! Multiscale Molecular Modeling of Polymer-Clay Nanocomposites. *Fluid Phase Equilib.* **2007**, *261*, 366-374

[165] Theodorou, D. N.; Suter, U. W. Atomistic Modeling of Mechanical Properties of Polymeric Glasses. *Macromolecules* **1986**, *19*, 139-154.

[166] Fermeglia, M.; Ferrone, M.; Pricl, S. Computer Simulation of Nylon-6/Organoclay Nanocomposites: Prediction of the Binding Energy. *Fluid Phase Equilib.* **2003**, *212*, 315-329

[167] Majumder, C.; Briere, T. M.; Mizuseki, H.; Kawazoe, Y. Structural Investigation of Thiophene Thiol Adsorption on Au Nanoclusters: Influence of Back Bonds. *J. Phys. Chem. Lett.* **2002**, *117*, 2819-2822

[168] Heinz, H.; Lin, T.-J.; Kishore Mishra, R.; Emami, F. S. Thermodynamically Consistent Force Fields for the Assembly of Inorganic, Organic, and Biological Nanostructures: The Interface Force Field. *Langmuir* **2013**, *29*, 1754-1765

[169] Toukmaji, A.; Sagui, C.; Board, J.; Darden, T. Efficient Particle-Mesh Ewald Based Approach to Fixed and Induced Dipolar Interactions. *J. Chem. Phys.* **2000**, *113*, 10913-10927

[170] Scocchi, G.; Posocco, P.; Fermeglia, M.; Pricl, S. Polymer−Clay Nanocomposites: A Multiscale Molecular Modeling Approach. *J. Phys. Chem. B* **2007**, *111*, 2143-2151

[171] Goel, H.; Chandran, P. R.; Mitra, K.; Majumdar, S.; Ray, P. Estimation of Interfacial Tension for Immiscible and Partially Miscible Liquid Systems by Dissipative Particle Dynamics. *Chem. Phys. Lett.* **2014**, *600*, 62-67

[172] Martínez, L.; Andrade, R.; Birgin, E. G.; Martnez, J. M. Packmol: A Package for Building Initial Configurations for Molecular Dynamics Simulations. *J. Comput. Chem.* **2009**, *30*, 2157−2164

[173] Plimpton, S. Fast Parallel Algorithms for Short-Range Molecular Dynamics. *J. Comput. Phys.* **1995**, *117*, 1-19

[174] Humphrey, W.; Dalke, A.; Schulten, K. VMD: Visual Molecular Dynamics. *J. Mol. Graphics* **1996**, *14*, 33-38

[175] Zhou, Y.; Marson, R. L.; van Anders, G.; Zhu, J.; Ma, G.; Ercius, P.; Sun, K.; Yeom, B.; Glotzer, S. C.; Kotov, N. A. Biomimetic Hierarchical Assembly of Helical Supraparticles from Chiral Nanoparticles. *ACS Nano* 2016, *10*, 3248−3256.

[176] Liu, X.; Wu, F.; Tian, Y.; Wu, M.; Zhou, Q.; Jiang, S.; Niu, Z. Size Dependent Cellular Uptake of Rod-like Bionanoparticles with Different Aspect Ratios *Scientific Reports* 2016, *6*, 24567

[177] Dag, A.; Zhao, J.; Stenzel, M. H. Origami with ABC Triblock Terpolymers Based on Glycopolymers: Creation of Virus-Like Morphologies. *ACS Macro Lett.* 2015, *4*, 579−583

[178] Huang, R.; Carney, R. P.; Ikuma, K.; Stellacci, F.; Lau B. L. T. Effects of Surface Compositional and Structural Heterogeneity on Nanoparticle–Protein Interactions: Different Protein Configurations. *ACS Nano* 2014, *8*, 5402-5412.

[179] Li, Z.-W.; Zhu, Y.-L.; Lu, Z.-Y.; Sun, Z.-Y. A Versatile Model for Soft Patchy Particles with Various Patch Arrangements. *Soft Matter* 2016, *12*, 741-749

[180] Gentilini, C.; Pasquato, L. Morphology of Mixed-Monolayers Protecting Metal Nanoparticles. *J. Mater. Chem.* 2010, *20*, 1403-1412

[181] Jackson, A. M.; Myerson, J. W.; Stellacci, F. Spontaneous Assembly of Subnanometre-Ordered Domains in the Ligand Shell of Monolayer-Protected Nanoparticles. *Nature Mater.* 2004, *3*, 330-336

[182] Jackson, A. M.; Hu, Y.; Silva, P. J.; Stellacci, F. From Homoligand- to Mixed-Ligand- Monolayer-Protected Metal Nanoparticles: A Scanning Tunneling Microscopy Investigation. *J. Am. Chem. Soc.* 2006, *128*, 11135-11149

[183] Sing, C.; Ghorai, P. K.; Horsch, M. A.; Jackson, A. M.; Larson, R. G.; Stellacci, F.; Glotzer, S. C. Entropy-Mediated Patterning of Surfactant-Coated Nanoparticles and Surfaces. *Phys. Rev. Lett.* 2007, *99*, 226106

[184] Carney, R.P.; DeVries, G. A.; Dubois, C.; Kim, H.; Kim, J. W.; Singh, C.; Ghorai, P. K.; Tracy, J. B.; Stiles, R. L.; Murray, R. W.; Glotzer, S. C.; Stellacci, F. Size Limitations for the Formation of Ordered Striped Nanoparticles *J. Am. Chem. Soc*. 2008, *130*, 798-799

[185] Li, Z.-W.; Zhu, Y.-L.; Lu, Z.-Y.; Sun, Z.-Y. A Versatile Model for Soft Patchy Particles with Various Patch Arrangements. *Soft Matter* 2016, *12*, 741-749

[186] Verma, A.; Uzun, O.; Hu, Y.; Hu, Y.; Han, H.S.; Watson, N.; Vhen, S.; Irvine D. J.; Stellacci, F. Surface-Structure-Regulated Cell-Membrane Penetration by Monolayer-Protected Nanoparticles. *Nature Mater.* 2008, *7*, 588-595

[187] Stewart, A. ; Zheng, S.; McCourt, M. R.; Bell, S. E. J. Controlling Assembly of Mixed Thiol Monolayers on Silver Nanoparticles to Tune their Surface Properties *ACS Nano* 2012, *6*, 3718-3726

[188] Bianchi, E.; Kahl, G.; Likos, C.N.; Sciortino, F. Inverse Patchy Colloids with Small Patches: Fluid Structure and Dynamical Slowing Down. *J. Phys.: Condens. Matter* 2015, *27*, 27, 230301

[189] Harkness, K. M.; Balinski, A.; Mclean, J. A.; Clieff, D. E. Nanoscale Phase Segregation of Mixed Thiolates on Gold Nanoparticles. *Angew. Chem. Inter. Ed.* 2011, *50*, 10554 –10559

[190] PEGylation on mixed monolayer gold nanoparticles: Effect of grafting density, chain length, and surface curvature, Journal of Colloidal and Interface Science, 504 (2017) 325-333

[191] Posocco, P.; Hassan, Y. M.; Barandiaran, I.; Kortaberria, G.; Pricl, S.; Fermeglia, M. Combined Mesoscale/Experimental Study of Selective Placement of Magnetic Nanoparticles in Diblock Copolymer Films Via Solvent Vapor Annealing. *J. Phys. Chem. C* 2016, *120*, 7403-7411

[192] Posel, Z.; Posocco, P.; Lisal, M.; Fermeglia, M.; Pricl, S. Highly Grafted Polystyrene/Polyvinylpyridine Polymer Gold Nanoparticles in a Good Solvent: Effects of Chain Length and Composition. *Soft Matter* 2016, *12*, 3600-3611

[193] Posel, Z.; Posocco, P.; Fermeglia, M.; Lisal, M.; Pricl, S. Modeling Hierarchically Structured Nanoparticle/Diblock Copolymer Systems. *Soft Matter* 2013, *9*, 2936-2946

[194] Posocco, P.; Posel, Z.; Fermeglia, M.; Lísal, M.; Pricl, S. A Molecular Simulation Approach to the Prediction of the Morphology of Self-Assembled Nanoparticles in Diblock Copolymers. *J. Mater. Chem.* 2010, *20*, 10511–10520

[195] Scocchi, G.; Posocco, P.; Handgraaf, J.-W.; Fraaije, J. G. E. M.; Fermeglia, M.; Pricl, S. A Complete Multiscale Modelling Approach for Polymer–Clay Nanocomposites. *Chem. Eur. J.* 2009, *15*, 7586-7592

[196] D. A. Case, V. Babin, J. T. Berryman, R. M. Betz, Q. Cai, D. S. Cerutti, T. E. Cheatham, T. A. I. Darden, R. E. Duke, H. Gohlke, A. W. Goetz, S. Gusarov, N. Homeyer, P. Janowski, J. Kaus, I. Kolossváry, A. Kovalenko, T. S. Lee, S. LeGrand, T. Luchko, R. Luo, B. Madej, K. M. Merz, F. Paesani, D. R. Roe, A. Roitberg, C. Sagui, R. Salomon-Ferrer, G. Seabra, C. L. Simmerling, W. Smith, J. Swails, R. C. Walker, J. Wang, R. M. Wolf, X. Wu and P. A. Kollman, *AMBER 14, University of California, San Francisco*, 2014

[197] J. Wang, R. M. Wolf, J. W. Caldwell, P. A. Kollman and D. A. Case, *J. Comput. Chem.*, 2004, **25**, 1157-1174

[198] J. Wang, W. Wang, P. A. Kollman and D. A. Case, *J. Mol. Graphics Model.*, 2006, **25**, 247-260

[199] Posocco, P.; Gentilini, C.; Bidoggia, S.; Pace, A.; Franchi, P.; Lucarini, M.; Fermeglia, M.; Pricl, S.; Pasquato, L. Self-organization of Mixtures of Fluorocarbon- and Hydrocarbon Amphiphilic Thiolates on the Surface of Gold Nanoparticles. *ACS Nano* 2012, *6*, 7243-7253

[200] Ge X, Ke PC, Davis TP, Ding F (2015) A thermodynamics model for the emergence of a stripe-like binary SAM on a nanoparticle surface. Small 11:4894–4899

[201] Heikkilä E, Gurtovenko AA, Martinez-Seara H, Häkkinen H, Vattulainen I, Akola J (2012) Atomistic simulations of functional Au144(SR)60 gold nanoparticles in aqueous environment. J Phys Chem C 116:9805–9815

[202] Lane JMD, Grest GS (2010) Spontaneous asymmetry of coated spherical nanoparticles in solution and at liquid–vapor interfaces. Phys Rev Lett 104:235501

[203] Velachi V, Bhandary D, Singh JK, Cordeiro MNDS (2015) Structure of mixed self-assembled monolayers on gold nanoparticles at three different arrangements. J Phys Chem C 119:3199–3209

[204] Velachi V, Bhandary D, Singh JK, Cordeiro MNDS (2016) Striped gold nanoparticles: new insights from molecular dynamics simulations. J Chem Phys 144:244710

[205] Kuna JJ, Voïtchovsky K, Singh C, Jiang H, Mwenifumbo S, Ghorai PK, Stevens MM, Glotzer SC, Stellacci F (2009) The effect of nanometre-scale structure on interfacial energy. Nat Mater 8:837–842 Lane JMD, Grest GS (2010) Spontaneous asymmetry of coated spherical nanoparticles in solution and at liquid–vapor interfaces. Phys Rev Lett 104:235501

[206] Velachi V, Bhandary D, Singh JK, Cordeiro MNDS (2015) Structure of mixed self-assembled monolayers on gold nanoparticles at three different arrangements. J Phys Chem C 119:3199–3209

[207] Velachi V, Bhandary D, Singh JK, Cordeiro MNDS (2016) Striped gold nanoparticles: new insights from molecular dynamics simulations. J Chem Phys 144:244710

[208] Silvia Bidoggia et al. Fluorinated And Charged Hydrogenated Alkanethiolates Grafted On Gold: Expanding the Diversity of Mixed Monolayer Nanoparticles for Biological Applications, Bioconjugate Chem. 2017, 28, 43-52

[209] Shuaidong Huo et al. Fully Zwitterionic Nanoparticle Antimicrobial Agent through Tuning of Core Size and Ligand Structure, ACS Nano 2016, 10, 8732-8737

[210] Ying Jiang et al. The Interplay of Size and Surface Functionality on the Cellular Uptake of Sub-10nm Gold Nanoparticles, ACS Nano 2015, 10, 9986-9993

[211] Zheng, N.; Fan, J.; Stucky, G., *J. Am. Chem. Soc*. 2006, 198, 6550- 6551.

[212] Chen R, Riviere JE (2016) Biological and environmental surface interactions of nanomaterials: characterization, modeling, and prediction. Wiley Interdiscip Rev Nanomed Nanobiotechnol 9:e1440

[213] Lelimousin M, Limongelli V, Sansom MSP (2016) Conformational changes in the epidermal growth factor receptor: role of the transmembrane domain investigated by coarse-grained metadynamics free energy calculations. J Am Chem Soc 138:10611–10622

[214] Saunders MG, Voth GA (2013) Coarse-graining methods for computational biology. Annu Rev Biophys 42:73–93

[215] Van Lehn RC, Ricci M, Silva PH, Andreozzi P, Reguera J, Voitchovsky K, Stellacci F, Alexander-Katz A (2014) Lipid tail protrusions mediate the insertion of nanoparticles into model cell membranes. Nat Commun 5:4482–4493

[216] P. Posocco, C. Gentilini, S. Bidoggia, A. Pace, P. Franchi, M. Lucarini, M. Fermeglia, S. Pricl and L. Pasquato, *ACS Nano*, 2012, 6, 7243-7253

[217] C. Gentilini, P. Franchi, E. Mileo, S. Polizzi, M. Lucarini, L. Pasquato, *Angew. Chem. Int. Ed.* **2009**, *48*, 3060

[218] M. Sologan, C. Cantarutti, S. Bidoggia, S. Polizzi, P. Pengo and L. Pasquato, *Faraday Discuss.*, 2016, 191, 527-543

[219] M. Şologan, D. Marson, S. Polizzi, P. Pengo, S. Boccardo, S. Pricl, P. Posocco and L. Pasquato, *ACS Nano*, 2016, 10, 9316-9325

[220] G. Rossi and L. Monticelli, *Biochim. Biophys. Acta*, 2016, **1858**, 2380-2389

[221] H. I. Ingólfsson, C. Arnarez, X. Periole and S. J. Marrink, *J. Cell Sci.*, 2016, **129**, 257-268

[222] M. G. Saunders and G. A. Voth, *Annu. Rev. Biophys.*, 2013, **42**, 73-93

[223] S. J. Marrink and D. P. Tieleman, *Chem. Soc. Rev.*, 2013, **42**, 6801-6822

[224] H. Lee, A. H. de Vries, S.-J. Marrink and R. W. Pastor, *J. Phys. Chem. B*, 2009, **113**, 13186-13194

[225] M. Bulacu, N. Goga, W. Zhao, G. Rossi, L. Monticelli, X. Periole, D. P. Tieleman and S. J. Marrink, *J. Chem. Theory*, 2013, **9**, 3282-3292

[226] T. A. Wassenaar, H. I. Ingólfsson, R. A. Böckmann, D. P. Tieleman and S. J. Marrink, *J. Chem. Theory*, 2015, **11**, 2144-2155

[227] T. Fischer, H. Jelger Risselada and R. L. C. Vink, *Phys. Chem. Chem. Phys.*, 2012, **14**, 14500-14508

[228] H. J. Risselada and S. J. Marrink, *Proc. Natl. Acad. Sci.*, 2008, **105**, 17367-17372

[229] P. Pengo, S. Polizzi, L. Pasquato and P. Scrimin, *J. Am. Chem. Soc.*, 2005, 127, 1616-1617.

[230] D. H. de Jong, S. Baoukina, H. I. Ingólfsson and S. J. Marrink, *Comput. Phys. Commun.*, 2016, **199**, 1-7

[231] J. Kästner, *Wiley Interdisciplinary Reviews: Computational Molecular Science*, 2011, **1**, 932-942

[232] D. Bochicchio, E. Panizon, R. Ferrando, L. Monticelli and G. Rossi, *J. Chem. Phys.*, 2015, **143**, 144108

[233] P. Pengo, L. Baltzer, L. Pasquato and P. Scrimin, *Angew. Chem. Int. Ed.*, 2007, 46, 400-404

[234] M. De, C.-C. You, S. Srivastava and V. M. Rotello, *J. Am. Chem. Soc.*, 2007, 129, 10747-10753

[235] N. A. Kotov, *Science*, 2010, 330, 188-189

[236] C. M. Jewell, J. M. Jung, P. U. Atukorale, R. P. Carney, F. Stellacci and D. J. Irvine, *Angew. Chem. Int. Ed.*, 2011, 50, 12312-12315.

[237] Y. S. Yang, R. P. Carney, F. Stellacci and D. J. Irvine, *ACS Nano*, 2014, 8, 8992-9002

[238] E. Harrison, J. R. Nicol, M. Macias–Montero, G. A. Burke, J. A. Coulter, B. J. Meenan and D. Dixon, *Mater. Sci. Eng., C*, 2016, 62, 710-718.

[239] E. Harrison, J. A. Coulter and D. Dixon, *Nanomedicine (Lond)*, 2016, 11, 851-865N. D. Burrows, A. M. Vartanian, N. S. Abadeer, E. M. Grzincic, L. M. Jacob, W. Lin, J. Li, J. M. Dennison, J. G. Hinman and C. J. Murphy, *J. Phys. Chem. Lett.*, 2016, 7, 632-641.

[240] P. Pengo, M. Şologan, L. Pasquato, F. Guida, S. Pacor, A. Tossi, F. Stellacci, D. Marson, S. Boccardo, S. Pricl and P. Posocco, *Eur. Biophys. J.*, 2017, 46, 749-771A.

[241] Verma, O. Uzun, Y. Hu, Y. Hu, H. S. Han, N. Watson, S. Chen, D. J. Irvine and F. Stellacci, *Nat. Mater.*, 2008, 7, 588-595.

[242] Shuaidong Huo et al, Ultrasmall Gold Nanoparticles Bheavior In Vivo Modulated by Surface Polyethylene Glycol (Peg) Grafting, Bioconjugate Chem. 2107, 28, 239-243

[243] N. A. Peppas and D. E. Owens, Int. J. Pharm., 2006, 307, 93–102.

[244] K. Knop, R. Hoogenboom, D. Fischer and U. S. Schubert, Angew. Chem., Int. Ed., 2010, 49, 6288–6308.

[245] S. Stolnik, S. E. Dunn, M. C. Garnett, M. C. Davies, A. G. Coombes, D. C. Taylor, M. P. Irving, S. C. Purkiss, T. F. Tadros, S. S. Davis and L. Illum, Pharm. Res., 1994, 11, 1800–1808.

[246] T. Tagami, Y. Uehara, N. Moriyoshi, T. Ishida and H. Kiwada, J. Controlled Release, 2011, 151, 149–154.

[247] R. Konradi, B. Pidhatika, A. Muhlebach and M. Textort, Langmuir, 2008, 24, 613–616.

[248] Z. G. Estephan, J. A. Jaber and J. B. Schlenoff, Langmuir, 2010, 26, 16884–16889.

[249] Z. G. Estephan, P. S. Schlenoff and J. B. Schlenoff, Langmuir, 2011, 27, 6794–6800.

[250] W. Norde, Pure Appl. Chem., 1994, 66, 491–496.

[251] R. Hong, N. O. Fischer, A. Verma, C. M. Goodman, T. Emrick and V. M. Rotello, J. Am. Chem. Soc., 2004, 126, 739–743.

[252] P. Roach, D. Farrar and C. C. Perry, J. Am. Chem. Soc., 2006, 128, 3939–3945.

[253] M. E. Aubin-Tam and K. Hamad-Schifferli, Langmuir, 2005, 21, 12080–12084.

[254] H. D. Hill, J. E. Millstone, M. J. Banholzer and C. A. Mirkin, ACS Nano, 2009, 3, 418–424.

[255] S. H. D. Lacerda, J. J. Park, C. Meuse, D. Pristinski, M. L. Becker, A. Karim and J. F. Douglas, ACS Nano, 2010, 4, 365–379.

[256] D. H. Tsai, F. W. DelRio, A. M. Keene, K. M. Tyner, R. I. MacCuspie, T. J. Cho, M. R. Zachariah and V. A. Hackley, Langmuir, 2011, 27, 2464–2477.

[257] Yuya Tsujimoto et al. Rate-determination step in the self-assembly process of supramolecular coordination capsules, Chem Sci. 2014, 5, 4167-4272

[258] Mariana Q. Mesquita et al. Revisiting Current Photoactive Materials for Antimicrobial Photodynamic Therapy, Molecules, 2018, 23(10): 2424

[259] Thomas J. Macdonald, Thiol-Capped Gold Nanoparticles Swell Encapsulated into Polyurethane as Powerful Antibacterial Surfaces Under Dark and Light Conditions, Scientific Reports, 2016, 6, 39272

[260] Ther Drug Monit 34, 460, 2012

[261] Ther Drug Monit 33, 766, 2011

[262] Kossatz et al. Breast Cancer Research (2015) 17:66,

[263] Panoraia I Siafaka et al. Surface Modified Multifunctional and Stimuli Responsive Nanoparticles for Drug Targeting: Current Status and Uses, Int J Mol Sci. 2016, 17(9): 1440

[264] Alle Madhusudhan et al., *Int. J. Mol. Sci.* 2014, *15*(5), 8216-8234;

[265] Madhusudhan A et al. Efficient pH dependent drug delivery to target cancer cells by gold nanoparticles capped with carboxymethyl chitosan, Int J Mol Sci, 2014, 15(5):8216-34

[266] R. Loddo, V. Francesconi, E. Laurini, S. Boccardo, M. Fermeglia, S. Pricl, M. Tonelli 9-Aminoacridine-based agents impair the bovine viral diarrhea virus (BVDV) replication targeting the RNA-dependent RNA Polymerase (RdRp). ChemMedChem, **2017.**

[267] http://cgmartini.nl/index.php/tutorials-general-introduction/proteins

APPENDIX A

Fluorinated and Hydrogenated Alkanethiolates coated gold nanoparticles systems

Nanoparticles	Diameter, nm[a]	Composition[b]	%F6[c]	δ CF_3, ppm	δ 7-CF_2, ppm	C_6F_6%[d]
NP-brC12/F6-a	3.7 ± 0.6	$Au_{2230}(brC12)_{305}(F6)_{22}$	6.8	-80.84	-126.10	0
NP-brC12/F6-b	3.6 ± 0.7	$Au_{1830}(brC12)_{250}(F6)_{43}$	14.7	-80.98	-126.30	0
NP-brC12/F6-c	3.4 ± 0.8	$Au_{1340}(brC12)_{202}(F6)_{47}$	19.2	-81.16	-126.50	0
NP-brC12/F6-d	2.1 ± 0.6	$Au_{270}(brC12)_{68}(F6)_{17}$	19.8	-81.23	-126.50	0
NP-brC12/F6-e	3.1 ± 0.9	$Au_{976}(brC12)_{148}(F6)_{62}$	29.4	-81.12	-126.40	0
NP-brC12/F6-f	1.6 ± 0.5	$Au_{208}(brC12)_{30}(F6)_{24}$	44.6	-81.22	-126.50	0
NP-brC12/F6-g	2.8 ± 0.6	$Au_{807}(brC12)_{76}(F6)_{92}$	54.5	-81.60	-126.90	40.0
NP-brC12/F6-h	2.7 ± 0.9	$Au_{500}(brC12)_{28}(F6)_{139}$	83.3	-81.60	-126.95	60.0
NP-brC12/F6-i	1.9 ± 0.9	$Au_{201}(brC12)_{11}(F6)_{63}$	85.1	-81.63	-127.00	46.7

*Table 15: Characterization data for nanoparticles **NP-brC12/F6**, ^{19}F chemical shifts of CF_3 and 7-CF_2 groups and percentage of C_6F_6 added. [a] Average diameters and standard deviation of a population of at least 300 particles. [b] Calculated on the basis of the TGA and TEM and ^1H NMR analyses of decomposed nanoparticles. [c] Percentage of the fluorinated ligand in the monolayer of nanoparticles **NP-brC12/F6** determined by ^1H NMR analysis of decomposed nanoparticles. [d] Percentage of C_6F_6 in the mixture $CDCl_3/C_6F_6$ added to solubilize the nanoparticles for NMR experiments.*

Nanoparticles	Diameter, nm[a]	Composition[b]	%F10[c]	δ CF_3, ppm	δ 9-CF_2, ppm	C_6F_6,%[d]
NP-C12/F10-a	3.2 ± 0.3	$Au_{1289}(C12)_{194}(F10)_{31}$	13.9	-81.05	-126.45	0
NP-C12/F10-b	3.2 ± 0.3	$Au_{1089}(C12)_{187}(F10)_{35}$	15.7	-81.19	-126.50	0
NP-C12/F10-c	3.6 ± 0.6	$Au_{1830}(C12)_{176}(F10)_{43}$	20.0	-81.05	-126.44	0
NP-C12/F10-d	3.6 ± 0.6	$Au_{1830}(C12)_{211}(F10)_{73}$	25.8	-81.35	-126.67	0
NP-C12/F10-e	3.2 ± 0.3	$Au_{1289}(C12)_{161}(F10)_{60}$	27.2	-81.53	-126.80	20.0
NP-C12/F10-f	3.2 ± 0.3	$Au_{1289}(C12)_{136}(F10)_{78}$	36.6	-81.62	-126.90	20.0
NP-C12/F10-g	3.6 ± 0.6	$Au_{1830}(C12)_{170}(F10)_{112}$	40.0	-81.62	-127.01	33.0
NP-C12/F10-h	4.0 ± 0.6	$Au_{2406}(C12)_{126}(F10)_{200}$	61.5	-81.51	-127.05	71.0
NP-C12/F10-i	3.2 ± 0.5	$Au_{1289}(C12)_{27}(F10)_{186}$	87.3	-81.62	-127.12	82.8

*Table 16: Characterization data for nanoparticles **NP-C12/F10**, ^{19}F chemical shifts of CF_3 and 9-CF_2 groups and percentage of C_6F_6 added. [a] Average diameters and standard deviation obtained by analysis of a population of at least 300 particles. [b] Calculated on the basis of the TGA and TEM and ^1H NMR analyses of decomposed nanoparticles. [c] Percentage of the fluorinated ligand in the monolayer of nanoparticles **NP-C12/F10** determined by ^1H NMR analysis of decomposed nanoparticles. [d] Percentage of C_6F_6 in the mixture $CDCl_3/C_6F_6$ added to solubilize the nanoparticles for NMR experiments.*

Nanoparticles	Diameter, nm[a]	Composition[b]	%F6[c]	δ CF_3, ppm	δ 7-CF_2, ppm	C_6F_6% [d]
NP-C8/F6-a	3.0 ± 0.6	$Au_{976}(C8)_{229}(F6)_{11}$	4.5	-80.83	-126.30	0
NP-C8/F6-b	3.3 ± 0.8	$Au_{1340}(C8)_{246}(F6)_{18}$	6.8	-80.89	-126.22	0
NP-C8/F6-c	3.8 ± 0.7	$Au_{1634}(C8)_{283}(F6)_{29}$	9.3	-81.01	-126.37	0
NP-C8/F6-d	2.7 ± 0.5	$Au_{527}(C8)_{139}(F6)_{38}$	21.3	-81.19	-126.55	0
NP-C8/F6-e	3.0 ± 0.6	$Au_{976}(C8)_{166}(F6)_{46}$	21.7	-81.22	-126.50	0
NP-C8/F6-f	2.8 ± 0.6	$Au_{780}(C8)_{114}(F6)_{67}$	37.0	-81.41	-126.73	0
NP-C8/F6-g	2.6 ± 0.5	$Au_{475}(C8)_{75}(F6)_{53}$	41.7	-81.45	-126.76	0
NP-C8/F6-h	3.1 ± 0.6	$Au_{976}(C8)_{126}(F6)_{90}$	41.7	-81.45	-126.76	0
NP-C8/F6-i	1.9 ± 0.4	$Au_{225}(C8)_{42}(F6)_{38}$	47.5	-81.40	-126.78	20.0
NP-C8/F6-j	2.4 ± 0.5	$Au_{465}(C8)_{57}(F6)_{57}$	50.0	-81.36	-126.80	40.0
NP-C8/F6-k	2.3 ± 0.5	$Au_{459}(C8)_{57}(F6)_{57}$	50.0	-81.45	-126.80	0
NP-C8/F6-l	2.4 ± 0.5	$Au_{459}(C8)_{53}(F6)_{59}$	52.2	-81.47	-126.85	40.0
NP-C8/F6-m	2.9 ± 0.5	$Au_{807}(C8)_{86}(F6)_{98}$	53.3	-81.42	-126.78	40.0
NP-C8/F6-n	2.5 ± 0.5	$Au_{465}(C8)_{42}(F8)_{76}$	63.8	-81.51	-126.88	40.0
NP-C8/F6-o	2.4 ± 0.4	$Au_{459}(C8)_{32}(F6)_{80}$	71.7	-81.58	-126.96	40.0
NP-C8/F6-p	2.2 ± 0.6	$Au_{309}(C8)_{25}(F6)_{70}$	73.7	-81.53	-126.96	60.0
NP-C8/F6-q	2.5 ± 0.4	$Au_{460}(C8)_{16}(F6)_{78}$	83.0	-81.55	-126.96	40.0

*Table 17: Characterization data for nanoparticles **NP-C8/F6**, ^{19}F chemical shifts of CF_3 and 7-CF_2 groups and percentage of C_6F_6 added. [a] Average diameters and standard deviation of a population of at least 300 particles. [b] Calculated on the basis of the TGA and TEM and ^1H NMR analyses of decomposed nanoparticles. [c] Percentage of the fluorinated ligand in the monolayer of nanoparticles **NP-C8/F6** determined by ^1H NMR analysis of decomposed nanoparticles. [d] Percentage of C_6F_6 in the mixture $CDCl_3/C_6F_6$ added to solubilize the nanoparticles for NMR experiments.*

Nanoparticles	Diameter,[a] nm	Composition[b]	%F6[c]	δ CF_3, ppm	δ 7-CF_2, ppm	C_6F_6%[d]
NP-C16/F6-a	2.9 ± 0.5	$Au_{976}(C16)_{177}(F6)_{6}$	2.6	-80.84	-126.10	0
NP-C16/F6-b	3.2 ± 0.6	$Au_{1289}(C16)_{213}(F6)_{8}$	3.6	-81.00	-126.30	0
NP-C16/F6-c	2.6 ± 0.5	$Au_{460}(C16)_{105}(F6)_{5}$	4.5	-81.12	-126.43	0
NP-C16/F6-d	3.0 ± 0.5	$Au_{976}(C16)_{178}(F6)_{11}$	5.5	-81.00	-126.33	0
NP-C16/F6-e	3.2 ± 0.6	$Au_{976}(C16)_{147}(F6)_{42}$	21.7	-81.19	-126.43	0
NP-C16/F6-f	2.9 ± 0.5	$Au_{800}(C16)_{142}(F6)_{79}$	35.7	-81.40	-126.70	0
NP-C16/F6-g	2.1 ± 0.4	$Au_{309}(C16)_{42}(F6)_{35}$	45.5	-81.58	-126.91	0
NP-C16/F6-h	2.1 ± 0.4	$Au_{309}(C16)_{40}(F6)_{44}$	52.4	-81.51	-126.83	0
NP-C16/F6-i	2.6 ± 0.4	$Au_{475}(C16)_{70}(F6)_{80}$	53.3	-81.51	-126.85	0
NP-C16/F6-j	2.5 ± 0.3	$Au_{475}(C16)_{71}(F6)_{96}$	57.3	-81.45	-126.78	0
NP-C16/F6-k	2.7 ± 0.6	$Au_{527}(C16)_{55}(F6)_{74}$	57.4	-81.60	-126.91	12.5
NP-C16/F6-l	2.0 ± 0.4	$Au_{309}(C16)_{31}(F6)_{44}$	58.6	-81.55	-126.88	12.5
NP-C16/F6-m	2.1 ± 0.5	$Au_{309}(C16)_{26}(F6)_{52}$	66.6	-81.71	-127.06	37.5
NP-C16/F6-n	2.3 ± 0.4	$Au_{314}(C16)_{23}(F6)_{63}$	73.0	-81.47	-126.86	0
NP-C16/F6-o	2.2 ± 0.4	$Au_{314}(C16)_{19}(F6)_{61}$	76.2	-81.58	-126.86	37.5
NP-C16/F6-p	2.1 ± 0.3	$Au_{309}(C16)_{19}(F6)_{62}$	76.4	-81.71	-127.01	37.5
NP-C16/F6-q	2.2 ± 0.5	$Au_{314}(C16)_{18}(F6)_{72}$	80.4	-81.67	-127.08	25.0

*Table 18: Characterization data for nanoparticles **NP-C16/F6**, ^{19}F chemical shifts of CF_3 and 7-CF_2 groups and percentage of C_6F_6 added. [a] Average diameters and standard deviation of a population of at least 300 particles. [b] Calculated on the basis of the TGA and TEM and ^1H NMR analyses of decomposed nanoparticles. [c] Percentage of the fluorinated ligand in the monolayer of nanoparticles **NP-C16/F6** determined by ^1H NMR*

analysis of decomposed nanoparticles. [d] Percentage of C_6F_6 in the mixture $CDCl_3/C_6F_6$ added to solubilize the nanoparticles for NMR experiments.

Nanoparticles	Diameter, nm[a]	Composition[b]	%F6[c]	δ CF_3, ppm	δ 7-CF_2, ppm	C_6F_6%[d]
NP-C12/F6-a	3.4 ± 0.4	$Au_{1340}(C12)_{213}(F6)_{26}$	10.6	-80.95	-126.26	0
NP-C12/F6-b	3.3 ± 0.3	$Au_{1310}(C12)_{210}(F6)_{30}$	12.5	-81.13	-126.45	0
NP-C12/F6-c	3.4 ± 0.6	$Au_{1340}(C12)_{208}(F6)_{30}$	12.6	-81.00	-126.27	0
NP-C12/F6-d	3.2 ± 0.4	$Au_{1289}(C12)_{194}(F6)_{35}$	15.4	-80.95	-126.27	0
NP-C12/F6-e	3.2 ± 0.3	$Au_{1289}(C12)_{190}(F6)_{35}$	15.6	-81.04	-126.35	0
NP-C12/F6-f	3.3 ± 0.6	$Au_{1340}(C12)_{174}(F6)_{40}$	18.8	-81.11	-126.41	0
NP-C12/F6-g	3.2 ± 0.4	$Au_{1289}(C12)_{185}(F6)_{46}$	20.0	-81.06	-126.35	0
NP-C12/F6-h	3.8 ± 0.3	$Au_{2267}(C12)_{232}(F6)_{68}$	22.7	-81.08	-126.37	0
NP-C12/F6-i	3.6 ± 0.6	$Au_{1830}(C12)_{197}(F6)_{73}$	27.0	-81.26	-126.52	0
NP-C12/F6-j	3.6 ± 0.6	$Au_{1830}(C12)_{209}(F6)_{85}$	28.6	-81.22	-126.54	0
NP-C12/F6-k	3.6 ± 0.6	$Au_{1830}(C12)_{206}(F6)_{86}$	29.4	-81.15	-126.47	0
NP-C12/F6-l	3.6 ± 0.6	$Au_{1830}(C12)_{180}(F6)_{100}$	35.7	-81.66	-126.70	26.6
NP-C12/F6-m	2.5 ± 0.7	$Au_{488}(C12)_{81}(F6)_{48}$	37.0	-81.33	-126.60	0
NP-C12/F6-n	3.6 ± 0.6	$Au_{1830}(C12)_{184}(F6)_{123}$	40.0	-81.76	-126.72	26.6
NP-C12/F6-o	3.2 ± 0.8	$Au_{1289}(C12)_{123}(F6)_{112}$	47.8	-81.94	-127.07	26.6
NP-C12/F6-p	3.0 ± 0.8	$Au_{976}(C12)_{74}(F6)_{108}$	60.0	-82.07	-127.14	60.0
NP-C12/F6-q	3.1 ± 0.4	$Au_{1200}(C12)_{73}(F6)_{160}$	72.0	-82.10	-127.13	62.5

Table 19: Table S5. Characterization data for nanoparticles NP-C12/F6, 19F chemical shifts of CF3 and 7-CF2 groups and percentage of C6F6 added. a Average diameters and standard deviation obtained by analysis of a population of at least 300 particles. b Calculated on the basis of the TGA and TEM and 1H NMR analyses of decomposed nanoparticles. c Percentage of the fluorinated ligand in the monolayer of nanoparticles NP-C12/F6 determined by 1H NMR analysis of decomposed nanoparticles. d Percentage of C6F6 in the mixture CDCl3/C6F6 added to solubilize the nanoparticles for NMR experiments.

APPENDIX B

Atomic Force Microscopy

An Atom Force Microscopy (AFM) experimental investigation was conducted at NanoInnovation Laboratory (Head Dr. Loredana Casalis) established in Elettra Sincrotrone (Trieste) to evaluate how SAM coated NPs interact with synthetic membranes. Initially, some preliminary experiments were carried out employing different functionalized gold nanoparticles (AuNPs), already available in the laboratory, in order to become familiar with the machine, procedures and protocols commonly used.

The lipid layers deposition techniques we tried were (Figure 71):

- drop casting deposition protocol
- liposome deposition protocol

According to the drop casting technique, lipid powder was melted in a solvent (usually methanol/chloroform) and successively a drop was placed on the substrate (glass or mica). The system was heated in order to evaporate the solvent and left on the substrate only the lipid layers. Unfortunately using this technique there were many limits to cope with; uniformity and thickness of the layer above all were difficult to control.

The liposome deposition protocol allowed the creation of lipid vesicles in a buffer (like PBS, methanol/chloroform) through extrusion. A drop of the solution was placed on the glass substrate and the system has been heated in oven at 40 °C for 20-30 minutes. In this way vesicles broke and formed membranes full of defects on the substrate. However, this protocol leads to a greater probability to obtain a single layer due to the presence of no self-assembling between lipid molecules (Figure 72).

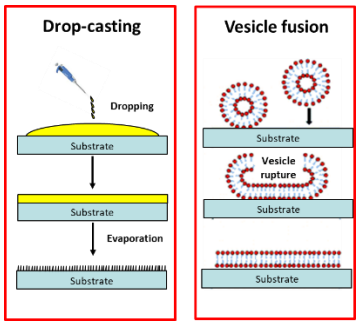

Figure 71: comparison of the drop casting deposition protocol (right) and liposome deposition protocol (left).

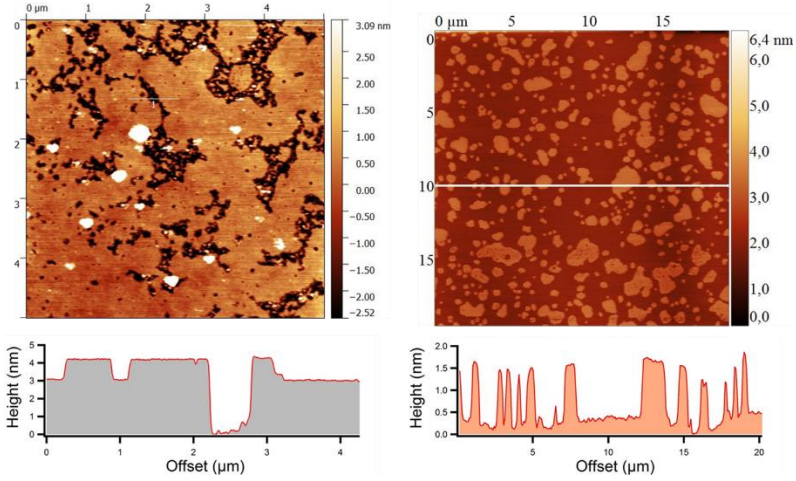

Figure 72: comparison of a 1,2-dioleoyl-sn-glycero-3-phosphocholine (DOPC) membrane, obtained with the drop casting deposition protocol (left panel) and of a DOPC/sphingomyelin (SM)/cholesterol (Chol) membrane, obtained with the liposome deposition protocol (right panel). From the height profile is possible to appreciate the formation of a double bilayer (left) and of a single layer (right). AFM imaging in non-contact mode in milliQ water. Substrate used, glass.

Later, further experiments were carried out to evaluate the interaction between AuNPs and synthetic lipid membranes. NP concentration, lipid type and deposition techniques of the Supported Lipid Bilayer (SLB) (drop casting and vesicles) were varied, without changing the glass substrate. These experiments were carried out in liquid (usually PBS and H_2O) optimizing the controlled formation of the layers in order to enhance AuNPs insertion. From literature is known that the presence of more than 2 lipidic bi-layers invalidates NPs insertion; in this situation NP can penetrate through layers avoiding the superficial imaging of the AFM. It is also known that a defect-free membrane does not permit insertion which is enhanced at defect's edges in presence of large defects. The deposition protocol optimization is necessary in order to have more or less 1-2 bi-layer membrane defects. After NPs addition, no changes in the morphology of the membrane was observed. This can be related to the

presence of more than one bi-layer, through which AuNPs may have been penetrated, avoiding the AFM superficial imaging. In order to obtain 1-2 layer on the substrate we focused our attention on the optimization of the SLBs deposition protocol (in collaboration with Fabio Perissinotto, PhD student in Nanotechnology working on these techniques and topics in his research project) both with liposomes and drop casting.

Further experiments were carried out on DOPC membrane with a new batch of NPs (NP-C12/F10, see Chapter 3) provided by Prof. Lucia Pasquato (Department of Chemical and Pharmaceutical Sciences, University of Trieste).

We performed the experiments using the drop casting deposition protocol, following the procedure employed by the group of Stellacci in (86). In all the experiments no variations in terms of height were observed after the addition of NPs except in one case (Figure 73), in which we noticed an effect similar to that reported in literature (86), The interaction between NPs and the membrane seemed to be enhanced along the edges of lipid islands, as observed by Stellacci et all in (86). Unfortunately, it was difficult to be reproduced.

.

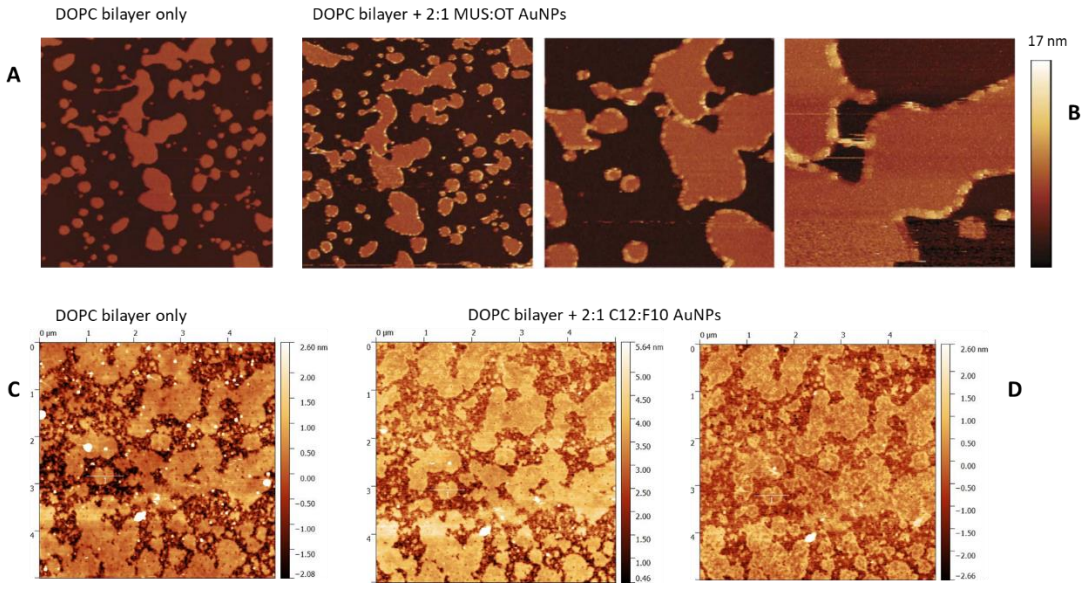

Figure 73: Comparison of referenced (86) results (A and B) with our results obtained following the same AFM procedure of A and B (C and D). The lipid components used has been the same in both cases which differ in the mixture employed in coating NPs. Ligand ratio was the same. The injected NPs were 2:1 MUS:OT AuNPs (B) and 2:1 C12:F10 AuNPs (D).

APPENDIX C

In-vitro experimental assays of C8T/F8P-AuNPs

This activity was performed by prof. Sabrina Pacor, prof. Alessandro Tossi and Dr. Filomena Guida (Department of Life Science, University of Trieste) and some relevant results useful to complement the computational analysis are reported here.

The confocal analysis (Figure 74) clearly displayed that both M1- and M2-C8T/F8P/BODIPY crossed the plasma membrane and reach the cytoplasm, while they did not appear to localize in the nuclear compartment. Even taking the difference of BODIPY loading and quenching into account, using a M1-C8T/F8P/BODIPY at a concentration ten times higher than M2-C8T/F8P/BODIPY, the fluorescence signal of cells treated with Janus NPs appeared less intense. This was confirmed also by flow cytometric analysis (Figure 74D). The effects of NP concentration and exposure time on the interaction of M1- and M2-C8T/F8P with MEC-1 cells are shown in Figure 74 indicating a remarkable different behavior between the two mixed systems, in line with that observed in SPR experiments and the computational analysis.

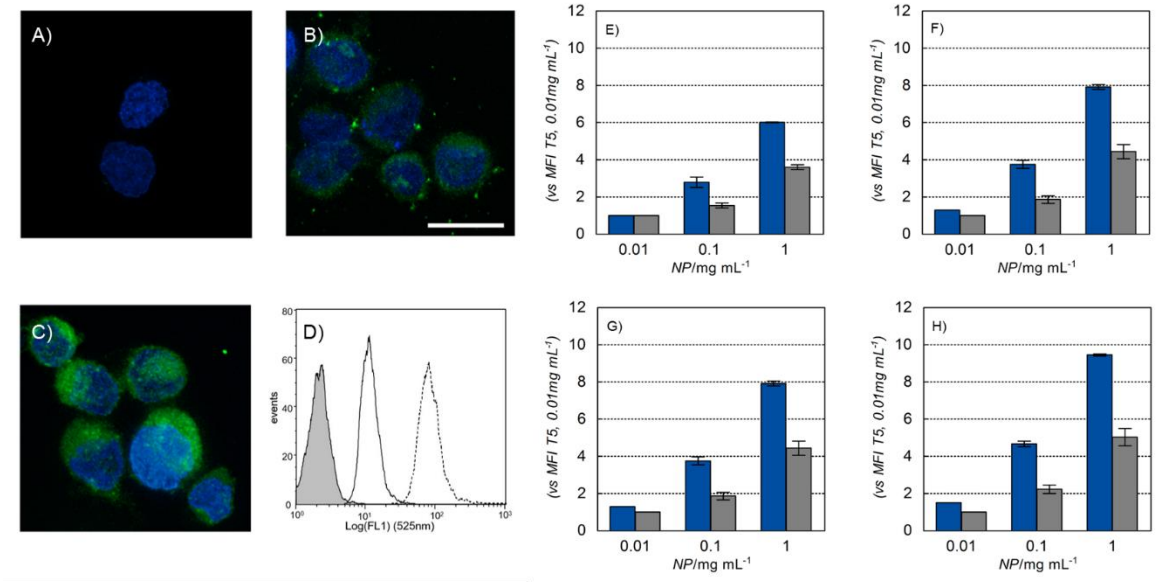

Figure 74: ***Confocal microscopy and flow cytometry of cells treated with mixed-ligand, BODIPY-tagged SAM-AuNPs.*** *Confocal images of (A) control MEC-1 cells, (B) cells treated with 1 mg mL^{-1} M1-C8T/F8P/BODIPY AuNPs and (C) cells treated with 0.1 mg mL^{-1} M2-C8T/F8P/BODIPY AuNPs, for 60 min prior to counterstaining nuclei with Hoechst dye. (D) Flow cytometric monoparametric overlay plot of green fluorescence emitted from untreated (grey peak) and cells treated with 1 mg mL^{-1} M1-C8T/F8P/BODIPY AuNPs (—) and 0.1 mg mL^{-1} M2-C8T/F8P/BODIPY AuNPs (-----).*

APPENDIX D

Experimental data Crystal Violet (UV e NMR)

The interaction of AuNP and CV have been studied in solution via UV and ^{1}H NMR. Unfortunately, misleading results have been obtained based on UV and NMR techniques due to bigger complexity of the system.

D.1) UV

The freedom of CV molecules to form multiple interactions with more than one AuNP caused the formation of small insoluble aggregates, which didn't allow to study the system employing UV and NMR techniques.

Figure 75 showed the UV titration in D_2O of Crystal Violet (CV) with 4nm gold nanoparticles covered 100% with MUS ligand. The Blue shift of the CV max absorbance (587nm to 530nm) has been observed. This phenomenon confirmed multiple interactions of CV molecules with present gold nanoparticles, leading to the formation of small particle and CV aggregates (Absorption of GNP shifted from initial 515nm to 530nm).

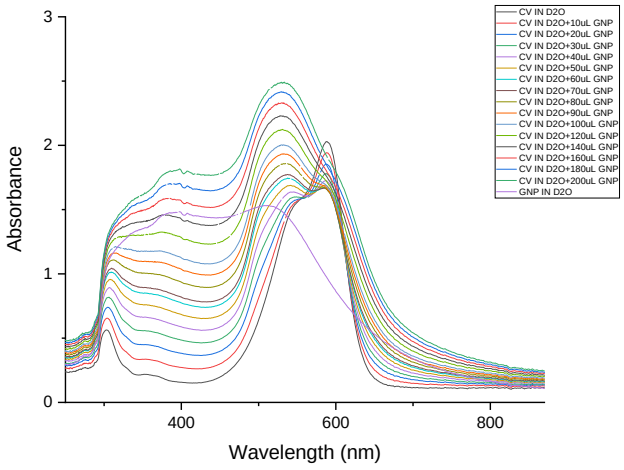

Figure 75: UV spectra of Crystal Violet (CV) with 4nm gold nanoparticles covered 100% with MUS ligand

D.2) NMR

Figure 76 showed the ^{1}H NMR (400MHz, D_2O) titration of Crystal Violet (CV) with 4nm gold nanoparticles covered 100% with MUS ligand. Marginal downfield shift of aromatic CV signals (d 6,9011ppm -> 6,9210ppm and d 7,3470ppm -> 7,3711ppm) and final signal disappearance have been observed. The disappearance of N-CH_3 signal (3,1432ppm) has been observed as well. This behavior confirms the interaction of CV and GNP forming small, insoluble, aggregates. The GNP broad pick can be noticed between 1,400ppm and 1,5500ppm. The D_2O signal has been omitted for clarification.

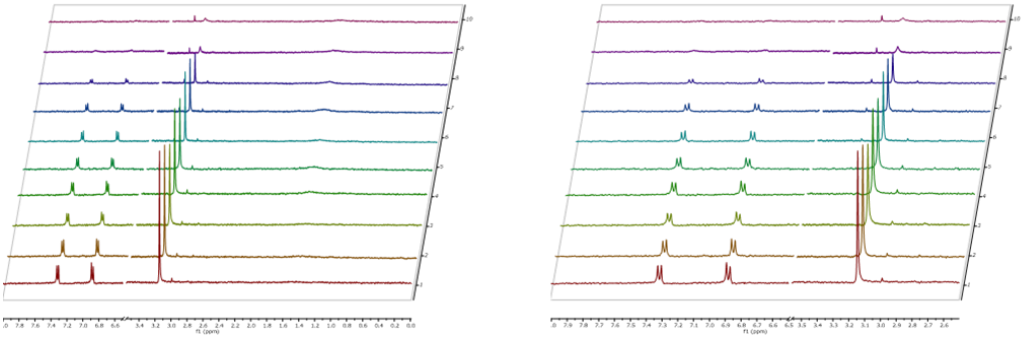

Figure 76: ^{1}H NMR (400MHz, D_2O) titration of Crystal Violet (CV) with 4nm gold nanoparticles covered 100% with MUS ligand

Acknowledgements

This work is generously supported by the Italian Ministry of University Research (MIUR) through the Scientific Independence of Young Researchers (SIR) project “Structure and FunctiOn at the Nanoparticle bioInterfAce” (grant RBSI14PBC6 to Paola Posocco).